Property Measurements of the Higgs Boson and Search for High Mass Resonances in Four-Lepton Final State with the ATLAS Detector at the LHC

by

Nan Lu

A dissertation submitted in partial fulfillment
of the requirements for the degree of
Doctor of Philosophy
(Physics)
in The University of Michigan
2017

Doctoral Committee:

Professor Bing Zhou, Chair
Professor Finn Larsen
Professor Homer A. Neal
Professor Gregory Tarle
Professor Ji Zhu

Nan Lu

nanlu@umich.edu

ORCID iD: 0000-0002-2631-6770

ACKNOWLEDGEMENTS

First and foremost, I would like to express my deepest gratitude to my advisor Bing Zhou for her guidance and support though my Ph.D. study. Bing's vision, leadership, dedication and immense knowledge have deeply influenced me. I am extremely fortunate to have Bing as my advisor.

Besides my advisor, I would like to thank other members of my thesis committee: Finn Larsen, Homer A. Neal, Gregory Tarle and Ji Zhu, for reviewing my thesis and providing very helpful and enlightening comments.

I am very grateful for the opportunities to take the physics courses offered by Myron Campbell, Henriette Elvang, Emanuel Gull, Gordon L. Kane, David Lubensky, Roberto D. Merlin, Leonard M. Sander, and Bing Zhou, which have helped me appreciate the beauty of physics and have laid the foundations for my research work.

I would like to express my sincere gratitude to the Michigan ATLAS group. I thank Haijun Yang for teaching me the concepts and methods in physics analysis during my early time in the group. My thanks to Lailin Xu for helping me learn physics analysis software and the nice collaboration on several research projects. I appreciate his patience to help and discuss with me at all times. My thanks also go to Cong Geng for developing the very nice analysis framework for the event selection in Run 2 and the pleasant collaboration on the HZZ physics analyses. I also thank Yusheng Wu for the illuminating discussions in many aspects of the physics analyses that I have worked on and his advice on career developments. I would like to thank Dante Amidei, Homer A. Neal, Jianming Qian, Tom Schwarz, Junjie Zhu for the insightful discussions on physics analyses and encouragements to me. I sincerely thank Tiesheng Dai for training and supervising me on the hardware work projects including the New Small Wheel simulation study for the L1 trigger and debugging the 12.5 ns T_0 time jump issue in the MDT readout electronics, which are crucial learning and research experiences to me. I also thank John Chapman and Bob Ball for their help in debugging the 12.5 ns T_0 time jump issue. I would like to thank Shawn McKee, Bob Ball, and Benjeman Meekhof for their strong support of computing resources, which is an indispensable asset to my research projects. I also thank other former

and present colleagues in the Michigan group: Tom Cheng, Edward Diehl, Haolu Feng, Philipp Fleischmann, Liang Guan, Wen Guo, Yicheng Guo, Bing Li, Xuefei Li, Hao Liu, Jianbei Liu, Lulu Liu, Yanlin Liu, Daniel Marley, Allison McCarn, Karishma Sekhon, Ismet Siral, Rongkun Wang, Aaron White, Zhaoxu Xi, Jiaming Yu, Dongliang Zhang, and many others for their friendship and help.

I am very fortunate to have the opportunities to work with many outstanding physicists as a member of the ATLAS Collaboration. I would like to express my sincere gratitude to Hong Ma and Eleni Mountricha from Brookhaven National Laboratory for the successful and pleasant collaboration on the physics analyses in the HZZ sub-working group. I am deeply grateful to Hong Ma for his guidance and encouragement to me. My special thanks to Eleni for all the support, encouragement and guidance which have made a difference in my research. I am very grateful for the opportunity to closely work with you over the past two years, and it has been a wonderful experience for me.

I sincerely thank Fabio Cerutti for his help and support to me in the combined Higgs boson spin and parity study in diboson channels and Higgs boson coupling measurements in the four-lepton final state. I have learned a lot from his sharp insight in physics.

I would also like to express my sincere gratitude to Stefano Rosati. Under his help and support, I started to learn how to perform combined measurements of the Higgs boson properties. I am also very grateful for his guidance and enlightening discussions with me on the Higgs boson property measurements in the four-lepton final state for Run 2.

I am very thankful to Bruno Mansoulie for the support in several physics analyses that I have worked on. His insightful comments and discussions have been very helpful to me.

I appreciate very much the enriching experience working with colleagues in the HZZ sub-working group on the high mass search and Higgs coupling measurements in the four-lepton final state. I am very grateful for the guidance and support from the HZZ conveners Rosy Nicolaidou, Robert Harrington, Roberto Di Nardo, Sarah Heim, Eleni Mountricha and Arthur Schaffer. I also thank Haider Abidi, Gaetano Barone, Valerio Bortolotto, Graham Cree, Denys Denysiuk, Tulay Donszelmann, Katharina Ecker, Andrea Gabrielli, Cong Geng, Wen Guo, Xiangyang Ju, Maria Hoffmann, Giada Mancini, Jochen Meyer, Ioannis Nomidis, Hideki Okawa, Lars Pedersen, Antonio Salvucci, Monica Trovatelli, David Valentino, Rongkun Wang, Yusheng Wu, Lailin Xu, and many other colleagues. It has been a great pleasure working with you.

I would like to thank colleagues working on the combined measurement of Higgs boson production and decay rates. I appreciate very much the coordination and support from the Higgs working group conveners Fabio Cerutti, Michael Duehrssen and Bruno Mansoulie, the Hcomb sub-working group conveners Nicolas Berger, Eric Feng, and Elisabetta Pianori. I also thank Lydia Brenner, Carsten Burgard, Xiaohu Sun and Jared Vasquez for the great teamwork. I have learned a lot from all of you.

I would like to thank colleagues working on the Higgs boson spin and parity study in the four-lepton channel and in combining the diboson channels. I appreciate very much the coordination and support from the Higgs working group conveners Marumi Kado and Pierre Savard, the Hcomb sub-working group conveners Bruno Mansoulie and Kirill Prokofiev. I thank the Editorial Boards chaired by Karl Jakobs and Aleandro Nisati for the very helpful discussions. I am grateful for the guidance and support from Fabio Cerutti, Kirill Prokofiev, and Stefano Rosati. I also thank Valerio Bortolotto, Eric Feng, Katharina Ecker, Tulay Donszelmann, Andrea Gabrielli, Haonan Lu, Lars Pedersen, Antonio Salvucci, Lailin Xu for their help.

My sincere thanks also go to Bing Li, Xuefei Li, Jianbei Liu and Lailin Xu for their help and guidance to me in the $Z \to 4\ell$ analysis. For the inclusive four-lepton analysis, I would like to thank Bing Li and Yusheng Wu for the support and discussions. In the $vvqq$ diboson resonance search, I thank Yicheng Guo, Francesco Lo Sterzo, Chao Wang and Lailin Xu for their help.

I would like to thank Elise Bodei, Joseph Sheldon, Paul Thurmond and Christina Zigulis for the outstanding administrative support. My special thanks to Christina for her kind help as the graduate program coordinator. Especially during the years when I was based at CERN, her remote help meant a lot to me.

Finally, I would like to express my sincere gratitude to my parents, my grandparents, and my husband Hongtao Yang. I am deeply grateful for your unconditional love and supporting my pursuit of experimental particle physics. This thesis is dedicated to you.

TABLE OF CONTENTS

LIST OF FIGURES

Figure

LIST OF TABLES

Table

ABSTRACT

The discovery of a Higgs boson by the ATLAS and CMS experiments at the Large Hadron Collider (LHC) at CERN in 2012 marked the beginning of a new era of experimental particle physics research through studies of the properties of this new particle. It is extremely important to determine the new particle's the quantum numbers - spin and parity, and to measure its couplings to fermions and vector bosons to confirm if the newly discovered particle is the Higgs boson predicted almost 50 years ago by the Standard Model (SM) of particle physics. In the SM, the Higgs boson is a scalar particle with positive parity ($J^P = 0^+$). It is responsible for generating masses for all the massive particles in our universe through the electroweak symmetry breaking mechanism.

This dissertation presents the measurements of the quantum numbers and couplings of the newly discovered boson using data collected in proton-proton collisions at the center-of-mass energies ($\sqrt{s}$) of 7, 8 and 13 TeV at the LHC by the ATLAS experiment during 2011-2012 and 2015-2016. The measurements are conducted with four-lepton (4ℓ) final state, where leptons are electrons and muons, which are produced from the cascade decay chain of the Higgs boson to the Z boson pair (ZZ^*) in the reaction of $pp \to H \to ZZ^* \to 4\ell$.

In the determination of the new particle's spin and parity, data is compared with different theoretical hypotheses using multivariate analysis approach. The SM Higgs boson prediction is tested against non-SM spin and parity hypotheses, including spin-0 and spin-2 models with universal and non-universal couplings to fermions and vector bosons. Data is in favor of the SM Higgs boson predicted quantum numbers, and all tested alternative models are excluded at more than 99.9% confidence level (CL) combining diboson decay channels using data collected at $\sqrt{s} = 7$ and 8 TeV with a total integrated luminosity of 25 fb^{-1}.

The Higgs boson coupling measurement is made by selecting inclusive four-lepton events from Higgs boson decays. These events are further divided into different categories based on the associated jet production and lepton kinematic distributions of the events. Each category is designed to have good sensitivity to certain Higgs production mechanism. The Boosted-Decision-Tree multivariate analysis technique has been developed and used in event categorization. The likelihood fit technique is used

to compare kinematic distributions of the selected four-lepton events with different coupling scenarios to determine the coupling strength and compared to the SM predictions. Using data collected at $\sqrt{s} = 13$ TeV with a total integrated luminosity of 36.1 fb^{-1}, The Higgs to vector boson and fermion couplings are measured with precision of 15% and 40%, respectively.

Many theoretical models beyond the SM (BSM), such as the two-Higgs-doublet model and the electroweak singlet model, predicted the existence of additional Higgs bosons at higher mass range. A search for BSM high mass Higgs boson has been performed using the data collected at $\sqrt{s} = 13$ TeV with a total integrated luminosity of 3.2 fb^{-1}, and no evidence of an additional Higgs boson has been observed in the four-lepton mass spectrum. Upper limits at the 95% CL are set on the production cross section times branching ratio of a heavy scalar boson decaying to four leptons. This search results will also be presented in this dissertation.

CHAPTER I

Introduction

What are the fundamental building blocks of matter and their interactions are basic questions to answer in the endeavor to understand the universe we live in. The Standard Model (SM) of particle physics [1, 2, 3], developed in the early 1960s based on gauge invariance principle, is the theory aiming to answer these questions. It has been very successful in explaining experimental results and precisely predicted a wide variety of phenomena. Thus, the SM is established as a well-tested theory in particle physics. In the SM, quarks and leptons are the fundamental building blocks of matter, and they interact through the exchange of force carriers: the photon for electromagnetic interactions, the W and Z bosons for weak interactions, and the gluons for strong interactions. The electromagnetic and weak interactions are unified in the SM, referred as the electroweak theory. Although the predictions of the SM have been extensively confirmed, the origin of all the particle masses remains a mystery since the mass terms in the theory framework will break the gauge invariance.

In 1964, Robert Brout, Francois Englert and Peter Higgs independently proposed a theoretical mechanism in the SM to explain how the W and Z bosons acquire mass by applying spontaneous symmetry breaking mechanism to the electroweak theory through a complex scalar doublet field [4, 5, 6, 7]. The fermions can also acquire mass through the Yukawa interaction with this scalar field. The corresponding particle of this field is a neutral scalar particle, called Higgs boson. The mass of the SM Higgs boson m_H is a free parameter in the theory, while all properties of the Higgs boson are precisely predicted by the theory once m_H is known. There are just a few theory constraints on the m_H under different assumptions. General theoretical considerations suggest that the m_H should be smaller than 1 TeV [8, 9, 10, 11], while precision electroweak measurements further constrained $m_H < 152$ GeV at 95% confidence level (CL) [12].

Over the past two decades, direct searches for the Higgs boson have been carried out at collider experiments. Prior to the LHC, experiments at the Large Electron-Positron (LEP) collider excluded the Higgs boson with m_H range below 114.4 GeV at 95% CL [13]; and experiments at the Tevatron proton-antiproton collider excluded the Higgs boson in a mass range of $162 \sim 166$ GeV at 95% CL [14], but detected an excess of events in the mass range of $120 \sim 135$ GeV [15, 16, 17]. Search for the SM Higgs boson is one of the primary physics motivations for the LHC experiments [18]. In 2012, a new boson with a mass of about 125 GeV was discovered by both the ATLAS and CMS experiments at the LHC [19, 20]. The discovery was made in the Higgs boson search physics program and based primarily on the $H \to \gamma\gamma$ channel, and the $H \to ZZ^* \to 4\ell$ (ℓ denotes an electron or a muon) channel, where one or two of the Z bosons are produced off-shell.

This discovery opened a new era of studying particle physics to advance our understanding of electroweak symmetry breaking through the measurements of the properties of this new particle. The measurements of the Higgs boson properties have been carried out in LHC Run 1 and in the on-going LHC Run 2 with increasing of precision and in many aspects such as the Higgs boson mass, spin, parity, production cross section, couplings, and Higgs decay width. The measured results are all found being consistent with those predicted from the SM Higgs boson. In the meanwhile, there are also extensive searches carried out in various final states looking for additional new scalar particles, which is predicted by several Beyond Standard Model (BSM) theories, such as the two-Higgs doublet model (2HDM) [37] and the electroweak singlet model (EWS) [119]. This dissertation will focus on the determination of the Higgs boson spin and parity and the measurement of the Higgs couplings using the $H \to ZZ^* \to 4\ell$ decay channel. The final results will be presented in combining with several other Higgs decay channels. Search for new scalar particles in high mass scale with the four-lepton final state will be presented in this thesis as well.

The dissertation is organized as follows. Chapter II gives a brief summary of the Standard Model of particle physics and the LHC phenomenology in particular focused on the Higgs boson. An overview of the the LHC and the ATLAS detector will be briefly described in Chapter III. General information on ATLAS event reconstruction will be covered in Chapter IV. The event selection of the $H \to ZZ^* \to 4\ell$ decay channel is presented in Chapter V. Then, the statistical modeling and procedures used in the analysis are presented in Chapter VI. The following two Chapters VII and VIII give descriptions on the determination of the Higgs boson spin and parity, and the measurement of the Higgs couplings, with the $H \to ZZ^* \to 4\ell$ channel and in

combining several Higgs decay channels. Chapter IX reports the results of the search for additional high mass Higgs bosons. Finally, the dissertation ends with a summary and outlook of the Higgs boson property measurements with the ATLAS detector as the last Chapter X.

CHAPTER II

Theory

2.1 The Standard Model of Particle Physics

The SM of particle physics is a theory describing the elementary particles and their interactions, which has been very successful in explaining and predicting a wide variety of experimental results. The elementary particles and their quantum numbers of the SM is shown in Figure 2.1 [21].

The quarks and leptons are the basic building blocks of matter. They all have spin 1/2 and are referred to as fermions. There are six kinds of quarks: up, down, strange, charm, bottom and top, and as shown in Figure 2.1, they form in three generations of doubles. Up, charm and top quarks have electric charge of 2/3 e, and others have electric charge of -1/3 e, where e is the magnitude of the electron's electric charge. Each quark flavor comes in three colors, and another quantum number that all quarks carry is baryon number B. The flavor of leptons also comes in three generations of doubles. The electron (e), muon (μ), tau (τ) all have electric charge of -e, while the corresponding neutrino does not carry any electric charge. A lepton number (L) can be assigned to each generation, which is experimentally found to be conservative. All the listed elementary particles have the corresponding anti-particles, which have the same mass and spin but opposite other quantum numbers.

In addition to quarks and leptons, there are force carrier particles in the SM, which are vector bosons with the spin quantum number equals to one (spin-1) as described below:

- photon (γ, mass-less, electromagnetic force carrier),
- $W^{\pm}$ and Z boson (massive, weak force carriers),
- Eight gluons (g, mass-less, strong force carriers).

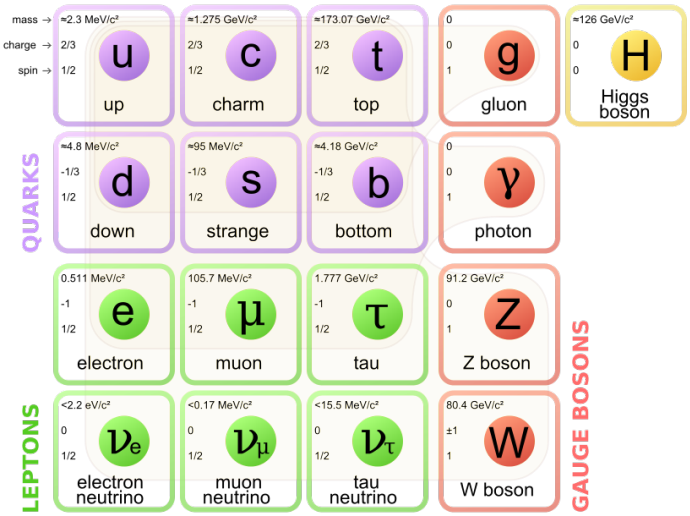

Figure 2.1: Elementary particles in the Standard Model of particle physics.

There are four types of fundamental forces observed in nature so far: gravity, electromagnetism, weak and strong interactions. The gravity is not included in the SM.

To describe the elementary particles and their interactions, the SM is formulated with three internal symmetries represented by $U(1) \times SU(2) \times SU(3)$. Under these symmetry transformations, the physics law (represented by Lagrangian of the theory) is invariant, which is called gauge invariant. $U(1) \times SU(2)$ is the symmetry related to the unified electroweak interactions for all the quarks and leptons, and $SU(3)$ is the symmetry associated with the particle interactions mediated by gluons. Under this theoretical framework based on gauge invariant all the particles must be massless, which is in contradiction with observations. To solve this theoretical problem the Higgs mechanism which predicts the existence of a neutral scalar, the Higgs boson, is introduced to explain the generation of mass through the electroweak symmetry breaking. On July 4, 2012, a new particle was discovered by the ATLAS [22] and CMS [23] experiments at CERN in the search for the Higgs boson program. In the years that followed, the ATLAS and CMS experiments have been measuring the properties of this new particle, and so far the results from the measurements are all consistent with the predicted Higgs boson in the SM [24, 25].

It is commonly believed that the SM is incomplete. For example the neutrinos are massless particles in the SM. However, the experimental discovery of neutrino oscillations by the Super-Kamiokande Observatory [26] and the Sudbury Neutrino Observatory [27] has demonstrated that neutrinos have non-zero masses, although, tiny masses. More importantly, the SM cannot explain what is dark matter in our

universe observed in astrophysics experiments. There are many deeper theoretical questions that SM cannot answer. Therefore search for new physics beyond SM is another high priority in experiments at the LHC. The newly discovered Higgs boson is a bridge to allow us to explore the new territory in particle physics research.

2.1.1 The Lagrangian of the Standard Model

The theoretical framework is built with Lagrangian which includes particle motion dynamics and conservation laws observed in nature. The conservation laws are represented by invariance of the Lagrangian under symmetry transformations. The Lagrangian of the SM, which describes the elementary particles and their interaction, can be written as

$$L_{SM} = L_{gauge} + L_{fermion} + L_{Higgs} + L_{Yukawa}, \tag{2.1}$$

where L_{gauge} term describes the gauge field tensor of the force carrier vector-bosons (Gluons, W, Z and photon) and kinematics, which is written as

$$L_{gauge} = -\frac{1}{4}G_{a\mu\nu}G_a^{\mu\nu} - \frac{1}{4}W_{a\mu\nu}W_a^{\mu\nu} - \frac{1}{4}B_{\mu\nu}B^{\mu\nu}, \tag{2.2}$$

where the non-Abelian vector potential can be written W_a^μ (a = 1,2,3 for SU(2), and 1,2,...8 for SU(3)), then the field tensor is defined as

$$W_a^{\mu\nu} = \partial^\mu W_a^\nu - \partial^\nu W_a^\mu + g f_{abc} W_b^\mu W_c^\nu \ (f_{abc} \textit{ are structure constants}); \tag{2.3}$$

the fermion term $L_{fermion}$ describes the fermion (f) kinematics and interactions with gauge bosons and is written as:

$$L_{fermion} = \sum_{f=L_L,L_R,Q_L,u_R,d_R} \bar{f} i\gamma^\mu D_\mu f, \tag{2.4}$$

where γ^μ is the Dirac matrices and D_μ is covariant derivative operator, which will be discussed later in this section; the Lagrangian of the Higgs section is given by

$$L_{Higgs} = (D_\mu\phi)^\dagger(D_\mu\phi) - V(\phi), \tag{2.5}$$

which describes the Higgs field kinematic and potential energies; and the interaction term of matter particles with the Higgs field is given by

$$L^{Q}_{Yukawa} = g_d \overline{Q_L} \phi d_R + g_u \overline{Q_L} \phi_c u_R + Herm.\ conjugate \tag{2.6}$$

which are associated with the Higgs mechanism, will be discussed in Section 2.1.2.

In the SM, the ferminons form left-handed weak-isospin doublet and right-handed weak-isospin singlet. For simplicity, we describe the theory for the first generation of leptons, which is easy to generalize to the second and third generations. The first generation of leptons can be writtin as

$$L_e = \begin{pmatrix} \nu_e \\ e_L \end{pmatrix} \tag{2.7}$$

$$R_e = (e_R) \tag{2.8}$$

The left and right handed states are defined by

$$e_L = \frac{1-\gamma^5}{2} e \tag{2.9}$$

$$\nu_L = \frac{1-\gamma^5}{2} \nu \tag{2.10}$$

$$e_R = \frac{1+\gamma^5}{2} e \tag{2.11}$$

where γ^5 is a 4×4 matrix $\begin{pmatrix} 0 & I_{2\times2} \\ I_{2\times2} & 0 \end{pmatrix}$ and $I_{2\times2}$ represents the two-dimensional unit matrix. Similarly, the first generation of quarks are written as:

$$Q_L = \begin{pmatrix} u_L \\ d_L \end{pmatrix}, u_R, d_R. \tag{2.12}$$

In order to maintain the theory invariant under gauge transformations in internal space of $U(1) \times SU(2) \times SU(3)$, the covariant derivative operator is introduced as:

$$D_\mu = \partial^\mu - i g_1 \frac{Y}{2} B_\mu - i g_2 \frac{\tau^i}{2} W^i_\mu - i g_3 \frac{\lambda^a}{2} G^a_\mu \tag{2.13}$$

where Y, τ^i, and λ^a are the generators for the U(1), SU(2) and SU(3) gauge symmetry groups, B_μ, W^i_μ and G^a_μ are gauge boson fields, and g_1, g_2 and g_3 are coupling constants between fermion and gauge fields. Then, the Lagrangian for the fermions can be written as in Equation 2.4. We further define the gauge fields $W^\pm$ and W^0 as:

$$\begin{aligned} W^+ &= (-W^1 + iW^2)/\sqrt{2} \\ W^- &= (-W^1 - iW^2)/\sqrt{2} \\ W^0 &= W^3 \end{aligned} \tag{2.14}$$

and define the neutral gauge fields A_μ and Z_μ as:

$$\begin{aligned} A_\mu &= \frac{g_2 B_\mu + g_1 W^0_\mu}{\sqrt{g_1^2 + g_2^2}} \\ Z_\mu &= \frac{g_1 B_\mu + g_2 W^0_\mu}{\sqrt{g_1^2 + g_2^2}} \end{aligned} \tag{2.15}$$

and group the coupling constants as

$$\begin{aligned} e &= \frac{g_1 g_2}{\sqrt{g_1^2 + g_2^2}} \\ sin\theta_\omega &= \frac{g_1}{g_1^2 + g_2^2} \\ cos\theta_\omega &= \frac{g_2}{g_1^2 + g_2^2}, \end{aligned} \tag{2.16}$$

the Lagrangian to describe the interaction of the first generation fermion with the force-carrier particles photons (A_μ), $W^\pm$, Z^0, and gluons (G_μ) is written as

$$\begin{aligned} L_{fermion} = & \sum_{f=\nu_e,e,u,d} eQ_f(\bar{f}\gamma^\mu f)A_\mu \\ & + \frac{g_1}{cos\theta_\omega} \sum_{f=\nu_e,e,u,d} [\bar{f}_L\gamma^\mu f_L(T^3_f - Q_f sin^2\theta_\omega) + \bar{f}_R\gamma^\mu f_R(-Q_f sin^2\theta_\omega)]Z_\mu \\ & + \frac{g_2}{\sqrt{2}}[(\bar{u}_L\gamma^\mu d_L + \bar{\nu}_{eL}\gamma^\mu e_L)W^+_\mu + Herm.\ conjugate] \\ & \frac{g_3}{2} \sum_{q=u,d} \bar{q}_\alpha \gamma^\mu \lambda^a_{\alpha\beta} q_\beta G^a_\mu \end{aligned} \tag{2.17}$$

where λ is a 3×3 matrix in the SU(3) color space. This Lagragian can apply to the second or third generation by replacing $(\nu_e, e, u, d) \rightarrow (\nu_\mu, \mu, c, s)$ or $(\nu_e, e, u, d) \rightarrow (\nu_\tau, \tau, t, b)$.

The gauge transformations under the local $U(1)$ symmetry are

$$L_e \to e^{-i\alpha(x)} L_e, \qquad R_e \to e^{-2i\alpha(x)} R_e, \qquad B_\mu \to B_\mu + \frac{2}{g_1}\partial_\mu \alpha(x),$$

and under the local SU(2) transforms are

$$L_e \to e^{-i\vec{\alpha}(x)\cdot\vec{\tau}/2} L_e, \qquad W_\mu^a \to W_\mu^a + \frac{1}{g_2}\partial_\mu \alpha^a(x) + \epsilon^{abc}\alpha^b(x) W_\mu^c,$$

where $\vec{\alpha}$ specifies the rotation angles and $\vec{\tau}$ are the Pauli matrices, the generators of the SU(2) symmetry group. Lagrangian is invariant under underlying symmetry transformations. However, adding the mass term for fermions or gauge bosons would break the SU(2) invariance of the Lagrangian. Thus, the Higgs mechanism is introduced to explain mass generation through the electroweak symmetry breaking mechanism.

2.1.2 The Higgs Mechanism

In the SM, a scalar field (called Higgs field) is introduced to break the electroweak symmetry in vacuum (spontaneous symmetry breaking). The gauge bosons and fermions interact with the Higgs field to gain masses. This process is called Higgs mechanism. The SM formulation of the Higgs mechanism is briefly described in this section.

Denote the Higgs field ϕ as a doublet in the SU(2) space and expressed it below:

$$\phi = \frac{1}{\sqrt{2}} \begin{pmatrix} \phi_1 + i\phi_2 \\ \phi_3 + i\phi_4 \end{pmatrix} \tag{2.18}$$

The Lagrangian about the ϕ can be written as

$$L_\phi \equiv L_{Higgs} = T(\phi) - V(\phi) = (D_\mu \phi)^\dagger (D^\mu \phi) - \mu^2 \phi^\dagger \phi - \lambda(\phi^\dagger \phi)^2. \tag{2.19}$$

For $\mu^2 < 0$, the minimum of potential $V(\phi)$ is at

$$\phi^\dagger \phi = \frac{-\mu^2}{2\lambda} = \frac{\nu^2}{2}, \tag{2.20}$$

The real component of which can be written as

$$Real\ (\phi^\dagger \phi) = \frac{\phi_1^2 + \phi_2^2 + \phi_3^2 + \phi_4^2}{2} \tag{2.21}$$

From above expression we notice that there could be many solution to Equation 2.20. Therefore, we must choose a direction in SU(2) space. We choose the minimum, or vacuum ϕ_0 at,

$$\phi_0 = \frac{1}{\sqrt{2}}\begin{pmatrix}0\\ \nu\end{pmatrix}, \tag{2.22}$$

This implies $\phi_3 = \nu$ (the vacuum expectation value), and $\phi_1 = \phi_2 = \phi_4 = 0$. We can then study the spectrum by expanding ϕ field around the vacuum,

$$\phi(x) = \frac{1}{\sqrt{2}}\begin{pmatrix}0\\ \nu + H(x)\end{pmatrix}. \tag{2.23}$$

The Higgs potential $V(\phi)$ can be rewritten as

$$V(\phi) = -\frac{\mu^4}{4\lambda} - \mu^2 H^2 + \lambda\nu H^3 + \frac{\lambda}{4}H^4.$$

The second term in $V(\phi)$ represents the mass (at the tree-level) of the physical Higgs boson:

$$M_H = \sqrt{-2\mu^2} = \sqrt{2\lambda}\ \nu,$$

where λ is a parameter of the SM which is not specified in the model. The third and the 4th terms are the Higgs boson self-interaction terms.

Now we will see how the gauge bosons gain masses via the Higgs mechanism. When the scalar field $\phi(x)$ expanded around the a vacuum that with expectation value ν as shown in Equation 2.23, the kinematics term $T(\phi)$ in the Higgs field Lagrangian is expanded as:

$$\begin{aligned} T(\phi) = (D_\mu\phi)^\dagger(D^\mu\phi) = \frac{1}{2}(\partial_\mu H)^2 + \frac{g_1^2}{8}(W_\mu^1 - iW_\mu^2)(W^{1\mu} + iW^{2\mu})(\nu + H)^2 \\ + \frac{1}{8}(g_1 W_\mu^3 - g_2 B_\mu)(W^{3\mu} - g_2 B^\mu)(\nu + H)^2, \end{aligned} \tag{2.24}$$

which based on the definition in Equation 2.14 and 2.15, is rewritten as:

$$\begin{aligned} T(\phi) &= (D_\mu\phi)^\dagger(D^\mu\phi) \\ &= \frac{1}{2}(\partial_\mu H)^2 + \frac{1}{4}g_1^2 W_\mu^+ W^{-\mu}(\nu + H)^2 + \frac{1}{8}(g_1^2 + g_2^2)Z^\mu Z_\mu(\nu + H)^2 \\ &= \frac{1}{2}(\partial_\mu H)^2 + (\frac{1}{2}\nu g_2)^2 W_\mu^+ W^{-\mu} + \frac{1}{2}\nu {g_1}^2 W_\mu^+ W^{-\mu} H + \frac{1}{4}g_1^2 W_\mu^+ W^{-\mu} H^2 \\ &+ \frac{1}{2}(\frac{1}{2}\nu\sqrt{g_1^2 + g_2^2})^2 Z_\mu Z^\mu + \frac{1}{4}\nu(g_1^2 + g_2^2)Z_\mu Z^\mu H + \frac{1}{8}(g_1^2 + g_2^2)Z_\mu Z^\mu H^2. \end{aligned} \tag{2.25}$$

From the terms:

$$(\frac{1}{2}\nu g_2)^2 W_\mu^+ W^{-\mu} + \frac{1}{2}(\frac{1}{2}\nu\sqrt{g_1^2+g_2^2})^2 Z_\mu Z^\mu, \tag{2.26}$$

we see that the charged $W^\pm$ boson has acquired a mass of

$$m_W = \frac{1}{2}\nu g_2, \tag{2.27}$$

the neutral Z boson has acquired a mass of

$$m_Z = \frac{1}{2}\nu\sqrt{g_1^2+g_2^2}, \tag{2.28}$$

and the photon remains zero mass. Using the masses of the $W^\pm$ and Z boson defined in Equation 2.27 and 2.28, the kinematic term shown in Equation 2.25 is rewritten as:

$$\begin{gathered} T(\phi) = (D_\mu\phi)^\dagger(D^\mu\phi) \\ = \frac{1}{2}(\partial_\mu H)^2 + {m_W}^2 W^{+\mu}W_\mu^- + \frac{2{m_W}^2}{\nu}W^{+\mu}W_\mu^- H + \frac{{m_W}^2}{\nu^2}W^{+\mu}W_\mu^- H^2 \\ + \frac{1}{2}{m_Z}^2 Z^\mu Z_\mu + \frac{{m_Z}^2}{\nu}Z^\mu Z_\mu H + \frac{{m_Z}^2}{2\nu^2}Z^\mu Z_\mu H^2 \end{gathered} \tag{2.29}$$

which describes Higgs boson kinematics, the masses of $W^\pm$ and Z bosons, the triple and quartic boson interactions of the $W^\pm$/Z boson and the Higgs boson with the coupling proportional to the mass of the gauge boson squared. Such coupling is referred to as gauge coupling of the Higgs boson.

To explain how the fermions acquire mass, we add an interaction term to the previous Lagrangian of the electron (as an example) to describe the interaction of fermions with the Higgs field:

$$L_{Yukawa}^e = g_e(\overline{L_e}\phi e_R^- + \phi^\dagger\overline{e_R^-}L_e) \tag{2.30}$$

This Lagrangian is invariant under the $U(1)\times SU(2)$ transformation. We then expand the field ϕ around its vacuum by substituting Equation 2.23 into Equation 2.30, the interaction term becomes

$$L_{Yukawa}^e = \frac{g_e\nu}{\sqrt{2}}(\overline{e_L^-}e_R^- + \overline{e_R^-}e_L^-) + \frac{g_e}{\sqrt{2}}(\overline{e_L^-}e_R^- + \overline{e_R^-}e_L^-)H \tag{2.31}$$

where the first term shows that the electron mass is

$$m_e = \frac{g_e \nu}{\sqrt{2}} \tag{2.32}$$

The second term represents the interaction between electron and the Higgs boson with the interaction coupling proportional to the electron mass. Such coupling is called Yukawa coupling.

Similarly, the interaction of quarks (the first generation u, d quarks used here as an example) with the Higgs field can be written as below where the first two terms are the mass terms and the last two terms describe the interaction of d and u quarks with H.

$$L^Q_{Yukawa} = g_d \overline{Q_L} \phi d_R + g_u \overline{Q_L} \phi_c u_R + Herm.\ conjugate \tag{2.33}$$

which is

$$L^Q_{Yukawa} = m_d \bar{d} d + m_u \bar{u} u + \frac{m_d}{\nu} \bar{d} d H + \frac{m_u}{\nu} \bar{u} u H \tag{2.34}$$

This procedure for electron, and for the first generation of quarks acquire mass can be applied to the second and third generations of leptons and quarks by making the substitutions of $e \to \mu, \tau$; and $u \to c, t$, and $d \to s, b$.

2.1.3 Natural Unit

Natural units are customarily used to simplify formulas and calculations in physics by normalizing to unity the chosen constant physical quantities. Normally, only Planck constant ($\hbar$) and the speed of light in vacuum (c) are set to unity, $\hbar = c = 1$. The energy, momentum and mass then share the same unit, e.g. MeV, GeV, TeV. Conversions between units are based on the actual numerical expressions of $\hbar$ and c:

$$\hbar = 6.58 \times 10^{-25}\ \text{GeV} \cdot \text{s}, \tag{2.35}$$

$$c = 3.00 \times 10^{9}\ \text{m}. \tag{2.36}$$

These expressions provide two version factors written below, which can convert e.g. particle widths to lifetimes and to express cross sections in barn (b):

$$1\text{GeV} = 1.52 \times 10^{24}\ \text{sec}^{-1}, \tag{2.37}$$

$$1\text{GeV}^{-2} = 3.90 \times 10^{-28}\ \text{cm}^2 = 3.90 \times 10^{-4}\ \text{b}. \tag{2.38}$$

2.2 Higgs Boson Phenomenology at the LHC

2.2.1 Phenomenology of Proton-Proton Collisions

A proton consists of partons: quarks and gluons. In proton-proton (pp) collisions at the LHC, the parton interactions can be classified into hard and soft scattering processes depending on the momentum transfer between the interacting partons. A hard scattering process involves large momentum transfer, which could be either a violent scatter or creation of a system of large mass. A pp collision event at LHC is illustrated in Figure 2.2. The main theoretical components of this process is described

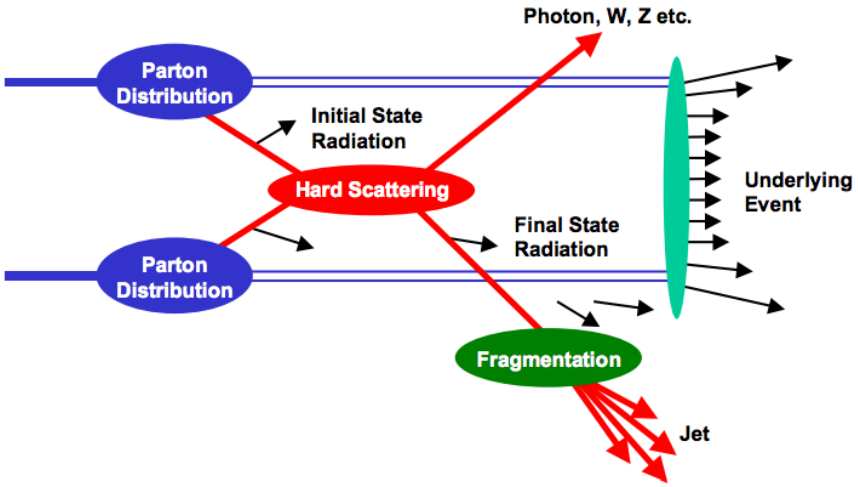

Figure 2.2: Schematic view of a hadron-hadron collision.

below:

- **Parton Distribution Function (PDF)** gives the probability of finding a certain type of quark or gluon carrying momentum fraction x at an energy scale Q. Figure 2.3 [28] shows the measured PDFs of gluon and quarks in NNPDF3.0 which is accurate in perturbative QCD at NNLO [29].

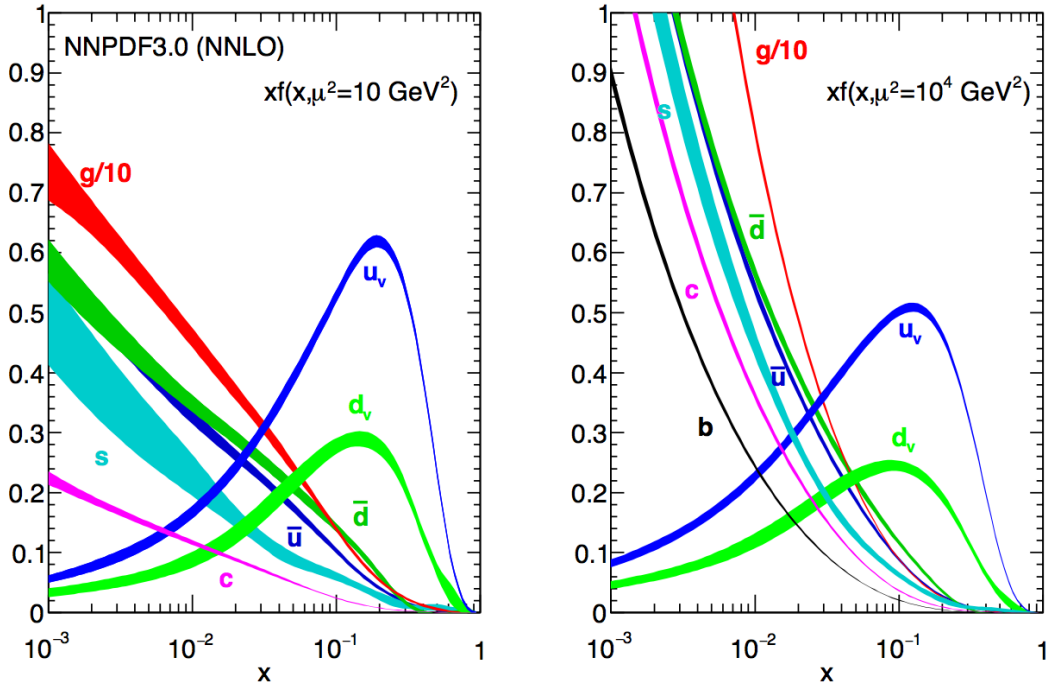

Figure 2.3: NNPDF3.0 NNLO PDF set for $Q^2 = 10$ GeV^2 and $Q^2 = 10^4$ GeV^2.

- **Hard Scattering** represents the event produced by parton interactions, such as the Higgs boson production from the gluon-gluon fusion and the decay products in final state from the underlying physics process. For example, Higgs decays to vector bosons or quark pairs in final states.

- **Jet Fragmentation and Hadronization** produces the hadronic jets in the final state from the partons (quarks and gluons) which are produced in the hard scattering.

- **Initial and Final State Radiation** comes from the QCD or QED radiations from the incoming and outgoing partons.

- **Underlying Event** includes particles produced by proton remnants.

The fundamental connection between theory and experimental measurement is the cross section (σ) for a given physics process. As an example of Higgs production through gluon-gluon fusion and decay to ZZ^* process, the cross section can be calculated as a convolution of the PDF for the incoming gluons ($F_{g_1}(x_1, Q^2), F_{g_2}(x_2, Q^2)$), and the parton level hard-scattering cross section of $\hat{\sigma}_{g_1 g_2 \to H \to ZZ^*}(\alpha_s, \mu_F, \mu_R)$, which

can be written as:

$$\sigma = \sum_{g_1,g_2} \int dx_1 dx_2 F_{g_1}(x_1, Q^2) F_{g_2}(x_2, Q^2) \hat{\sigma}(\alpha_s, \mu_F, \mu_R). \tag{2.39}$$

where μ_F and μ_R are the QCD factorization and renormalization scales. The scale Q in PDF is often using the μ_F, which separates the long and short distance physics. Parton level hard-scattering cross-section depends on both μ_F and μ_R. It can be calculated perturbatively in QCD in form of the fixed-order expansion in α_s. The calculation with tree-level diagrams gives the leading-order (LO) partonic cross section. For LHC physics analysis, most of the theoretical calculations are performed with higher-order corrections, including the next-to-leading-order (NLO), the next-to-next-to-the-leading order (NNLO), and the next-to-next-to-next-to-the-leading order (N^3LO). The choice of μ_F and μ_R is arbitrary. To avoid unnaturally large logarithms reappearing in the perturbation series, μ_F and μ_R often take a value in the order of the typical momentum scales of the hard-scattering process. In addition, $\mu_F = \mu_R$ is also often assumed. Taking the Higgs production through gluon-gluon fusion and decay to $ZZ^* \to 4\ell$ process as an example, the standard choice for Higgs cross section calculation is $\mu_F = \mu_R = \frac{m_{4\ell}}{2}$.

2.2.2 SM Higgs Boson Production at the LHC

At the LHC, in the SM the Higgs production is dominated by the gluon fusion (ggF) process through a loop diagram at leading order, due to the large gluon density in the protons. The subleading Higgs boson production mode is the vector-boson fusion (VBF) mechanism, which has a production cross section about one order of magnitude smaller than that of the ggF. Events produced via the VBF mechanism is characterized by two energetic jets produced in the forward region in the final state with large rapidity separations. Following next is the vector-boson associated production (VH) mechanisms, where the associated vector boson offers a distinct experimental signature to help select events produced via this mechanism. Higgs boson production in association with a top or bottom quark pair is more rare, each of which contributes to only about 1% of the total Higgs boson production cross section. The presence of top quark (pair) in the final state offers a distinct experimental signature to isolate ttH events. The b quark (pair) in the bbH process is quite soft and similar in kinematics to the gluons emitted in the ggF process, which makes it very difficult to detect bbH process at the LHC. Representative tree-level Feynman diagrams for these dominant Higgs boson production processes are shown in Figure 2.4.

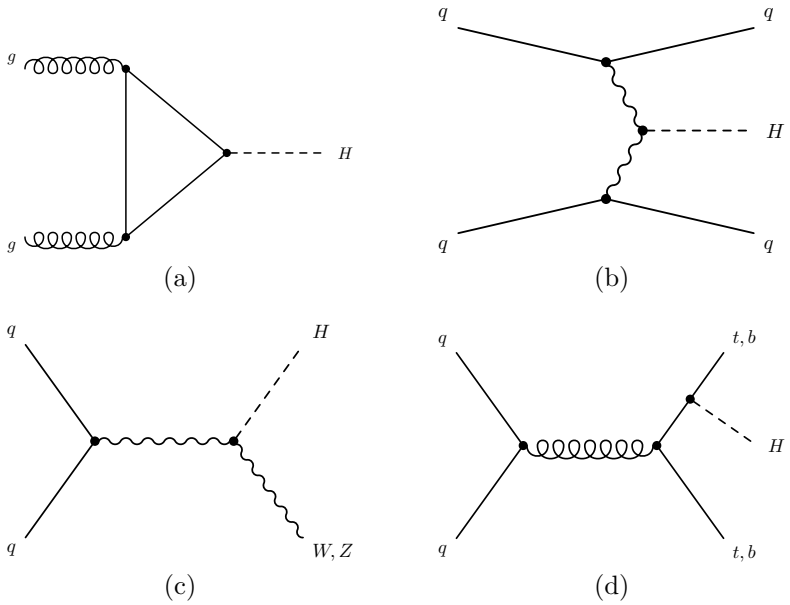

Figure 2.4: Representative tree-level Feynman diagrams for leading Higgs boson production mechanism at the LHC: The ggF (2.4a), VBF (2.4b), VH (2.4c) and ttH/bbH (2.4d).

The Higgs boson production cross sections are summarized in Table 2.1, for different Higgs production processes assuming a mass of 125.09 GeV, the central value of the result from the combined measurement of the Higgs boson mass with the ATLAS and CMS experiments using the full Run 1 dataset [30].

2.2.3 SM Higgs Boson Decays

The main SM Higgs decay channels with their expected branching ratios at the measured Higgs boson mass of 125.09 GeV are summarized in Table 2.2.

Representative tree-level Feynman diagrams for various Higgs boson decay processes are shown in Figure 2.5. The two leading Higgs decay channels are $b\bar{b}$ and WW. The $H \to ZZ^* \to 4\ell$ decay channel only has a branching ratio of about 0.013%. Despite its very tiny branching ratio, many advantages such as the excellent signal over background ratio and good mass resolution, make the $H \to ZZ^* \to 4\ell$ decay channel one of the channels contributing to Higgs boson discovery and a golden channel to measure many of the Higgs boson properties after the discovery.

Production mechanism	Cross section (pb)			
	$\sqrt{s} = 7$ TeV	$\sqrt{s} = 8$ TeV	$\sqrt{s} = 13$ TeV	Order of calculation
ggF	15.3 ± 0.7	21.4 ± 1.1	48.5 ± 2.4	N^3LO
VBF	1.24 ± 0.06	1.60 ± 0.04	3.78 ± 0.08	NLO
WH	0.576 ± 0.012	0.70 ± 0.015	1.37 ± 0.03	NLO
ZH	0.338 ± 0.011	0.420 ± 0.014	0.882 ± 0.04	NLO
bbH	0.155 ± 0.035	0.202 ± 0.045	0.486 ± 0.12	NLO
ttH	0.089 ± 0.009	0.133 ± 0.013	0.507 ± 0.05	NLO
Total	17.7 ± 0.7	24.5 ± 1.1	55.5 ± 2.4	

Table 2.1: Standard Model Higgs boson production cross sections at $m_H = 125.09$ GeV at center-of-mass energy $\sqrt{s} = 7$, 8 and 13 TeV at the LHC. The uncertainties on the cross sections are the quadratic sum of the uncertainties from variations of QCD scales, parton distribution functions and the strong interaction coupling, α_s.

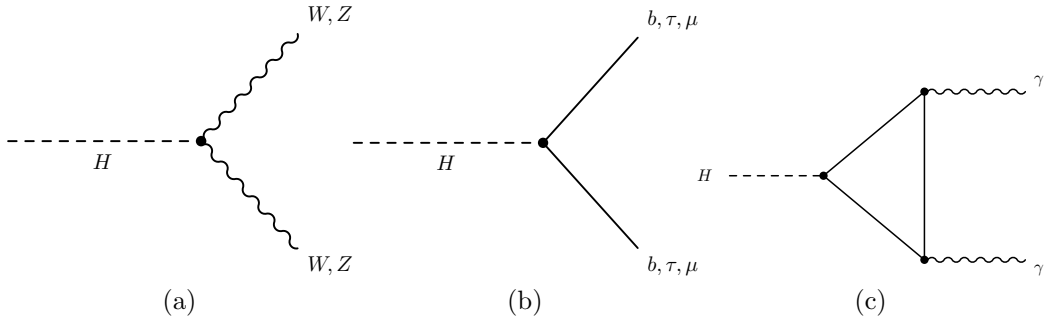

Figure 2.5: Representative leading-order Feynman diagrams for Higgs boson decay to a pair of W or Z bosons (2.5a), fermions (2.5b), and photons (2.5c).

Decay channel	Branching ratio (%)
$H \to b\bar{b}$	57.1 ± 1.9
$H \to WW^*$	22.0 ± 0.9
$H \to gg$	8.53 ± 0.85
$H \to tt$	6.26 ± 0.35
$H \to cc$	2.88 ± 0.35
$H \to ZZ^*$	2.73 ± 0.11
$H \to \gamma\gamma$	0.228 ± 0.011
$H \to Z\gamma$	0.157 ± 0.014
$H \to \mu\mu$	0.022 ± 0.001

Table 2.2: Standard Model Higgs boson decay branching ratios at $m_H = 125.09$ GeV.

2.2.4 Beyond the Standard Model

It has been a question whether the newly discovered scalar particle is indeed the SM predicted Higgs boson. There are alternative theoretical models predicting new particles like the discovered new boson. This section gives brief descriptions of the models beyond the SM, which will be tested using data collected by the ATLAS detector at the LHC.

2.2.4.1 Spin and Parity

In this dissertation, the tensor structure of the Higgs boson coupling to vector bosons is studied using the Higgs boson characterization model [31, 32], which uses an effective Lagrangian approach for the description of beyond Standard Model (BSM) interactions. The EFT approach is only valid up to a certain energy scale, Λ, which is set to 1 TeV based on no evidence of new physics below this energy scale has been shown up in the experimental results obtained at the LHC and from previous collider experiments. Two BSM scenarios for the spin and parity of the boson are tested in the spin and parity studies:

- a BSM spin-0 CP-even or CP-odd Higgs boson,
- a spin-2 particle.

In both cases, the studied particle is assumed to have a mass of about 125 GeV, and a narrow width significantly smaller than the experiment detector resolution, thus interference effects between the studied particle and backgrounds can be neglected.

The $J^P = 1^{\pm}$ hypothesis is not tested in this dissertation, considering that the $H \to \gamma\gamma$ decay channel has been observed, which is forbidden by the Landau–Yang theorem [33, 34] for a spin-1 particle. Moreover, the spin-1 hypothesis has already been studied in the previous ATLAS publication [35] in the $H \to ZZ^*$ and $H \to WW^*$ decays and has been excluded at more than 99% CL.

2.2.4.2 The spin-0 hypothesis

In the Higgs boson characterization model, the spin-0 particle (X) interacting with pairs of W or Z bosons, is given through the following general interaction Lagrangian:

$$\begin{aligned}\mathcal{L}_0^V = & \left\{\cos(\alpha)\kappa_{\rm SM}\left[\tfrac{1}{2}g_{HZZ}Z_\mu Z^\mu + g_{HWW}W_\mu^+W^{-\mu}\right]\right. \\ & -\tfrac{1}{4}\tfrac{1}{\Lambda}\left[\cos(\alpha)\kappa_{HZZ}Z_{\mu\nu}Z^{\mu\nu} + \sin(\alpha)\kappa_{AZZ}Z_{\mu\nu}\tilde{Z}^{\mu\nu}\right] \\ & \left.-\tfrac{1}{2}\tfrac{1}{\Lambda}\left[\cos(\alpha)\kappa_{HWW}W_{\mu\nu}^+W^{-\mu\nu} + \sin(\alpha)\kappa_{AWW}W_{\mu\nu}^+\tilde{W}^{-\mu\nu}\right]\right\}X.\end{aligned} \tag{2.40}$$

Here V^μ represents the vector-boson field ($V = Z, W^\pm$), the $V^{\mu\nu}$ are the reduced field tensors and the dual tensor is defined as $\tilde{V}^{\mu\nu} = \frac{1}{2}\varepsilon^{\mu\nu\rho\sigma}V_{\rho\sigma}$. The symbols $\kappa_{\rm SM}$, κ_{HVV} and κ_{AVV} denote the coupling constants corresponding to the interaction of the SM, BSM CP-even or BSM CP-odd spin-0 particle, represented by the X field, with ZZ or WW pairs, and the mixing angle α allows for production of CP-mixed states.

In our analysis, the SM Higgs boson hypothesis ($J^P = 0^+$) is tested against two alternatives: the CP-odd $J^P = 0^-$ and the BSM CP-even $J^P = 0_h^+$ hypotheses, with the corresponding values of the couplings listed in Table 2.3.

J^P	Model	Values of tensor couplings			
		$\kappa_{\rm SM}$	κ_{HVV}	κ_{AVV}	α
0^+	SM Higgs boson	1	0	0	0
0_h^+	BSM spin-0 CP-even	0	1	0	0
0^-	BSM spin-0 CP-odd	0	0	1	$\pi/2$

Table 2.3: Parameters of the benchmark scenarios for spin-0 boson tensor couplings used in tests (see Eq. (2.40)) of the fixed spin and parity models.

2.2.4.3 The spin-2 hypothesis

In the Higgs boson characterization model [32], the description of the interaction of a spin-2 particle with fermions and vector bosons is described by the following Lagrangian:

$$\mathcal{L}_2 = -\frac{1}{\Lambda}\left[\sum_V \kappa_V \mathcal{T}_{\mu\nu}^V X^{\mu\nu} + \sum_f \kappa_f \mathcal{T}_{\mu\nu}^f X^{\mu\nu}\right]. \tag{2.41}$$

Inspired by gravitation theories, the spin-2 tensor field $X^{\mu\nu}$ is chosen to interact with the gauge-boson and fermion energy-momentum tensors, $\mathcal{T}_{\mu\nu}^V$ and $\mathcal{T}_{\mu\nu}^f$, of vector bosons V and fermions f, with coupling constants κ_V and κ_f.

In the benchmark models studied in this dissertation, the universal couplings (UC) scenario refers to the hypothesis that vector-boson couplings: κ_W, κ_Z, and κ_γ, are independent of all the other couplings and $\kappa_q = \kappa_g$; while in the non-universal couplings (non-UC) scenario, κ_q/κ_g ratio is chosen to be zero or two. In the non-UC scenario, the spin-2 model predicts an enhancement of the tail in the distribution of the transverse momentum, p_{T}^X. In analysis, a selection of $p_{\mathrm{T}}^X < 300$ GeV is applied to the non-UC scenarios, and a second more conservative selection $p_{\mathrm{T}}^X < 125$ GeV is also performed, considering that the EFT must describe the physics at least up to the mass of the observed resonance. The values of the couplings, p_{T}^X selections and the corresponding spin-2 benchmark scenarios are listed in Table 2.4.

Values of spin-2 quark and gluon couplings		p_{T}^X selections (GeV)	
$\kappa_q = \kappa_g$	Universal couplings	–	–
$\kappa_q = 0$	Low light-quark fraction	< 300	< 125
$\kappa_q = 2\kappa_g$	Low gluon fraction	< 300	< 125

Table 2.4: The values of the couplings to quarks κ_q and to gluons κ_g, the transverse momentum p_{T}^X of the spin-2 resonance selections and the corresponding spin-2 benchmark scenarios.

2.2.4.4 Higgs Boson Coupling Modifiers

Signal-strength parameter is a measure of potential deviations from the SM prediction under the assumption that the Higgs boson production and decay kinematics do not change appreciably from the SM expectations. For the process of Higgs boson produced via mechanism i and decaying to final state f, i.e. $i \to H \to f$, the signal-strength parameter μ_i^f is defined as the ratio between the Higgs boson rate measured experimentally and its SM expectation:

$$\mu_i^f = \frac{\sigma_i \times BR^f}{\sigma_{i,SM} \times BR_{SM}^f} \tag{2.42}$$

An inclusive signal-strength parameter μ is a common scale factor for all considered Higgs boson production mechanisms and decay processes. The measurement of μ is the most model dependent and also the most precise among all the Higgs boson rate measurements presented in this thesis. By definition, $\mu = 0$ corresponds to the background-only model while $\mu = 1$ corresponds to the signal plus background model assuming the SM Higgs boson as the signal process.

The measurements of Higgs boson couplings presented in Chapter VIII of this dissertation are performed using a leading-order tree-level motivated framework, referred to as the κ-framework, following the approach and benchmarks recommended by the LHC Higgs Cross Section Working Group [31] and [36]. This framework is designed to quantify possible deviations in the data from the SM predictions in terms of the Higgs boson couplings to the SM fermions and bosons. It is based on the following assumptions:

- The mass of the Higgs boson is assumed to be the central value of the ATLAS and CMS combined mass measurement of $m_H = 125.09$ GeV;
- The width of the Higgs boson is very narrow (~ 4 MeV), justifying the use of the zero-width approximation;
- Only modifications of coupling strengths are considered, while the tensor structure is assumed to be the same as the SM, thus the spin and parity quantumn numbers are assumed to be $J^P = 0^+$.

In this framework, the cross section for the process $i \to H \to f$ can be decomposed as the SM cross sections and widths scaled by coupling modifiers, as expressed in the following equation:

$$\sigma_i \cdot BR^f = \frac{\sigma_i \cdot \Gamma_f}{\Gamma_H} = \frac{\sigma_i^{SM} \cdot \Gamma_f^{SM}}{\Gamma_H^{SM}} \cdot \frac{\kappa_i^2 \cdot \kappa_f^2}{\kappa_H^2} \tag{2.43}$$

where σ_i is the production cross section through the initial state i, BR^f and Γ_f are the branching ratio and partial decay width into the final state f, respectively. Γ_H denotes the total width of the Higgs boson. $\kappa_H, \kappa_i, \kappa_f$ are the coupling modifiers for the Higgs boson total width, production and decay process. κ_H^2 is defined as the sum of squared coupling modifiers for all Higgs decay channels κ_f^2 weighted by the corresponding SM partial decay width Γ_f^{SM}:

$$\kappa_H^2 = \sum_f \frac{\kappa_j^2 \Gamma_f^{SM}}{\Gamma_H^{SM}} \tag{2.44}$$

where the summation of the SM partial decay width Γ_f^{SM} includes the decay channel $WW, ZZ, \gamma\gamma, Z\gamma, gg, tt, bb, cc, ss, \tau\tau$ and $\mu\mu$. The contributions from up and down quarks and electron are negligible.

Considering the $H \to ZZ^* \to 4\ell$ channel alone is not able to measure all the Higgs boson coupling modifiers, additional assumptions are made in order to study

two coupling modifiers: the Higgs boson coupling to fermions κ_F and the coupling to bosons κ_V. These additional assumptions are presented below.

First, it is assumed that there is no new particle in the loops. The effective coupling modifiers for the loop-induced Higgs boson production and decay modes then can be parametrized in terms of coupling modifiers to the SM fermions and vector bosons. For example, the effective coupling modifiers for ggF production and $H \to \gamma\gamma$ decay are given by:

$$\kappa_g^2 \equiv \frac{\kappa_t^2 \sigma_{ggF}^{tt} + \kappa_b^2 \sigma_{ggF}^{bb} + \kappa_t \kappa_b \sigma_{ggF}^{tb}}{\sigma_{ggF}^{tt} + \sigma_{ggF}^{bb} + \sigma_{ggF}^{tb}} = 1.06\kappa_t^2 + 0.01\kappa_b^2 - 0.07\kappa_t\kappa_b, \tag{2.45}$$

and

$$\kappa_{\gamma\gamma}^2 \equiv \frac{\sum_{i,j(i\geq j)} \kappa_i \kappa_j \Gamma_{\gamma\gamma}^{ij}}{\sum_{i,j(i\geq j)} \Gamma_{\gamma\gamma}^{ij}} = 1.59\kappa_W^2 + 0.07\kappa_t^2 - 0.66\kappa_W\kappa_t. \tag{2.46}$$

Furthermore, assuming there is no BSM decay process, the coupling modifier for the total width κ_H defined in Equation 2.44 takes the form:

$$\begin{aligned} \kappa_H^2 = 0.57\kappa_b^2 + 0.22\kappa_W^2 + 0.09\kappa_g^2 + 0.06\kappa_t^2 + 0.03\kappa_Z^2 + 0.03\kappa_c^2 \\ +0.0023\kappa_{\gamma\gamma}^2 + 0.0016\kappa_{Z\gamma}^2 + 0.0001\kappa_s^2 + 0.00022\kappa_\mu^2. \end{aligned} \tag{2.47}$$

Finally, we assume that all vector boson modifiers are the same and denoted as κ_V,

$$\kappa_V = \kappa_Z = \kappa_W \tag{2.48}$$

all fermion coupling modifiers are the same as κ_F,

$$\kappa_F = \kappa_t = \kappa_b = \kappa_c = \kappa_s = \kappa_\tau = \kappa_\mu, \tag{2.49}$$

κ_H is then deduced to the simple formula:

$$\kappa_H^2 = (0.75\kappa_F)^2 + (0.25\kappa_V)^2. \tag{2.50}$$

Figure 2.6 illustrates the introduction of the κ_V and κ_F in the process of Higgs boson production via gluon fusion production mechanism and decaying to ZZ^*. The ratio of the measured cross section over the SM prediction in the Higgs boson production in the ZZ^* decay channel, which has been defined previously as $\mu_i^{ZZ^*}$, can be parametrized below in the case of fermion-mediated Higg boson production mech-

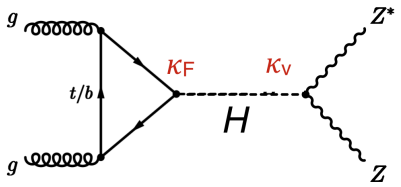

Figure 2.6: Couplings modifiers κ_V, κ_F, for a LO diagram $gg \to H \to ZZ^*$.

anism:

$$\mu_i^{ZZ^*} = \frac{\sigma \cdot BR\ (i \to H \to ZZ)}{(\sigma \cdot BR\ (i \to H \to ZZ))_{SM}} = \frac{(\kappa_V \kappa_F)^2}{(0.75\kappa_F)^2 + (0.25\kappa_V)^2} \tag{2.51}$$

where i denotes ggF, ttH or bbH production mechanisms, and in the case of boson-mediated production process:

$$\mu_i^{ZZ^*} = \frac{\sigma \cdot BR\ (i \to H \to ZZ)}{(\sigma \cdot BR\ (i \to H \to ZZ))_{SM}} = \frac{\kappa_V^4}{(0.75\kappa_F)^2 + (0.25\kappa_V)^2} \tag{2.52}$$

where i denotes VBF or VH production mechanisms.

Measuring the Higgs boson couplings is a powerful approach to search for new physics. There are questions unanswered by the SM, such as the hierarchy problem and the nature of dark matter. There are extensions to the SM in the Higgs sector to provide possible explanations to these questions. In some theories more than one Higgs doublet is predicted, leading to the existence of more than one Higgs boson. Minimal Composite Higgs Models (MCHM) [38, 39, 40, 41, 42, 43] represent a possible explanation for the scalar naturalness problem, where the Higgs boson is a composite, pseudo-Nambu-Goldstone boson rather than an elementary particle. The Higgs boson coupling measurements have sensitivity to these new physics phenomena, for example combining the measurement of Higgs boson couplings to fermions and vector bosons in $H \to \gamma\gamma$, $H \to ZZ^*$, $H \to WW^*$, $H \to Z\gamma$, $H \to b\bar{b}$, $H \to \tau\tau$, $H \to \mu\mu$ decay channels and using the Run 1 data, lower limits at the 95% CL on the Higgs boson compositeness scale λ in the MCHM4 and MCHM5 models are set to be 710 GeV and 780 GeV respectively [44]. Figure 2.7 shows the two-dimensional contours at 68% CL and 95% CL in the κ_V versus κ_F couplings modifier plane as reference together with the couplings modifier predicted in the MCHM4 and MCHM5 models are shown as parametric functions of the Higgs boson compositeness scaling parameter $\xi = \nu^2/\lambda^2$ where ν is the SM vacuum expectation value. ξ is contrained by the coupling measurements since it is related to κ_F and κ_V in the MCHM4 model

by the formula:

$$\kappa_F = \kappa_V = \sqrt{1-\xi}, \tag{2.53}$$

and in the MCHM5 model:

$$\kappa_V = \sqrt{1-\xi}, \tag{2.54}$$

$$\kappa_F = \frac{1-2\xi}{\sqrt{1-\xi}}. \tag{2.55}$$

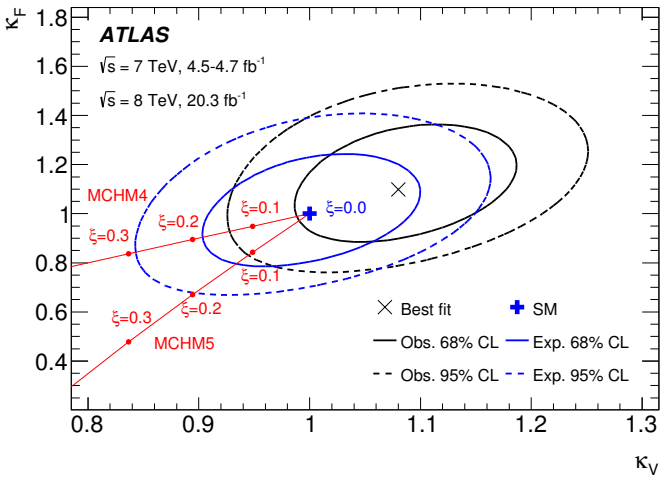

Figure 2.7: Two-dimensional likelihood contours at 68% CL and 95% CL in the κ_V vs. κ_F couplings modifier plane. The couplings modifiers predicted in the MCHM4 and MCHM5 models are shown as parametric functions of the Higgs boson compositeness scaling parameter ξ.

CHAPTER III

The Large Hadron Collider and the ATLAS Experiment

3.1 The Large Hadron Collider

3.1.1 Introduction

The Large Hadron Collider (LHC) [18] is the latest addition to the CERN's accelerator complex shown in Figure 3.1 [45], which is installed in a deep underground tunnel with a circumference of 27 kilometers, beneath the France and Switzerland border near Geneva, Switzerland. It is a superconducting circular accelerator at the energy frontier, operating at proton-proton (pp), lead-lead (Pb-Pb) and proton-lead (p-Pb) collision modes. Before the particles are injected into the LHC, their energies are boosted in a sequence of several accelerators. In the pp collision mode, protons are first accelerated in Linear accelerator 2 (Linac 2) to an energy of 50 GeV, then injected to the Proton Synchrotron Booster and accelerated to 1.4 GeV. Afterwards, the Proton Synchrotron (PS) and the Super Proton Synchrotron (SPS) boosts the particle beam to 25 GeV and 450 GeV. Finally, the protons are injected to the two beam pipes of the LHC. They are accelerated to reach a maximun beam energy of 6.5 TeV so far. The two beams travel in opposite directions and collide at center-of-mass energy ($\sqrt{s}$) of 13 TeV at four interaction points (IP), outside which four particle detectors are constructed to record the events produced in the particle collisions. The four detectors and their main physics goals are summarized below:

- **ALICE** (A Large Ion Collider Experiment): A heavy-ion detector to study the physics of strongly interacting matter at extreme energy densities, in the form of quark-gluon plasma;

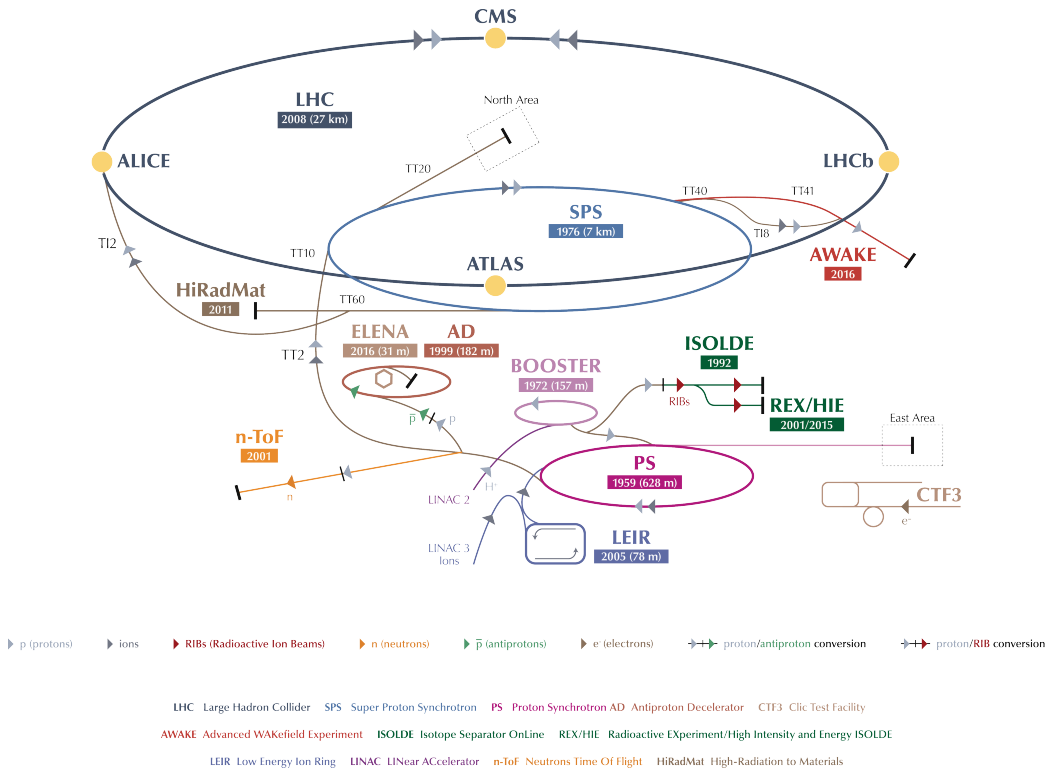

Figure 3.1: Schematic view of CERN's accelerator complex.

- **ATLAS** (A Toroidal LHC Apparatus): One of the two general purpose detectors to probe a wide range of physics including tests of the SM at the energy frontier and searching for the Higgs boson, supersymmetry, dark matter and etc.;
- **CMS** (Compact Muon solenoid): The other general purpose detector;
- **LHCb** (Large Hadron Collider beauty): A b-physics detector to measure the parameters of CP violation in the interactions of b-hadrons.

3.1.2 Luminosity

Luminosity (L) is defined as the ratio of event rate ($\frac{dN}{dt}$) over the cross section (σ) of the process in which the event is produced,

$$\frac{dN}{dt} = L \times \sigma. \tag{3.1}$$

It is an important parameter to characterize the performance of the LHC. It represents the number of particles per area per time in collisions, and is thus expressed in unit

of $cm^{-2}s^{-1}$. luminosity is solely determined by beam parameters [46]. Assuming a Gaussian beam distribution, the luminosity can be expressed as:

$$L = \frac{N_b^2 n_b f_{rev} \gamma_r}{4\pi \epsilon_n \beta^*} F, \tag{3.2}$$

where N_b is the number of particles per bunch, n_b the number of bunches per beam, f_{rev} the revolution frequency, γ_r the relativistic gamma factor, ϵ_n the normalized transverse beam emittance, β^* the beta function at the collision point, and F the geometric luminosity reduction factor due to the crossing angle at the IP, which can be calculated as:

$$F = 1/\sqrt{1 + (\frac{\theta_c \sigma_z}{2\sigma^*})^2}, \tag{3.3}$$

where θ_c is the full crossing angle at the IP, σ_z the root mean square (RMS) of bunch length and σ^* the transverse RMS of beam size at the IP and assuming equal beam parameters for both circulating beams.

The intergral of the luminosity with respect to time (L_{int}):

$$L_{int} = \int L dt \tag{3.4}$$

which is called as the integrated luminosity, characterizes the data size in a certain collision time. It is expressed in unit of inverse femtobarn (fb^{-1}) [1] in this dissertation, and measures the number of events produced per fb cross section.

At the LHC, multiple *pp* collision events are expected to happen during a single bunching crossing. The average number of *pp* inelastic interactions per bunch crossing, often referred to as pile-up parameter (μ), poses as an experimental challenge. These collision events are uncorrelated with the hard-scattering process, and can be approximated as contributing a background of soft energy depositions that have particularly adverse and complex effects on the jet reconstruction [47]. The pile-up parameter can be calculated as the integrated luminosity in a bunching crossing time multiplied by the inelastic interaction cross section (σ_{inel}):

$$\mu = \int_0^{t^{\text{crossing}}} L dt \times \sigma_{inel}. \tag{3.5}$$

The values of the inelastic cross section at center-of-mass energy of 8 and 13 TeV

[1] $fb^{-1} = 10^{39}$ cm^{-2}.

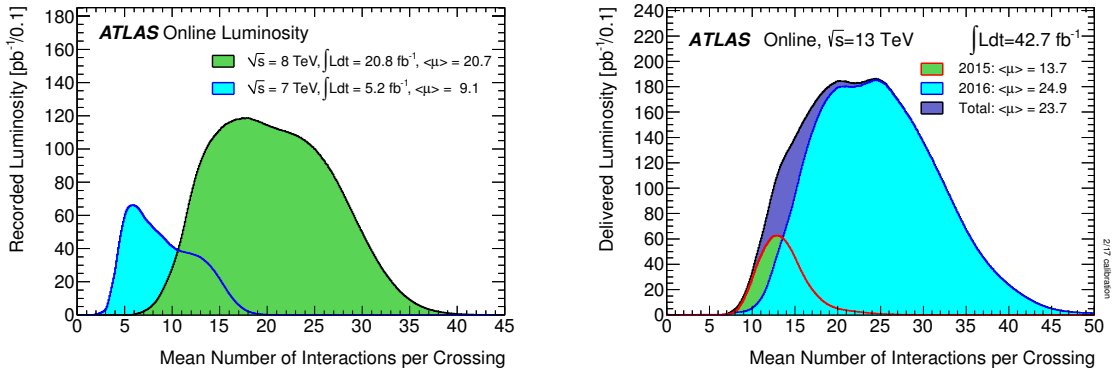

(a) (b)

Figure 3.2: The luminosity-weighted distribution of the mean number of interactions per crossing μ, in the pp collision data produced in $2011 - 2012$ (3.2a) recorded by the ATLAS detector and in $2015 - 2016$ (3.2b) delivered by the LHC.

are about 72 mb and 78 mb, respectively, calculated by Pythia8 generater [48]. The number of interactions averaged over all bunch crossings and averaged over the data are referred to as $< \mu >$. Figure 3.2 shows the luminosity-weighted distribution of μ, and the $< \mu >$ value in pp collision data at the LHC in years of 2011, 2012 [49], 2015 and 2016 [50].

Table 3.1 highlights the typical values of representative beam parameters under

Parameter	Design	2010	2011	2012	2015	2016
Beam energy [TeV]	7.0	3.5	3.5	4	6.5	6.5
Bunches/beam n_b	2808	348	1331	1380	2244	2220
Bunch crossing time t_{crossing} [ns]	25	150	50	50	25	25
Protons/bunch N_b [10^{11} protons]	1.15	0.9	1.2	1.7	1.1	1.1
ϵ_n [μ m]	3.75	2.6	2.4	2.4	3.5	3.4
β^* [m]	0.55	2.0-3.5	1.0-1.5	0.6	0.8	0.4
Peak luminosity [10^{34} cm^{-2}s^{-1}]	1.0	0.02	0.36	0.77	0.51	1.4
$< \mu >$	25	2	9	21	14	25
Integrated luminosity LHC delivered [fb^{-1}]		0.047	5.5	22.8	4.2	38.9

Table 3.1: Selected proton running conditions in the LHC operation in Run 1 (2010-2012) and in Run 2 (2013-2016) and the corresponding design parameters.

operational conditions of the LHC in pp collision mode in Run 1 from 2010 to 2012 and in Run 2 from 2015 to 2016. In 2016, the peak luminosity is up to $1.4\times$ $\mathrm{cm}^{-2}\mathrm{s}^{-1}$ which has surpassed the design value. The LHC operation has been remarkably well.

3.2 The ATLAS detector

The ATLAS detector [51] is a symmetric cylindrical multi-purpose detector, designed to be sensitive to a wide range of physics signatures to fully exploit the physics potential of the LHC at a nominal luminosity of 10^{34} $\mathrm{cm}^{-2}\mathrm{s}^{-1}$. The sub-detectors include the inner detector (ID), the electromagnetic (EM) and hadronic calorimeters, and the muon spectrometer (MS). A schematic view is shown in Figure 3.3.

The coordinate system used in the ATLAS dector is a right-handed Cartesian coordinate system with its origin at the IP, in the center of the detector. The positive x-axis points from the IP to the center of the LHC ring, the positive y-axis points upward, and the z-axis is along the beam direction. The side-A and side-C of the detector is with positive and negative z, respectively. The azimuthal angle ϕ is measured around the beam pipe. $\phi = 0$ corresponds to the positive x-axis and increases clockwise when looking into the positive z-axis direction. The polar angle θ measures the angle from the beam axis.

The nomenclatures used to describe the characteristics of the particles detected by the ATLAS detector are briefly introduced below. The componet of the particle momentum in the transverse (x-y) plane is called as the transverse momentum p_{T} ($p_{\mathrm{T}} = p \cdot sin(\theta)$). The projection of the energy in the transverse plane is referred to as the transverse energy E_{T}. It is related to the transverse momentum through $E_{\mathrm{T}} = \sqrt{p_{\mathrm{T}}^2 + m^2}$. The pseudorapidity is defined as $\eta = -\ln\tan(\theta/2)$. In case of a massive object, the rapidity is used $y = \frac{1}{2}\ln(\frac{E+p_Z}{E-p_Z})$. Another useful variable is the angular separation between two objects in the η-ϕ angle space, defined as $\Delta R = \sqrt{(\Delta\eta)^2 + (\Delta\phi)^2}$.

3.2.1 Inner Dectector

The ATLAS Inner Detector is designed to provide hermetic and robust pattern recognition, excellent momentum resolution and both primary and secondary vertex measurements for charged tracks above a given p_{T} threshold (about 0.5 GeV) in the pseudorapidity range of $\eta < 2.5$. It also provides electron identification within $\eta < 2.0$ and over a wide range of energies (0.5 GeV - 150 GeV). The ID is contained within a cylindrical envelope of length $\pm$3512 mm and of radius 1150 mm,

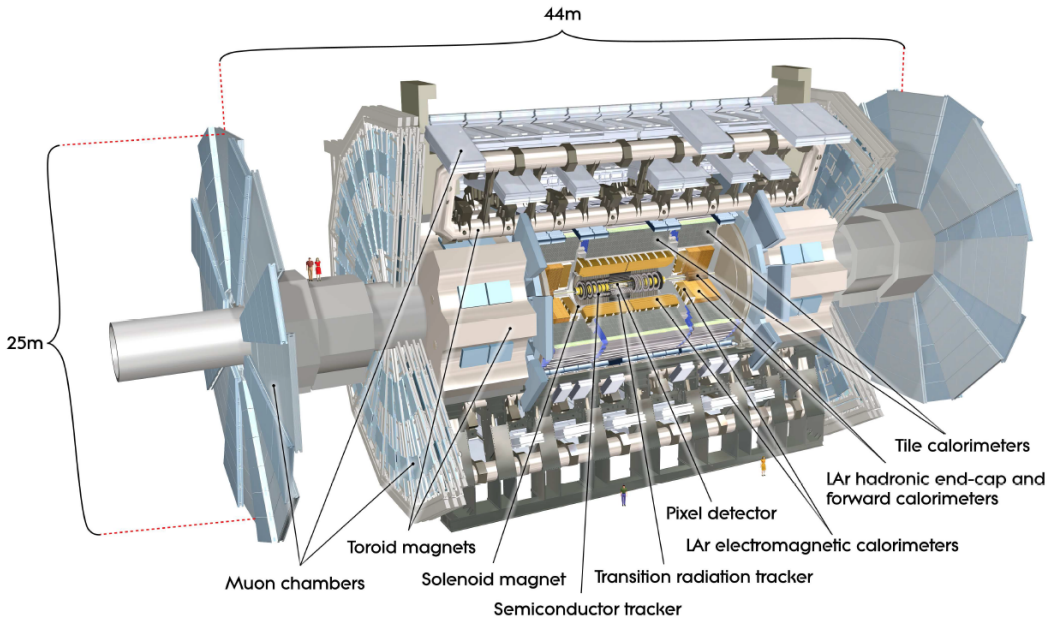

Figure 3.3: Cut-away view of the ATLAS detector.

and located at small radii from the beamline. It is immersed in a 2 T magnetic field produced by a thin superconducting solenoid located in front of the calorimeter. As illustrated in Figure 3.4 [52], the ID consists of three subdectors: fine-granularity pixel and microstrip detectors covering the range of $|\eta| < 2.5$, and a gas-filled straw-tube transition-radiation tracker (TRT) complementing the silicon tracker at larger radii and providing electron identification based on transition radiation. The parameters of the ID is summarized in Table 3.2.

Type	Position	Area (m^2)	Resolution $\sigma(\mu m)$	Channels (10^6)	η coverage
Pixels	IBL	0.2	$R\phi = 12$, $z = 66$	16	± 2.5
	2 barrel layers	1.4	$R\phi = 12$, $z = 66$	81	± 1.7
	5 end-cap disks	0.7	$R\phi = 12$, $z = 77$	43	$1.7 - 2.5$
Silicon	4 barrel layers	34.4	$R\phi = 16$, $z = 580$	3.2	± 1.4
strips	9 end-cap wheels	26.7	$R\phi = 16$, $z = 580$	3.0	$1.4 - 2.5$
TRT	Axial barrel straws		170 (per straw)	0.1	± 0.7
	Radial end-cap straws		170 (per straw)	0.32	$0.7 - 2.0$

Table 3.2: Parameters of the ID. The resolutions quoted are typical values.

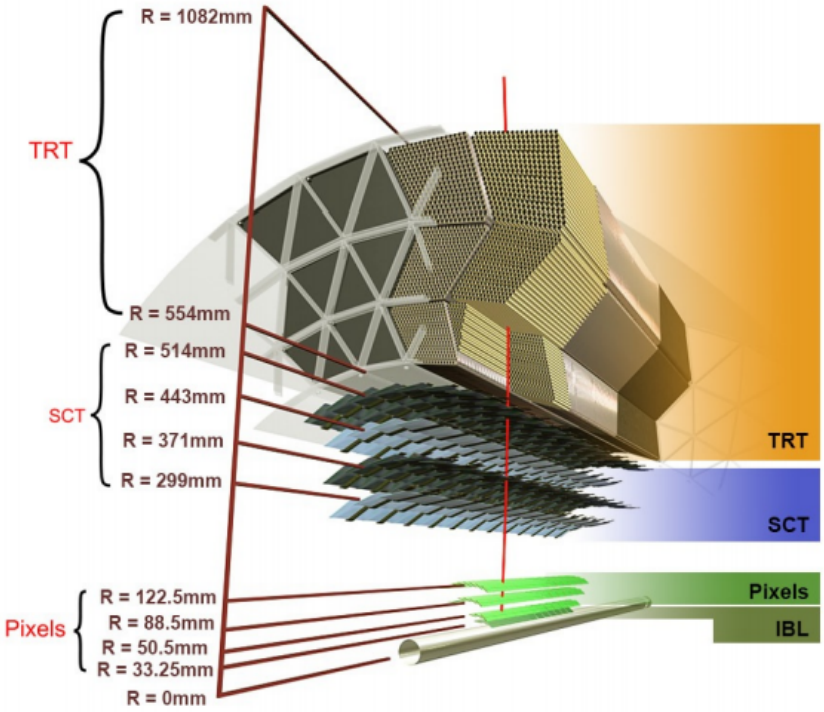

Figure 3.4: A schematic view of the ATLAS Inner detector

3.2.1.1 The Pixel Detector

The pixel detector is the innermost part of the ATLAS detector, designed to provide high-precision measurements per track as close to the IP as possible. It is vital to the determination of the impact parameter resolution and the identification of short-lived particles such as B hadrons and τ leptons. It is 1.4 m long and has a diameter of 0.43 m. During LHC Run 1, the active part of the pixel detector is made of three barrel layers (B-layer, layer 1, layer 2) at average radii of about 5 cm, 9 cm, and 12 cm, and three disks on each endcap regions between radii of 11 and 20 cm to guarantee at least three space points over the full tracking pseudorapidity range of $|\eta| < 2.5$. Spatial resolution of the pixel detector is about 12 μm/layer in the (R, ϕ) coordinate.

The active part of the pixel detector consists of a module composed of silicon sensors, front-end electronics and flex-hybrids with control circuits. There are 1744 modules with 80 million readout channels in total. The nominal pixel size is 50 microns in the ϕ direction and 400 microns in z (barrel region, along the beam axis) or r (disk region) with the exception that a few special pixels in the region between integrated circuits on a module have larger dimensions.

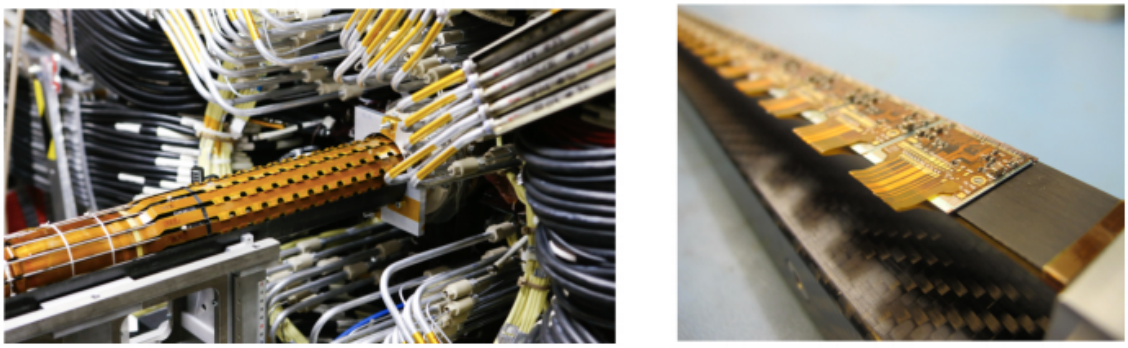

(a) (b)

Figure 3.5: The ATLAS IBL detector before the insertion (3.5a) and an IBL stave where the single detector modules are mounted on carbon fibre support structures (3.5b).

During the first long shutdown of the LHC in 2013-2014, a new innermost pixel detector, the Insertable B-layer (IBL) [53], was added between the first pixel layer and a new smaller radius beam pipe at the radius of 33 mm, to help improve the vertex resolution and b-tagging efficiency, to compensate for inefficiencies in the pixel B-layer which can arise over time due to irreversible radiation damage, as well as to meet the increasing bandwidth requirements resulting from the expected Phase-I LHC peak luminosity. Figure 3.5 shows the ATLAS IBL detector prior the insertion and an IBL stave. The spatial resolution of the IBL measured from collision data is 10.0 ± 0.1 μm in the transverse plane and 66.5 ± 0.8 μm in the longitudinal z direction.

3.2.1.2 The Semiconductor Tracker

The semiconductor tracker (SCT) is designed to provide eight precision measurements per track in the intermediate radial range, contributing to the measurement of momentum, impact parameter and vertex position, as well as providing good pattern recognition by the use of high granularity. The SCT tracker includes four barrel layers at average radii of about of 30.0, 37.3, 44.7 and 52.0 cm, and nine disks on each endcap regions to cover the full tracking pseudo-rapidity range of $|\eta| < 2.5$. The spatial resolution is about 16 μm in the transverse plane and 580 μm in longitudinal z direction. There are 61 m^2 of silicon detectors and 6.2 million readout channels in total in the SCT tracker.

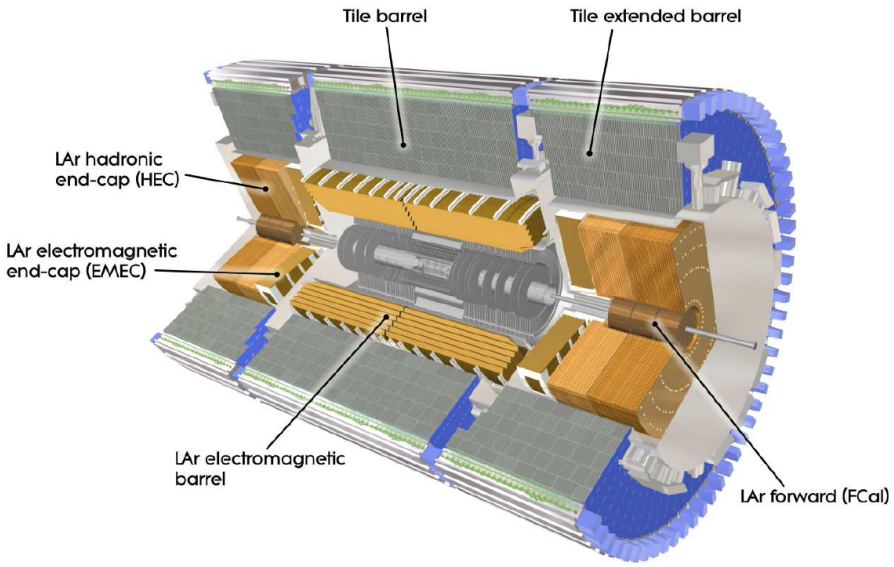

Figure 3.6: Cut-away view of the ATLAS Calorimeters.

3.2.1.3 Transition Radiation Tracker

The TRT, based on the use of straw detectors, is intrinsically radiation hard. It offers on average 30 two-dimensional space point measurements with an intrinsic resolution of approximately 120 μm for tracks with $p_{\mathrm{T}} > 0.5$ GeV and in the pseudorapidity range of $|\eta| < 2.0$. In addition to tracking, it also contributes to the electron identification capability enabled by the detection of transition-radiation photons created in a radiator between the straws.

3.2.2 Calorimeters

A view of the ATLAS calorimeters is shown in Figure 3.6. The calorimetry is built of an EM calorimeter covering the pseudorapidity range of $|\eta| < 1.475$ in the barrel region and $1.375 < |\eta| < 3.2$ in the endcap region, a hadronic calorimeter covering $|\eta| < 1.7$ in the barrel region and $1.5 < |\eta| < 3.2$ in the endcap region, and forward calorimeters covering $3.1 < |\eta| < 4.9$.

3.2.2.1 The Electromagnetic Calorimeter

The EM calorimeter is a lead/liquid-argon sampling calorimeter with an accordion geometry, providing complete ϕ symmetry without azimuthal cracks. Over the region of $|\eta| < 2.5$ ($2.5 < |\eta| < 3.2$ and in the overlap region between the barrel and the

endcap electromagnetic calorimeter) it is divided into three (two) layers in depth respectively, which are finely segmented in η and ϕ. An additional thin presampler layer covering the $|\eta| < 1.8$ region where the amount of material seen by an incident particle before the calorimeter front face is > 2 radiation lengths (X_0), is used to correct for fluctuations in energy losses of particles before they reach the calorimeter. The total thickness of the EM calorimeter increases from $22X_0$ to $30X_0$ in region from $\eta = 0$ to $\eta = 0.8$ and $24X_0$ to $33X_0$ in region from $\eta = 0.8$ to $\eta = 1.3$.

3.2.2.2 The Hadronic Calorimeters

The hadronic calorimeters includes the tile calorimeter, the liquid-argon hadronic endcap calorimeter (HEC) and the liquid-argon forward calorimeter (FCal).

The tile calorimeter is located in the barrel region. It is made of steel absorbers and scintillator tiles as the active medium. Its thickness is approximately 7.4 interaction lengths. Liquid argon with copper absorbers is used in the hadronic endcap calorimeters. The FCAL is located in the same cryostats as the endcap calorimeter. The FCAL is consist of copper in the first section and tungsten absorbers in the other two sectors, with liquid argon as the sensitive medium.

3.2.3 Muon Spectrometer

The muon spectrometer consists of the precision-tracking chambers to accurately and precisely measure the transverse momentum of the muons and the trigger chambers with fast reponse to trigger on the muons. The MS is immersed in a toroidal magnetic field of approximately 0.5 T and 1 T in the barrel and endcap regions, respectively. The MS is designed to be capable of standalone measurements of the transverse momentum of the muons in a wide range: down to about 3 GeV which is constrained by the muon energy loss in the calorimeters, and up to about 3 TeV. For 1 TeV muon tracks, the performance goal is to achieve approximately 10% stand-alone transverse momentum resolution, which corresponds to a sagitta along the z-axis of about 500 μm to be measured with a resolution of 50 μm or less. The cross-sections of the muon system in the planes transverse to and containing the beam axis are illustrated in Figure 3.7.

The precision-tracking chambers in the barrel region consists of three concentric cylindrical layers arranged around the beam axis at radii of approximately 5 m, 7.5 m, and 10 m. Precision Monitored Drift Tube (MDT) chambers cover the pseudorapidity range of $|\eta| < 2.7$, except that in the innermost endcap layer the region of $|\eta| < 2.0$

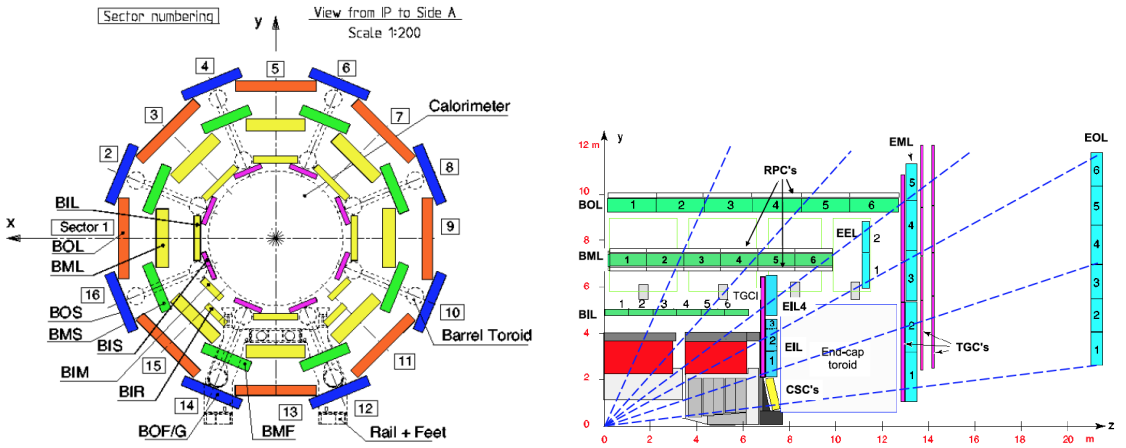

(a) (b)

Figure 3.7: Cross-section views of the muon spectrometer in the plan transverse to (3.7a) and along the beam axis (3.7b).

is covered. In the forward region of $2.0 < |\eta| < 2.7$ in the innermost endcap layer, the Cathode-Strip Chambers (CSC) which have higher rate capability are installed.

The trigger chambers include three concentric cylindrical stations of the Resistive Plate Chambers (RPC) in the barrel region covering $|\eta| < 1.05$ and the Thin Gap Chambers (TGC) in the endcap region covering $1.05 < |\eta| < 2.4$. The Level-1 trigger logic uses the fast information on the muon tracks provided by the trigger chambers to identify the track multiplicity and the approximate transverse momentum range.

Selected parameters characterize the performance of the muon sub-systems are summarized in Table 3.3. The following sections will briefly describe the technology and performances of the muon sub-systems.

Detector	Chamber Resolution (RMS)			Number of	
Type	z/R	ϕ	time	chambers	channels
MDT	35 μm	-	-	1088(1150)	339k (354k)
CSC	40 μm	5 mm	7 ns	32	30.7k
RPC	10 mm	10 mm	1.5 ns	544(606)	359k(373k)
TGC	2-6 mm	3-7 mm	4 ns	3588	318k

Table 3.3: Parameters of the sub-systems of the MS. The quoted spatial resolution (columns 2, 3) does not include chamber-alignment uncertainties. Column 4 shows the intrinsic time resolution of each chamber type. Numbers in brackets refer to the complete detector configuration as planned for 2009.

3.2.3.1 Monitored Drift-tube Chambers

The MDT chambers are made of drift tubes with a diameter of 30 mm. The wall of the tube is made using aluminium and is 400 μm in thickness. A tungsten-rhenium wire of 50 μm in diameter is located at the center of the tube. The tubes are operated with a non-flammable mixture of 93% Ar and 7% CO_2 at an absolute pressure of 3 bar. A muon passing the tube is ionized in the drift field. The electrons from the ionization drift towards the wire with a maximum drift time of 700 ns when drifting from the wall to the wire. The position of the muon thus can be determined through the tube's non-linear space and time relation. The spatial resolution of a MDT tube is about 80 μm.

3.2.3.2 Cathode Strip Chambers

The CSCs are multiwire proportional chambers with the wires oriented in the radial direction. Both cathodes are segmented, one with the strips perpendicular to the wires (providing the precision coordinate) and the other parallel to the wires providing the transverse coordinate. The position of the track is obtained by interpolation between the charges induced on neighboring cathode strips while wire signals are not read out. The resolution of a CSC plane is about 60 μm, while in the non-bending direction, the cathode segmentation is coarser leading to a resolution of 5 mm.

3.2.3.3 Resistive Plate Chambers

In the barrel, RPCs are used to build trigger chambers because of good spatial and time resolution, and adequate rate capability. The RPC is a gaseous parallel electrode-plate detector, operated with a mixture of C2H2F4/Iso-C4H10/SF6 (94.7/5/0.3), which combines the merits of relatively low operating voltage, non-flammability and low cost, while providing a comfortable plateau for safe avalanche operation. It contains two resistive plates made of phenolic-melaminic plastic laminate. They are kept parallel to each other at a distance of 2 mm by insulating spacers, and the electric field between them is about 4.9 kV/mm, allowing avalanches to form along the ionizing tracks towards the anode. The signal is read out via capacitive coupling to metallic strips, which are mounted on the outer faces of the resistive plates.

3.2.3.4 Thin Gap Chambers

In the endcap region, TGCs have been selected to build the trigger chambers due to good time resolution and high rate capability. In addition to trigger capability,

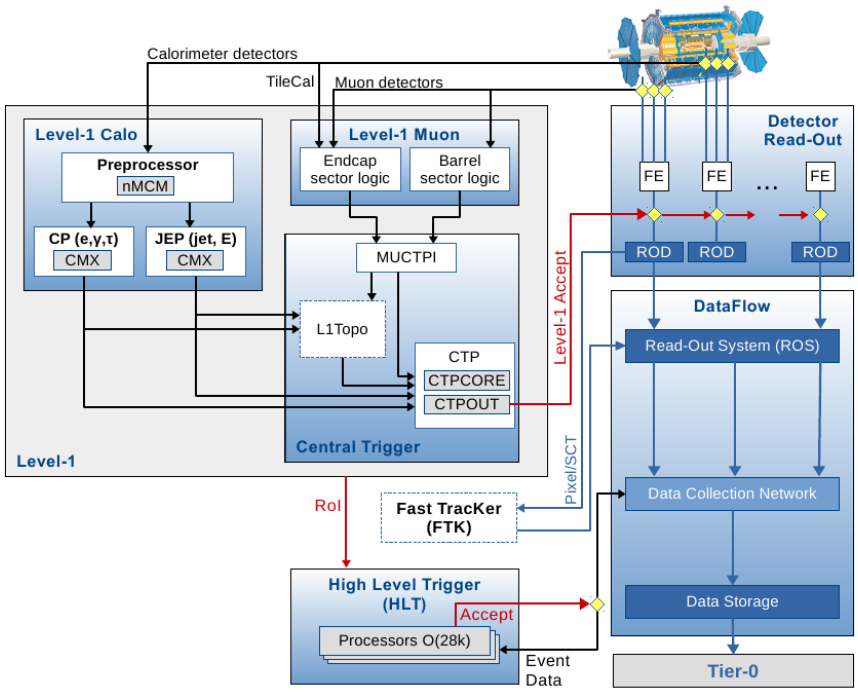

Figure 3.8: The ATLAS TDAQ system in Run 2 with emphasis on the components relevant for triggering. L1Topo and FTK were being commissioned during 2015.

TGCs provide a second azimuthal coordinate to complement the measurement of the MDTs in the bending (radial) direction. TGCs are multi-wire proportional chambers operated in a highly quenching gas mixture of CO2 and n-C5H12 (n-pentane), with the characteristic that the wire-to-cathode distance of 1.4 mm is smaller than the wire-to-wire distance of 1.8 mm. This cell geometry allows for operation in a quasi-saturated mode, i.e. with a gas gain of 3×10^5.

3.2.4 Trigger

The trigger system is an essential component of hadron collider experiments, because the rate of events containing interesting physics phenomena is only a small fraction of the total event rate. Due to the constraint from data storage capacity and rates, it is impossible to store all the events produced in the collisions, therefore, trigger system is employed to rapidly decide with high efficiency potential interesting events produced in a given bunch-crossing interaction to record for later analysis.

The ATLAS Trigger and Data Acquisition (TDAQ) system is illustrated in the block diagram shown in Figure 3.8 [54]. In Run 2, the trigger system consists of two levels of event selections: a Level-1 trigger (L1) reducing event rate to 100 kHz and

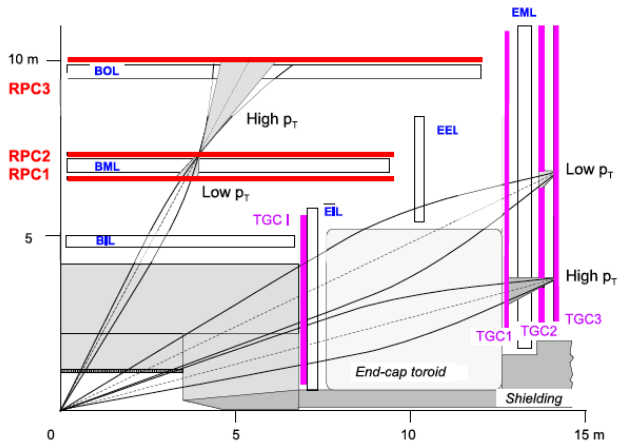

Figure 3.9: A schematic view of the muon trigger system. RPC2 and TGC3 are the reference planes in the barrel and endcap regions, respectively.

a high-level trigger (HLT) further reducing event rate to 1 kHz. In LHC Run 1, the HLT includes two levels of event selections: Level-2 and Event Filter farms, which were merged into a single homogeneous farm in Run 2 to improve resource sharing and for simplification.

3.2.4.1 Level-1 Trigger

The L1 is a hardware based trigger using reduced-granularity information from a subset of detectors. The Muon trigger (L1Mu) uses trigger chambers to identify signatures consistent with high-p_{T} muons and the Calorimeter trigger (L1Calo) uses all the calorimeter sub-systems to identify high-E_{T} electrons and photons, jets, τ-leptons decaying into hadrons, large $E_{\mathrm{T}}^{\mathrm{miss}}$ and large total transverse energy. The L1 identifies Regions-of-Interests (ROIs), which are the regions of the detector where possible trigger object in the event exist, and passes ROIs information to HLT.

- Muon trigger. The L1 muon trigger works with dedicated trigger chambers, the RPCs and the TGCs, which have been introduced in Section 3.2.3. Both of them have three trigger stations to allow the trigger algorithm to require a coincidence of hits in the different trigger stations within a road as illustrated in Figure 3.9, which tracks the path of a muon from the interaction point to the hits in the reference plane which is the middle RPC (RPC2) and outer TGC (TGC3) for the barrel and endcap regions, respectively. The width of the road decreases with the threshold to be applied to the p_{T} of the muon. There are six thresholds in total, three associated with the low-p_{T} trigger and three with

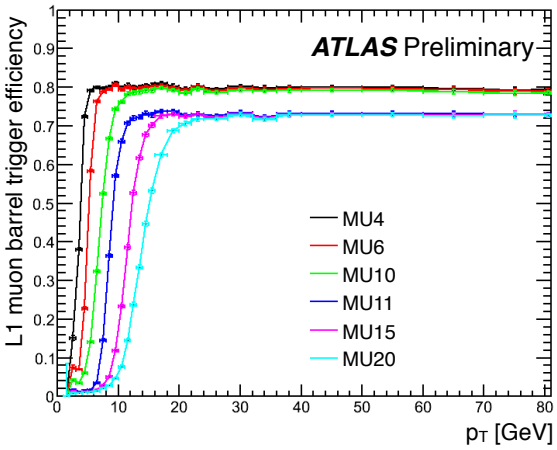

Figure 3.10: Efficiencies as functions of p_{T} of the six L1 muon triggers used in Run 1 in the barrel region: low-p_{T} threshold triggers MU4, MU6, MU10 with p_{T} threshold of 4, 6 and 10 GeV, respectively, and high-p_{T} threshold triggers MU11, MU15, MU20 with p_{T} threshold of 11, 15 and 20 GeV, respectively.

the high-p_{T} trigger. The efficiencies as functions of p_{T} of the six triggers in the barrel region used in Run 1 are shown in Figure 3.10. RPCs and TGCs also have sufficient timing accuracy to be able to identify the bunch-crossings.

During Run 1, the L1 trigger rate from the endcap region was dominated by particles not originating from the interaction point. To suppress such background events being accepted by L1 trigger, an new trigger logic [55] was introduced in Run 2 as illustrated in Figure 3.11, which requires an additional coincidence with the TGC-FI and TGC-EI chambers in the $1.3 < |\eta| < 1.9$ and the $1.05 < |\eta| < 1.3$ regions, respectively. It successfully lowered the trigger rate with very small loss on the efficiency.

- Calorimeter trigger

  L1Calo works with 7000 analogue trigger towers with granularity of 0.1×0.1 in $\Delta\eta \times \Delta\phi$ in most regions, and larger at higher $|\eta|$ region in the calorimeters. As shown in Figure 3.12, the electron/photon trigger algorithm is based on 4×4 trigger towers. 2×2 trigger towers are identified, in which at least one of the four possible two-tower sums of nearest-neighbor electromagnetic towers exceeds a pre-defined threshold. Isolation-veto thresholds are set for the surrounding ring in the electromagnetic calorimeter, as well as for the 2×2 hadronic-tower core sum behind the cluster and the hadronic ring around the hadronic-tower core. The τ algorithm uses the same basic elements to select narrow hadronic jets.

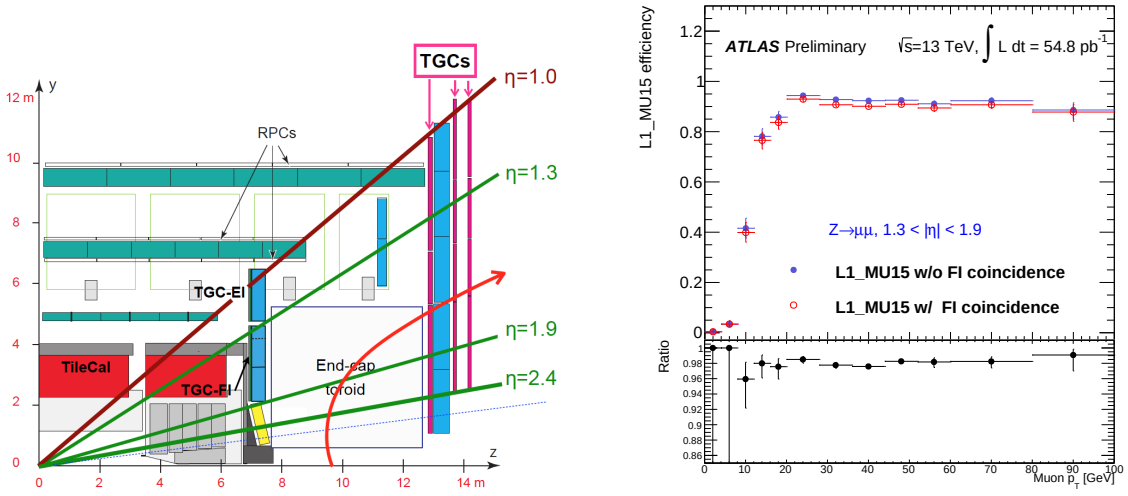

(a) (b)

Figure 3.11: In Figure 3.11a, the curved red arrow illustrates a L1 muon trigger due to background particles generated at the beam pipe around $z = 10$ m. Triggers due to events of this type are mitigated by requiring an additional coincidence with the TGC-FI or TGC-EI chambers. Figure 3.11b shows the efficiencies of L1_MU15 endcap trigger as a function of the p_{T} of offline muons without (blue points) and with (red points) the additional coincidence with TGC-FI chamber enabled, and their ratio (black points).

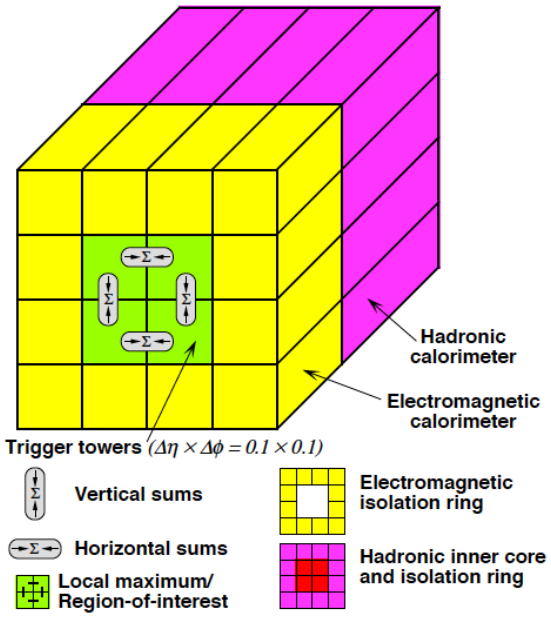

Figure 3.12: Electron/photon and τ trigger algorithms.

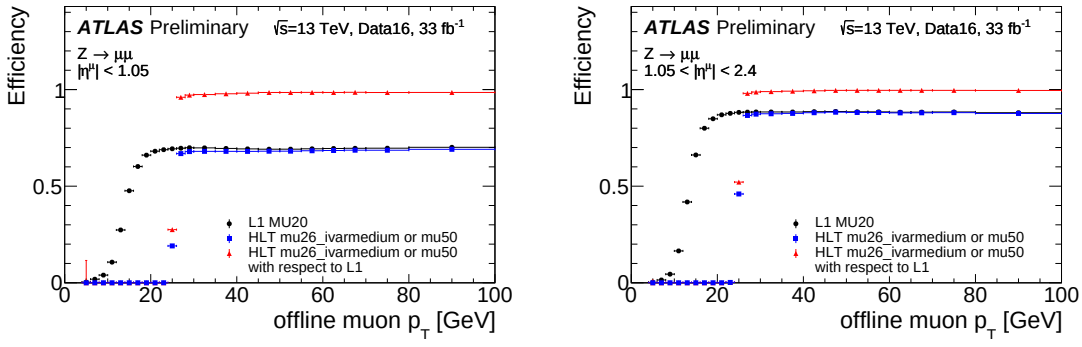

(a) (b)

Figure 3.13: The absolute efficiency of L1 MU20 trigger and absolute and relative efficiencies compared to the L1 MU20 trigger of the OR of mu26_ivarmedium and mu50 HLT as a function of p_{T} of offline muon candidates in the barrel (3.13a) and endcap (3.13b) detector regions.

The Jet/Energy trigger algorithm works with jet elements formed by the sums of 2×2 trigger towers in the electromagnetic calorimeters and in the hadronic calorimeters. $E_{\mathrm{T}}$are summed within overlapping windows consisting of 2×2, 3×3, or 4×4 jet elements and these sums are then compared to pre-defined jet energy thresholds.

3.2.4.2 High-Level Trigger

Seeded by ROIs, the HLT algorithms is performed on fully-built events based on the full granularity and precision of calorimeter and muon detector data, and inner detector data, to further select events. In Run 2, the HLT algorithms are designed to adopt offline tools in terms of data preparation, detector software, event reconstruction and selection cuts in analysis, to increase signal acceptance and higher background rejection in the offline analysis. As an example, Figure 3.13 plots the absolute efficiency of L1 MU20 trigger and absolute and relative efficiencies compared to the L1 MU20 trigger of the OR of mu26_ivarmedium and mu50 HLT as a function of p_{T} of offline muon candidates in the endcap and barrel detector regions. The MU20 trigger requires that a muon candidate passed the 20 GeV requirement of the L1 muon trigger system. The mu26_ivarmedium trigger is seeded by the MU20 trigger and is required to satisfy a 26 GeV HLT threshold and to pass a medium isolation selection computed using inner detector tracks reconstructed online by the HLT within a cone with a variable size which depends on the p_{T} of the muon. The

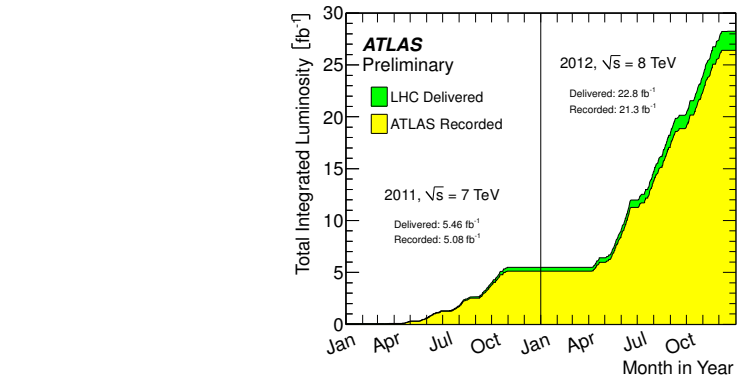

(a)

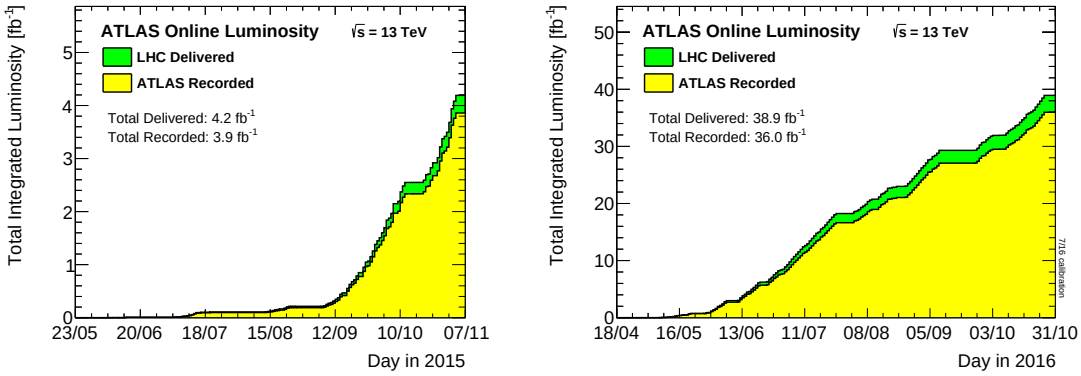

(b) (c)

Figure 3.14: Total integrated luminosity delivered by the LHC shown in green histogram and recorded by the ATLAS detector in 2011-2012 (3.14a), 2015 (3.14b) and 2016 (3.14c)

mu50 trigger is seeded by MU20 at L1 and is required to have p_{T} bigger than 50 GeV. The average data recording rate of 1 kHz is achieved in Run 2 increased from 400 Hz in Run 1. The events passing HLT trigger are recorded for subsequent offline analysis.

3.2.5 Data Collection

During the LHC Run-1 in 2011 and 2012 and Run-2 in 2015 and 2016, the operation of ATLAS detector ensures a high data taking efficiency of about 93%. Figure 3.14 shows the integrated luminosity delivered by the LHC and recorded by the ATLAS detector versus time in 2011 and 2012 with preliminary luminosity calibration, and in 2015 and 2016 with the initial online calibration.

The data collected by the ATLAS detector need to pass quality requirements

before being used in an analysis. If any relevant detector component is not operating correctly during the period in which an event is recorded, this event thus fails quality requirements. Dedicated measurements are performed to determine the luminosity in pp collisions using the ATLAS detector [56, 57]. The measured integrated luminosities and the associated uncertainties of the datasets used in the analyses presented in this dissertation, are summarized in Table 3.4.

	2011	2012	2015 + 2016
Integrated luminosity (fb^{-1})	4.5	20.3	36.1
Luminosity uncertainty ($\delta L/L$)	$\pm 1.8\%$	$\pm 2.8\%$	$\pm 3.2\%$
Analysis	2011 data	2012 data	2015 + 2016 data
Spin and parity in $H \to ZZ^* \to 4\ell$	Yes	Yes	Yes
Spin and parity combining ZZ^*, $\gamma\gamma$, WW^*	Yes	Yes	No
Higgs boson coupling measurement in $H \to ZZ^* \to 4\ell$	No	No	Yes
Higgs boson production and decay combining ZZ^*, $\gamma\gamma$	No	No	Yes (14.8 fb^{-1}(ZZ^*), 13.3 fb^{-1}($\gamma\gamma$))

Table 3.4: Summary of Higgs property measurements presented in this dissertation and data sets used in analyses with corresponding integrated luminosities including the luminosity uncertainties.

CHAPTER IV

ATLAS Event Reconstruction

Each time protons collide creating particles in final state is called an "event". In the ATLAS detector, there will be about a billion collision events per second. We record all the events that pass our "trigger system". Each recorded event will be reconstructed as physics objects, which will be described in this chapter.

4.1 Tracking

The reconstructed charged-particle trajectories in the inner detector and muon spectrometers are hereafter referred to as tracks.

4.1.1 Tracking in Inner Detector

The tracks in the inner detector is based on fitting a trajectory model to a set of measurements using a sequence of algorithms [58]. The inside-out algorithm starts from three-point seeds in the silicon detectors and adds hits moving away from the interaction point using a combinatorial Kalman filter. Ambiguities in the track candidates found in the silicon detectors are resolved, and tracks are extended into the TRT. The inside-out algorithm is the baseline algorithm designed for efficient reconstruction of primary charged particles. Primary particles are defined as particles with a mean lifetime of greater than 3×10^{11} s directly produced in a pp interaction or from the subsequent decays or interactions of particles with a lifetime shorter than 3×10^{11} s. The tracks reconstructed by the inside-out algorithm are required to have transverse momentum $p_{\mathrm{T}} > 400$ MeV.

In a second stage, a track search starts from segments reconstructed in the TRT and extends inwards by adding silicon hits, which is referred to as back-tracking.

Back-tracking is designed to reconstruct secondary particles, which are particles produced in the interactions of the primary particles. Finally tracks with a TRT segment but no extension into the silicon detectors are referred to as TRT-standalone tracks.

The transverse and longitudinal impact parameters of a track relative to the center of the beam spot are are referred to as d_0 and z_0 and their resolutions as σ_{d_0} and σ_{z_0}.

4.1.2 Tracking in Muon Spectrometer

The tracks in the MS starts from segments reconstructed within each muon chamber [59]. In each MDT chamber and nearby trigger chamber, a Hough transform is used to search for hits. Segments are reconstructed by performing a straight-line fit to the hits found in each MDT layer. The RPC or TGC hits measure the coordinate orthogonal to the bending plane. Segments in the CSC detectors are reconstructed by a combinatorial search for hits in the η and ϕ CSC planes, including a loose requirement on the compatibility of the segment with the luminous region.

Muon track candidates are then built by fitting together hits from segments in different layers. The algorithm used for this task performs a segment-seeded combinatorial search that starts by using as seeds the segments generated in the middle layers of the detector where more trigger hits are available. The search is then extended to use the segments from the outer and inner layers as seeds. The segments are selected using criteria based on hit multiplicity and fit quality and are matched using their relative positions and angles. At least two matching segments are required to build a track, except in the barrel endcap transition region where a single high-quality segment with η and ϕ information can be used to build a track. The same segment can initially be used to build several track candidates. Later, an overlap removal algorithm selects the best assignment to a single track, or allows for the segment to be shared between two tracks. To ensure high efficiency for close-by muons, all tracks with segments in three different layers of the spectrometer are kept when they are identical in two out of three layers but share no hits in the outermost layer.

The hits associated with each track candidate are fitted using a χ^2 fit. A track candidate is accepted if the χ^2 of the fit satisfies the criteria. The track candidate will be re-fitted in cases where hits making large contributions to the χ^2 are removed or additional hits consistent with the track candidate are recovered.

4.2 Primary Vertex

This section describes the method for reconstructing primary vertices. The input to the vertex reconstruction is a collection of reconstructed tracks. The procedure of primary vertex reconstruction is divided into two stages: vertex finding and vertex fitting [60]. The former stage generally denotes the pattern recognition process: the association of reconstructed tracks to vertex candidates. The vertex fitting stage includes the reconstruction of the actual vertex position and its covariance matrix. The strategy can be briefly outlined in these steps:

- A set of tracks satisfying the track selection criteria is defined.
- A seed position for the first vertex is selected.
- The tracks and the seed are used to estimate the best vertex position with a fit following an iterative procedure. In each iteration, less compatible tracks are down-weighted and the vertex position is recomputed.
- Tracks incompatible with the vertex determined in the previous step are removed and allowed to be used in the determination of another vertex.
- The whole procedure is repeated with the remaining tracks in the event to fit another vertex.

All vertices with at least two associated tracks are retained as valid primary vertex candidates. The output of the vertex reconstruction algorithm is a set of three dimensional vertex positions and their covariance matrices.

In $H \to ZZ^* \to 4\ell$ analysis, events are required to have at least one vertex with two associated tracks with $p_{\mathrm{T}} > 400$ Mev, and the primary vertex is chosen to be the reconstructed vertex with the largest $\sum p_{\mathrm{T}}^2$. Four leptons selected must come from the primary vertex.

4.3 Electron

4.3.1 Electron Reconstruction

Electrons in ATLAS are reconstructed based on information from the ID and the electromagnetic calorimeter. Electron candidates are clusters of energy associated with ID tracks, where the final track-cluster matching is performed after the tracks have been fitted with a Gaussian-sum filter. The energy of the electron is given by

the cluster energy while the ϕ and η directions are provided by the track parameters with respect to the beam line.

4.3.2 Electron Identification

Electrons are identified based on several variables to suppress background objects such as hadronic jets or converted photons [61]. These variables are the hits in the silicon detectors, including a hit in the innermost layer of the detector, the IBL (or the next-to-innermost layer in case of masked modules), and a likelihood discriminator, which combines the shower shape information provided by the highly segmented calorimeter, hits in the high-threshold TRT, compatibility of the tracking and calorimeter information, as well as some of the track quality information. In Run 2, two additional variables, the impact parameter in the transverse plane ($|d_0|$) and its significance ($|d_0|/\sigma_{d_0}$) have been added to the likelihood discriminator, further rejecting heavy-flavor background contributions.

To meet the needs of different physics analyses, different requirements on the output score of the likelihood discriminator are defined to offer three identification criteria: loose, medium and tight. The identification efficiencies for electrons and backgrounds are in a range of 78% - 90% and 0.3% - 0.8%, respectively [62].

4.3.3 Electron Isolation

Electrons produced from the decay of heavy particles, such as W, Z, or Higgs boson, are often well separated from other particles in the event. Therefore, electron isolation, which measures the detector activity around an electron candidate, can be used to further reject backgrounds such as electrons originating from converted photons produced in hadron decays, electrons from heavy flavor hadron decays, and light hadrons misidentified as electrons. Two isolation variables are defined:

- track-based isolation variable: $p_{\mathrm{T}}^{varcone20}$, is defined as the scalar sum of the p_{T} of the tracks satisfying quality requirements and originating from the primary vertex with $E_{\mathrm{T}} > 1$ GeV in a cone of size $\Delta R = min(10\ \mathrm{GeV}/E_{\mathrm{T}}^{e}, 0.2)$ centered around the direction of electron track. The electron track itself is excluded.

- calorimeter-based isolation variable, $E_{\mathrm{T}}^{topocone20}$, is defined as the sum of the E_{T} of clusters topologically connected [63] in a cone of size $\Delta R = 0.2$ around the electron, after subtracting the contribution from the energy deposit of the electron itself and correcting for effects from pile-up and underlying events.

Several electron isolation selection criteria are defined based on relative isolation variables, $p_{\mathrm{T}}^{varcone20}/p_{\mathrm{T}}$ and $E_{\mathrm{T}}^{topocone20}/E_{\mathrm{T}}$, to address the needs from various physics analysis.

4.4 Muon

4.4.1 Muon Reconstruction

Muon reconstruction is performed based on information from the ID, MS and calorimeters. There are four types depending on different reconstruction methods and subdetectors used [59].

- Combined (CB) muons. CB muons are reconstructed by combining the hits of the ID track and MS track and the energy loss in the calorimeter;
- Segment-tagged (ST) muons. A track in the ID is classified as a muon if it is associated with at least one track segment in the MDT or CSC chambers. MS muons captures muons transversing only one layer of MS chambers, due to their low p_{T} or reduced MS acceptance in the region;
- Standalone (SA) muons. In the $2.5 < |\eta| < 2.7$ region, where the ID provides little coverage, the muon is reconstructed based on the track reconstructed in the MS and a loose requirement on its compatibility with originating from the IP, taking into account the energy loss in the calorimeter;
- Silicon-associated forward (SiAF) muons: In the $2.5 < |\eta| < 2.7$ region, when a track reconstructed in the MS is extrapolated back to the interaction point, a very forward ID tracklet formed by Silicon hits only (no TRT hits) is found within a cone around the track in the MS, a combined fit is performed including the hits of the ID tracklet. This type of muon is used in the 2 $H \to ZZ^* \to 4\ell$ analysis in Run 2 using the dataset collected at $\sqrt{s} = 13$ TeV.
- Calorimeter-tagged (CT) muons. In the region of $|\eta| < 0.1$, ID tracks with 15 GeV $< p_{\mathrm{T}} <$ 100 GeV are identified as muons if their energy deposits in the calorimeter are consistent with minimum ionizing particles. CT muons recover muon acceptance in the region where the MS is only partially instrumented to allow for cabling and services to the calorimeters and the ID.

4.4.2 Muon Identification

Muon identification is carried out by applying quality requirements to suppress background, while maintain high efficiencies and robust momentum measurements for prompt muons. The quality variables used in the muon identification are summarized below. The first two variables quantify the compatibility between the ID and MS p_{T} measurements.

- q/p significance, defined as:

$$q/p = \frac{|q/p_{\mathrm{T,ID}} - q/p_{\mathrm{T,MS}}|}{\sqrt{\sigma^2_{p_{\mathrm{T,ID}}} + \sigma^2_{p_{\mathrm{T,MS}}}}} \tag{4.1}$$

  is the absolute value of the difference between the ratio of the charge and transverse momentum of the muons measured in the ID ($p_{\mathrm{T,ID}}$) and in the MS ($p_{\mathrm{T,MS}}$), divided by the sum in quadrature of the corresponding uncertainties;

- ρ', defined as

$$\rho' = \frac{p_{\mathrm{T,ID}} - p_{\mathrm{T,MS}}}{p_{\mathrm{T,CB}}} \tag{4.2}$$

  is the absolute value of the difference between the transverse momentum measured in the ID ($p_{\mathrm{T,ID}}$) and in the MS ($p_{\mathrm{T,MS}}$), divided by the transverse momentum of the combined track ($p_{\mathrm{T,CB}}$);

- normalized χ^2 of the combined track fit;

- number hits in the ID and the MS.

There are four kinds of muon identification criteria designed (Medium, Loose, Tight, and High-p_{T}) designed to address the specific needs of physics analyses.

- Medium muons, are designed to minimize the systematic uncertainties associated with muon reconstruction and calibration. Only CB and ME muons are considered, with addition requirement on the number of hits in muon chambers and a loose requirement on the compatibility between p_{T} measurements in the ID and MS (q/p significance < 7);

- Loose muons, designed to maximize the reconstruction efficiency while provide good-quality muon tracks, are specifically optimized for reconstructing Higgs boson candidates in the four-lepton final states. All medium muons defined above, and CT and ST muons in the $|\eta| < 0.1$ region are included;

- Tight muons, are selected to maximize the purity of muons at the cost of some efficiency. Only CB muons with at least two hits in MS and satisfying the medium criteria are considered. Additionally, requirements on normalized χ^2 of the track fit and the compatibility between ID and MS p_{T} measurements is employed to further reject background;

- High-p_{T} muons, are optimized for searches for high-mass Z' and W' resonances. To maximize the momentum resolution for muons with $p_{\mathrm{T}} > 100$ GeV, CB muons satisfying medium requirements and having at least three hits in three MS stations are included. Regions of the MS are vetoed, where the alignment is suboptimal.

4.4.3 Muon Isolation

Muon isolation, similarly as the electron isolation, is very powerful in discriminating prompt muons from backgrounds. Muon isolation selection criteria are defined using relative isolation variables, $p_{\mathrm{T}}^{varcone30}/p_{\mathrm{T}}$ and $E_{\mathrm{T}}^{topocone20}/E_{\mathrm{T}}$, where the isolation variables are defined similarly as the electron, with the cone size changed to $\Delta R = min(10\ \mathrm{GeV}/p_{\mathrm{T}}^{\mu}, 0.3)$ for the track-based isolation variable.

4.5 Jet

Jets are reconstructed from clusters of calorimeter cells using the anti-k_t algorithm with a distance parameter $R = 0.4$ [64]. The algorithm for the clustering suppresses noise and pileup by keeping only cells with a significant energy deposit and their neighboring cells. The jets are calibrated using a dedicated scheme designed to adjust, on average, the energy measured in the calorimeter to that of the true jet energy. To reduce the number of jet candidates originated from pileup vertices, jets with $p_{\mathrm{T}} < 60$ GeV within the ID acceptance ($|\eta| < 2.4$) have requirements applied to the fraction of tracks which come from the primary vertex.

4.5.1 B-Jet Tagging

The identification of jets containing b-hadron decays (b-tagging) is very important to physics analyses involved with the bottom or top quark. A typical b-hadron topology as illustrated in Figure 4.1 [65] is the presence of a vertex displaced from the primary vertex because of the long lifetime of hadrons containing a b-quark (life

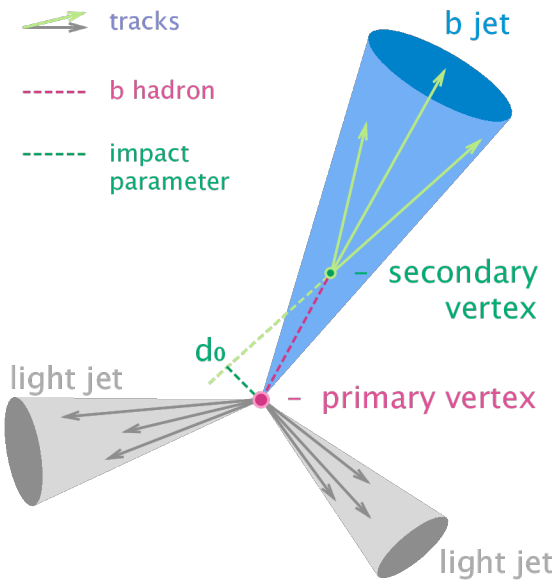

Figure 4.1: Common principles of b-tagging.

time $\tau \approx 1.5$ ps, $c\tau \approx 450$ μm). Based on such features, Boosted Decision Tree multivariate discriminants (MV2 algorithm) is used for b-tagging [66].

CHAPTER V

$H \to ZZ^* \to 4\ell$ Event Selection

The Higgs boson decay to four leptons channel, $H \to ZZ^* \to 4\ell$, where $\ell = e$ or μ, provides good sensitivity for the measurement of Higgs boson properties due to its high signal-to-background ratio (S/B), fully reconstructed final states and good signal mass resolution ($1 - 2\% \times m_H$, $m_H = 125$ GeV). The signal-to-background ratio is about $2.2 - 2.3$ for all of the four final states: $\mu^+\mu^-\mu^+\mu^-$ (4μ), $e^+e^-\mu^+\mu^-$ ($2e2\mu$), $\mu^+\mu^-e^+e^-$ ($2\mu2e$), and $e^+e^-e^+e^-$ ($4e$), in the analysis using data collected at 13 TeV. The first lepton pair is defined as the one with the invariant mass closest to the Z boson mass. The largest background source for this channel, throughout the four-lepton invariant mass ($m_{4\ell}$) range, is from the continuum $(Z^{(*)}/\gamma^*)(Z^{(*)}/\gamma^*)$ production, referred to as continuum ZZ^* background hereafter. For events with four-lepton invariant mass below about 160 GeV, there are also smaller background contributions from Z boson production in association with jets (Z + jets) and top quark pair ($t\bar{t}$) production with two prompt leptons, where the additional charged lepton candidates arise from decays of hadrons with b- or c-quark content, from π/K in flight decays, from photon conversions or from misidentification of jets.

5.1 Trigger

In Run-1, four-lepton events were selected with single-lepton and dilepton triggers. The p_{T} (E_{T}) thresholds for single-muon (single-electron) triggers increased from 18 GeV to 24 GeV (20 GeV to 24 GeV) between the 7 TeV and 8 TeV data, in order to cope with the increasing instantaneous luminosity. The dilepton trigger thresholds for 7 TeV data are set at 10 GeV p_{T} for muons, 12 GeV E_{T} for electrons and (6,10) GeV for (muon, electron) mixed-flavor pairs. For the 8 TeV data, the thresholds were raised to 13 GeV for the dimuon trigger, to 12 GeV for the dielectron trigger and (8,12) GeV for the (muon, electron) trigger; furthermore, a dimuon trigger with

different thresholds on the muon p_{T} 8 and 18 GeV, was added. The trigger efficiency for events passing the final selection is above 97% in the 4μ, $2\mu 2e$ and $2e2\mu$ channels and close to 100% in the $4e$ channel for both 7 TeV and 8 TeV data.

In Run-2, single-lepton, dilepton and trilepton triggers are used to select events. The electron trigger applies loose and medium likelihood identification for multilepton triggers or medium and tight for single-electron trigger, and applies isolation requirements only in the single-muon triggers. For the 2016 data the p_{T} thresholds have been raised and the electron identification tightened with the increase of the peak luminosity during the run. The impact on the signal efficiency is rather small, below 1%. Globally, the trigger efficiency for signal events passing the final selection is about 98%.

5.2 Object Selection

Because this channel has a very small Higgs boson decay branching ratio, it is vital to improve the signal efficiently whenever possible. Thus, the electrons and muons are selected by loose identification criteria to ensure high efficiencies while suppress background. The electrons are required to satisfy $E_{\mathrm{T}} > 7$ GeV, and $|\eta| < 2.47$, while the p_{T} threshold for muons has lowered to 5 GeV from 6 GeV from Run 1 to Run 2, improving the signal efficiency by 7% in the 4μ channel. The increased background due to the lower p_{T} threshold is mitigated by a requirement on the χ^2 value of a fit of the four-lepton tracks to a common vertex, which will be discussed later in this section.

The jets selected are reconstructed using anti-k_t algorithm with a distance parameter $R = 0.4$, and satisfy $p_{\mathrm{T}} > 30$ GeV and $|\eta| < 4.5$. The jet p_{T} threshold increased from 25 GeV to 30 GeV in the forward region of $2.7 < |\eta| < 4.5$ from Run 1 to Run 2, in light of higher pile-up effects due to increased luminosity in Run 2. This increase in jet p_{T} threshold improves VBF signal significance by a few percent. Pile-up rejection requirements are placed on the jets having $p_{\mathrm{T}} < 60$ GeV and $|\eta| < 2.4$, further reject pile-up jets. The b-jets identified by the MV2 algorithm with 70% efficiency are selected requiring $p_{\mathrm{T}} > 30$ GeV and $|\eta| < 2.5$.

Since different physics object can be reconstructed from the same detector information, the next step is to resolve the overlap ambiguity. If an electron and a muon which share the same ID track, the muon is selected except that if the muon is a calorimeter-tagged muon, the electron is selected. The jets close to electrons are removed if their angular separation satisfies $\Delta R < 0.2$, while the jets close to muons

are removed if their angular separation satisfies $\Delta R < 0.1$, the muon has less than three tracks and energy energy and momentum differences between the muon and the jet are small.

5.3 Four-Lepton Selecton

Lepton quadruplets are formed by all possible senarios of two pairs of same-flavor, opposite-sign lepton in an event. The lepton pair with invariant mass closer to the Z boson mass is referred to as the leading lepton pair and the other one as the subleading lepton pair. The invariant mass of the leading and subleading lepton pairs are denoted as m_{12} and m_{34}. For each of the Higgs boson candidate, the p_{T} of the leading three leptons in order of increasing p_{T} is required to be larger than 20, 15 and 10 GeV, respectively.

Next step is to look for Higgs boson candidate for each of the four sub-channels: 4μ, $2e2\mu$, $2\mu2e$, $4e$. The following procedure is performed in parallel in each sub-channel. The quadruplet with m_{12} closest to the Z boson mass are chosen as the Higgs boson candidate. In case there are more than one such quadruplet, the quadruplet with m_{34} closest to the Z boson mass is selected.

Further selections are made to the Higgs boson candiate. Considering in most of the SM Higgs boson decaying to two Z bosons events, the two Z bosons are produced with one on-shell and the other one off-shell, and only a tiny fraction of the events are produced with both Z boson off-shell, m_{12} is then required to be between 50 GeV and 106 GeV, and m_{34} is required to be in the range $m_{min} < m_{34} < 115$ GeV, where m_{min} is 12 GeV for $m_{4l} < 140$ GeV, and rises linearly to 50 GeV at $m_{4l} = 190$ GeV and then remains at 50 GeV for $m_{4l} > 190$ GeV. Additional, the leptons are required to be well separated with each other at an angular distance of $\Delta R > 0.1$ if the two leptons are of the same flavor and $\Delta R > 0.2$ otherwise. For 4μ and $4e$ events, if an opposite-charge same-flavor lepton pair is found to have an invariant mass below 5 GeV, this event is removed to reject background contribution from the process J/ψ decaying to a pair of leptons.

The Z+jets and $t\bar{t}$ background contributions are suppressed by applying track and calorimeter-based isolation requirements as well as impact parameter requirements to the leptons. For muons, the requirements are relative track isolation variable $p_T^{varcone30}/p_{\mathrm{T}} < 0.15$ and relative calorimeter isolation variable $E_T^{topocone20}/E_{\mathrm{T}} < 0.30$. For electrons, the requirements are relative track isolation variable $p_T^{varcone20}/p_{\mathrm{T}} < 0.15$ and relative calorimeter isolation variable $E_T^{topocone20}/E_{\mathrm{T}} < 0.20$. The transverse

impact parameter significance, defined as the impact parameter in the transverse plane divided by its uncertainty, $|d_0|/\sigma_{d_0}$, for all muons (electrons) is required to be lower than 3 (5).

In order to cope with the increase of the reducible background due to the lowering of the minimum muon p_{T} requirement (lowered from 6 GeV to 5 GeV), the four leptons are required to be compatible with the same vertex. A loose χ^2 selection is applied, corresponding to a signal efficiency of 99.5% for all decay channels, which further reduces 15% of the $Z+$jets and $t\bar{t}$ background.

Next, if more than one channel has a quadruplet passing the selection, the channel with the highest expected signal efficiency is kept, i.e. in the order: 4μ, $2e2\mu$, $2\mu2e$, $4e$. Finally, if there are more than four leptons present in the event, an effort is made to find the most SM Higgs boson signal-like quadruplet. The matrix element squared of a SM Higgs boson decaying to a pair of Z bosons ($M^2_{H\to ZZ^*}$) are calculated for all possible combinations of four leptons in the event, and the four leptons with the highest value of the matrix element squared are determined as the Higgs boson decay products. The matrix element is calculated at LO using MadGraph5_aMC @NLO [67] generator and assuming the invariant mass of the four leptons as the SM Higgs boson mass.

Events satisfying all the above criteria are considered candidate signal events. The signal selection efficiency is estimated to be 31%, 21%, 17%, 16% for sub-channels 4μ, $2e2\mu$, $2\mu2e$, $4e$, respectively.

5.4 Mass Resolution in the $H\to ZZ^*\to 4\ell$ Detection

After the inclusive event selection, a search for Final State Radiation (FSR) photons and a Z-mass-constrained kinematic fit to the leading lepton pair are performed to improve the Higgs signal resolution.

The QED process of radiative photon production in Z boson decays is well modelled by simulation. Some of the FSR photons can be identified in the calorimeter and incorporated into the four-lepton measurement. This method includes a search for collinear (for muons) and non-collinear FSR photons (for both muons and electrons) with only one FSR photon allowed per event. After the FSR correction, the lepton four-momenta of the leading dilepton are recomputed using a Z-mass-constrained kinematic fit. The fit uses a Breit-Wigner Z line shape and a single Gaussian to model the lepton momentum response function with the Gaussian σ set to the expected resolution for each lepton. The Z-mass constraint improves the $m_{4\ell}$ resolution

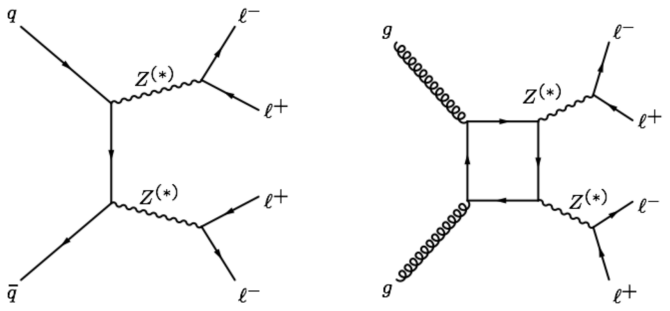

Figure 5.1: Representative diagrams for the quark-antiquark annihilation (5.1a) and gluon-initiated (5.1b) ZZ^* production processes. The particle $Z^{(*)}$ in the diagrams represents $Z^{(*)}/\gamma^*$.

by about 15%.

The Higgs boson mass resolution is expected to be about 1.6 GeV, 1.7 GeV, 2.1 GeV and 2.4 GeV for 4μ, $2e2\mu$, $2\mu2e$ and $4e$ sub-channels at the assumed Higgs boson mass $m_H = 125.09$ GeV, respectively.

5.5 Background Estimation

The main background component in the $H \to ZZ^* \to 4\ell$ channel is the continuum ZZ^* production. Representative diagrams for the quark-antiquark annihilation process and gluon-initiated process are shown in Figure 5.1. The continuum ZZ^* production is modelled using Monte Carlo (MC) simulations normalized to the SM predictions and validated in data sideband regions. The MC simulation samples used in the analyses are described in Section 7.1.2, 8.1.2.2 and 9.1.2.

Additionally, there are background sources including the Z+jets, $t\bar{t}$ and WZ processes, collectively referred to as reducible background, which are estimated with data. Considering the composition of the reducible background varies according to the flavor of the sub-leading lepton pairs ($\ell\ell\mu\mu$ and $\ell\ell ee$ final states), different approaches are taken to estimate them with data [68, 69]. The WZ production is included in the estimation with data in the $\ell\ell ee$ final states, while it is estimated using MC simulations for the $\ell\ell\mu\mu$ final states.

Other backgrounds come from the production of top quark-antiquark pairs in association with a vector boson $t\bar{t}V$ ($V = W, Z$) and triboson VVV production processes, which are minor and are estimated using MC simulations. In summary, Figure 5.2 presents the composition of the background in the Higgs signal region

with a mass range of 118 GeV $< m_{4\ell} <$ 129 GeV, which is used in the Higgs boson couplings measurement with the Run 2 data collected at $\sqrt{s} = 13$ TeV in 2015 and 2016.

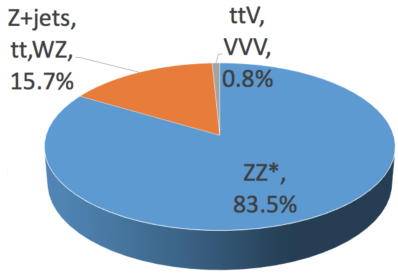

Figure 5.2: Background composition in the Higgs signal region with mass range 118 GeV $< m_{4\ell} <$ 129 GeV, in the analysis performed using the Run 2 data collected at $\sqrt{s} = 13$ TeV in 2015 and 2016.

5.6 Expected and Observed Events

The four-lepton invariant mass distributions in Run 1 and Run 2 after event selection criteria applied are shown in Figure 5.3. Table 5.1 presents the expected signal and background yields and the observed number of events in the signal region of 115 GeV $< m_{4\ell} <$ 130 GeV for the Higgs boson spin and parity study (Chapter VII) using the dataset collected at $\sqrt{s} = 7$, 8 and 13 TeV. Slightly higher number of events are observed in the dataset collected at $\sqrt{s}$ =8 and 13 TeV, which is not statistically significant. The mass range of 118 GeV $< m_{4\ell} <$ 129 GeV defines the signal region for the Higgs boson coupling measurements using the dataset collected at $\sqrt{s}$ =13 TeV (Chapter VIII). The corresponding numbers of expected and observed events are shown in Table 5.2.

5.7 Event Display

This section presents event display of several $H \to ZZ^* \to 4\ell$ candiate events passing the event selection criteria in Run-1 and Run-2 dataset.

A three-dimensional display is shown in Figure 5.4 [70] of a candidate Higgs boson event from pp collisions recorded by ATLAS at a center-of-mass energy of 7 TeV. The candidate event is reconstructed in the 4μ final state, with $m_{4\ell} = 145.8$ GeV. The masses of the lepton pairs are 94.3 GeV and 29.7 GeV, respectively. In the display, the purple lines show the four muon tracks.

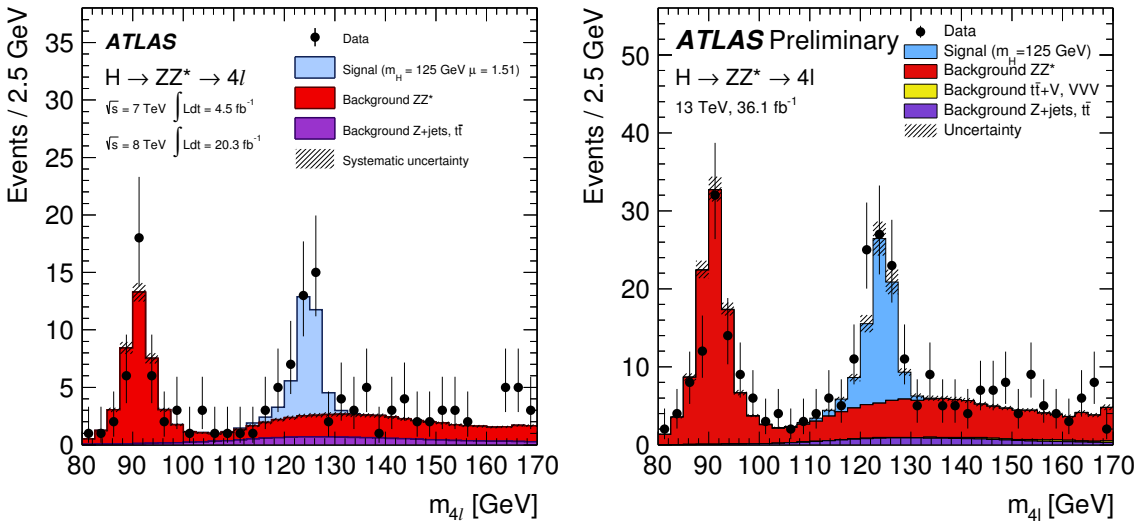

(a) (b)

Figure 5.3: Four-lepton invariant mass distribution after event selection criteria applied are shown with data candiates (black points), SM Higgs boson signal (red filled histogram) assmusing a mass of 125 GeV and normalized to a signal-strength of $\mu = 1.5$ in Run 1 5.3a and $\mu = 1$ in Run 2 5.3b, and background processes with systematic uncertainty (purple filled histogram).

Figure 5.5 [71] displays a candidate Higgs boson event from pp collisions recorded by ATLAS at a center-of-mass energy of 7 TeV. The candidate event is reconstructed in the $2e2\mu$ final state with $m_{4\ell} = 124.3$ GeV. The masses of the lepton pairs are 76.8 GeV and 45.7 GeV, respectively. In the three-dimensional display, the purple lines show the two muon tracks including the hits in the MS, the black lines show two electrons tracks.

Figure 5.6 presents a three-dimensional (central display) and a projection in the $r\phi$-plane (upper display) [72] of a candidate Higgs boson event from pp collisions recorded by ATLAS at a center-of-mass energy of 13 TeV. The candidate event is reconstructed in the $2e2\mu$ final state with $m_{4\ell} = 129$ GeV. The masses of the lepton pairs are 91 GeV and 29 GeV, respectively. In the display, the two muons tracks are indicated by the red lines, the two electrons tracks by the blue lines. The energy deposits in the electromagnetic calorimeter are shown in green, the deposits in the hadronic calorimeter in yellow. The two yellow cones present two jets in the event. the red lines show the two muon tracks including the hits in the MS, the green lines show two electrons tracks with the energy deposit in the electromagnetic calorimeter, and the violet cones present two jets. The p_{T} of the two electrons, muons, and jets

	SM Signal	ZZ^*	$t\bar{t}, Z+\text{jets}$	Total expected	Observed
$\int Ldt = 4.5$ fb^{-1}, $\sqrt{s} = 7$ TeV					
4μ	1.02±0.10	0.65±0.03	0.14±0.06	1.81±0.12	3
$2\mu 2e$	0.47±0.05	0.29±0.02	0.53±0.12	1.29±0.13	1
$2e2\mu$	0.64±0.06	0.45±0.02	0.13±0.05	1.22±0.08	2
$4e$	0.45±0.04	0.26±0.02	0.59±0.12	1.30±0.13	2
Total	2.58±0.25	1.65±0.09	1.39±0.26	5.62±0.37	8
$\int Ldt = 20.3$ fb^{-1}, $\sqrt{s} = 8$ TeV					
4μ	5.81±0.58	3.36±0.17	0.97±0.18	10.14±0.63	13
$2\mu 2e$	3.00±0.30	1.59±0.10	0.52±0.12	5.11±0.34	8
$2e2\mu$	3.72±0.37	2.33±0.11	0.84±0.14	6.89±0.41	9
$4e$	2.91±0.29	1.44±0.09	0.52±0.11	4.87±0.32	7
Total	15.4 ±1.5	8.72±0.47	2.85±0.39	27.0 ±1.6	37
$\int Ldt = 36.1$ fb^{-1}, $\sqrt{s} = 13$ TeV					
4μ	20.2±2.1	9.9±0.5	1.28±0.28	31.4±2.2	33
$2\mu 2e$	10.9±1.2	4.6±0.4	1.41±0.25	16.9±1.3	21
$2e2\mu$	14.1±1.4	7.1±0.4	1.02±0.23	22.3±1.5	31
$4e$	10.6±1.2	4.4±0.4	1.31±0.23	16.2±1.3	19
Total	56±6	26.0±1.5	5.0±0.6	87±6	104

Table 5.1: Expected signal, background and total yields, including their total uncertainties, and observed events in data, in the 115 GeV $< m_{4\ell} <$ 130 GeV signal region. The number of expected signal events is given for a SM Higgs boson mass of 125.5 GeVfor $\sqrt{s} = 7, 8$ TeV, and 125 GeVfor $\sqrt{s} = 13$ TeV.

is 111 and 16 GeV, 18 and 17 GeV, and 118 and 54 GeV, respectively. The two jets are separateby by a pseudorapidity difference of 6.4 and have an invariant mass of 2 TeV. This event has an high output score for the BDT_{2jVBF} discriminant described in Section 8.1.3.5, thus is consistent with the topology of the VBF production of a Higgs boson decaying to four leptons.

Figure 5.7 [70] displays a candidate Higgs boson event produced with $m_{4\ell} = 119$ GeV in the $2\mu 2e$ final state from pp collisions recorded by ATLAS at a center-of-mass energy of 13TeV. The candidate event is reconstructed in a beam crossing with 25 additionally reconstructed primary vertices from the minimum bias interactions. The masses of the lepton pairs are 69 GeV and 42 GeV, respectively. In the display, all

Final state	Signal	ZZ^*	Other backgrounds	S/B	Total expected	Observed
4μ	19.7 ± 2.1	7.5 ± 0.4	1.00 ± 0.21	2.3	28.1 ± 2.1	32
$2e2\mu$	13.5 ± 1.4	5.35 ± 0.29	0.78 ± 0.17	2.2	19.7 ± 1.4	30
$2\mu 2e$	10.4 ± 1.2	3.57 ± 0.29	1.09 ± 0.19	2.2	15.1 ± 1.2	18
$4e$	9.9 ± 1.2	3.35 ± 0.31	1.01 ± 0.17	2.3	14.3 ± 1.2	15
Total	54 ± 6	19.7 ± 1.3	3.9 ± 0.5	2.3	77 ± 6	95

Table 5.2: The number of expected and observed events passing event selection criteria and in the mass range of 118 GeV $< m_{4\ell} <$ 129 GeV with an integrated luminosity of 36.1 fb^{-1} collected at $\sqrt{s} = 13$ TeV. The signal process is assuming the SM Higgs boson with a mass of 125.09 GeV.

the tracks with p_{T} above 4 GeV are included, in which the red lines show the two muon tracks including the hits in the MS, the green lines show two electrons tracks with the energy deposit in the electromagnetic calorimeter. As shown in the lego plot on the bottom right, the p_{T} of the two muons and electrons is 29 and 31 GeV, 23 and 19 GeV, respectively. This event has a high output score for the BDT_{ZZ} discriminant which will be described in Section 8.1.3.5, thus has a high probability of being produced in the $H \to ZZ^* \to 4\ell$ process.

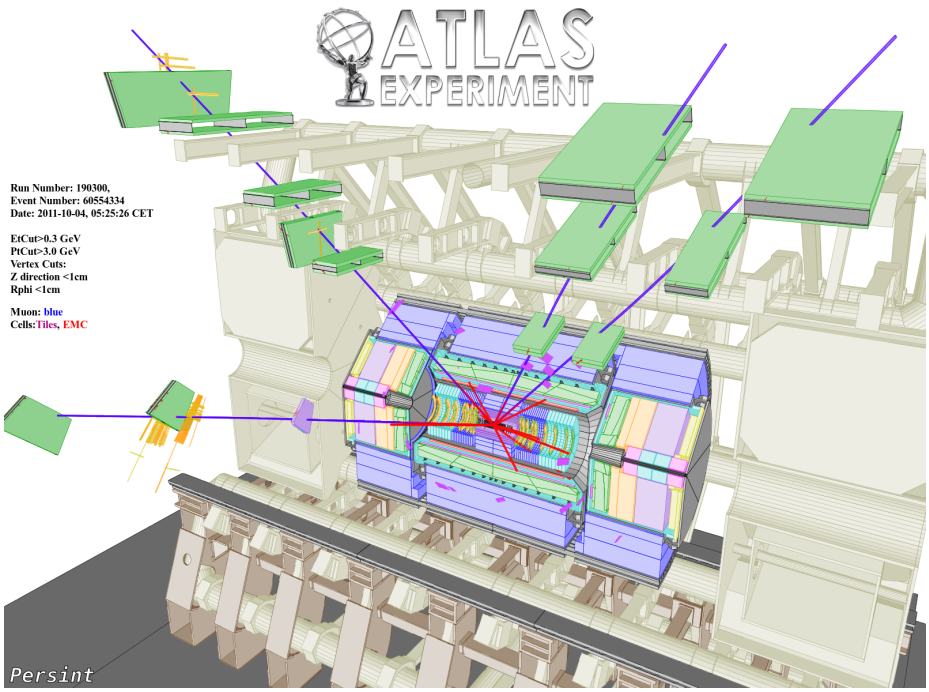

Figure 5.4: Display of a candidate Higgs boson event in the 4μ final state with the event number 60554334 and run number 190300 in pp collisions recorded by ATLAS at a center-of-mass energy of 7 TeV.

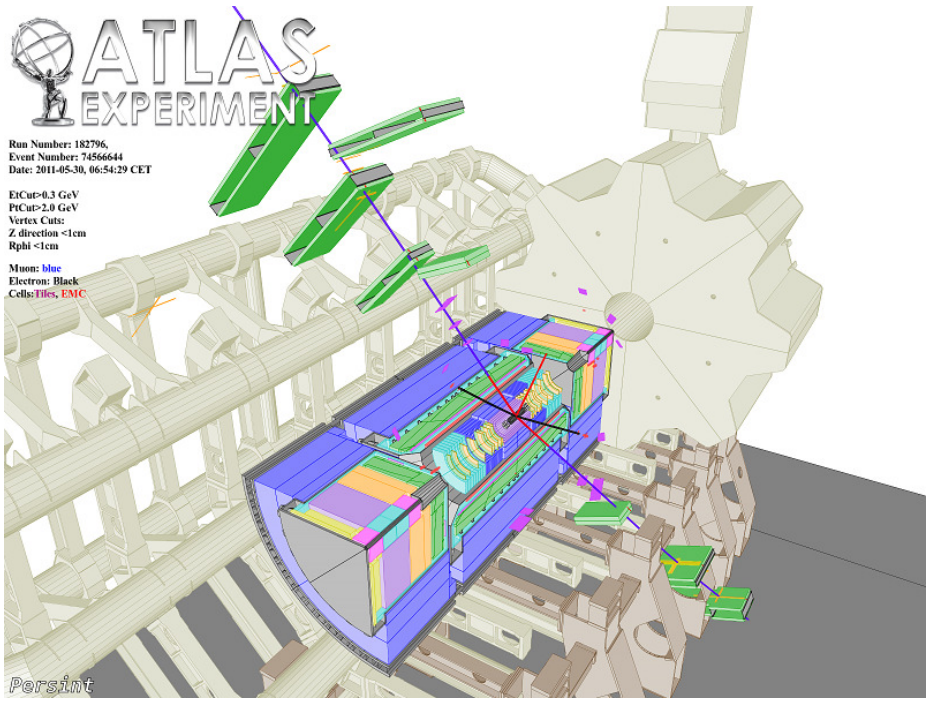

Figure 5.5: Display of a candidate Higgs boson event in the $2e2\mu$ final state with the event number 74566644 and run number 182796 in pp collisions recorded by ATLAS at a center-of-mass energy of 7 TeV.

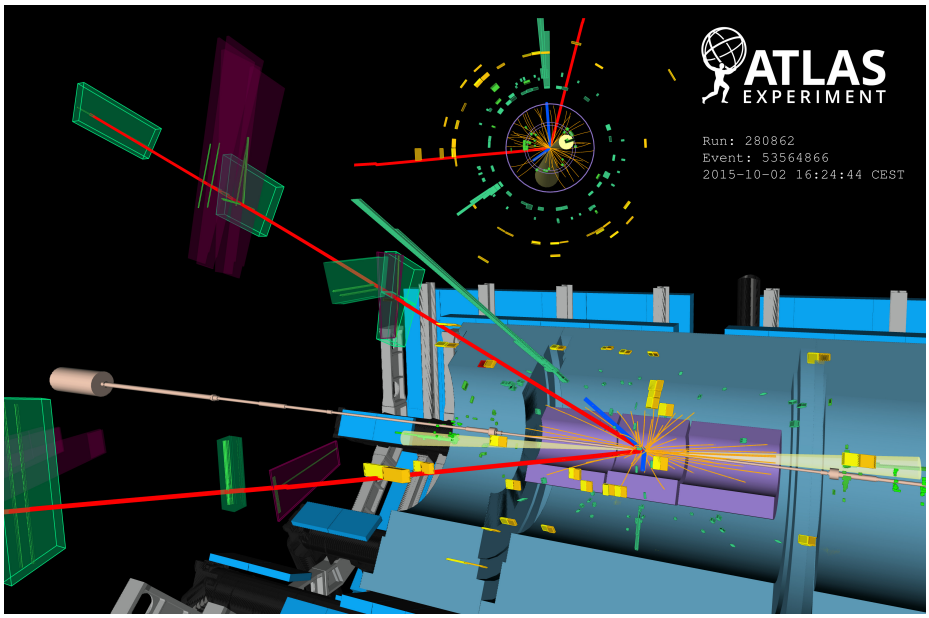

Figure 5.6: Another display of a candidate Higgs boson event in the $2e2\mu$ final state with the event number 74566644 and run number 182796 in pp collisions recorded by ATLAS at a center-of-mass energy of 13 TeV. The topology of the event is consistent with the VBF production of a Higgs boson.

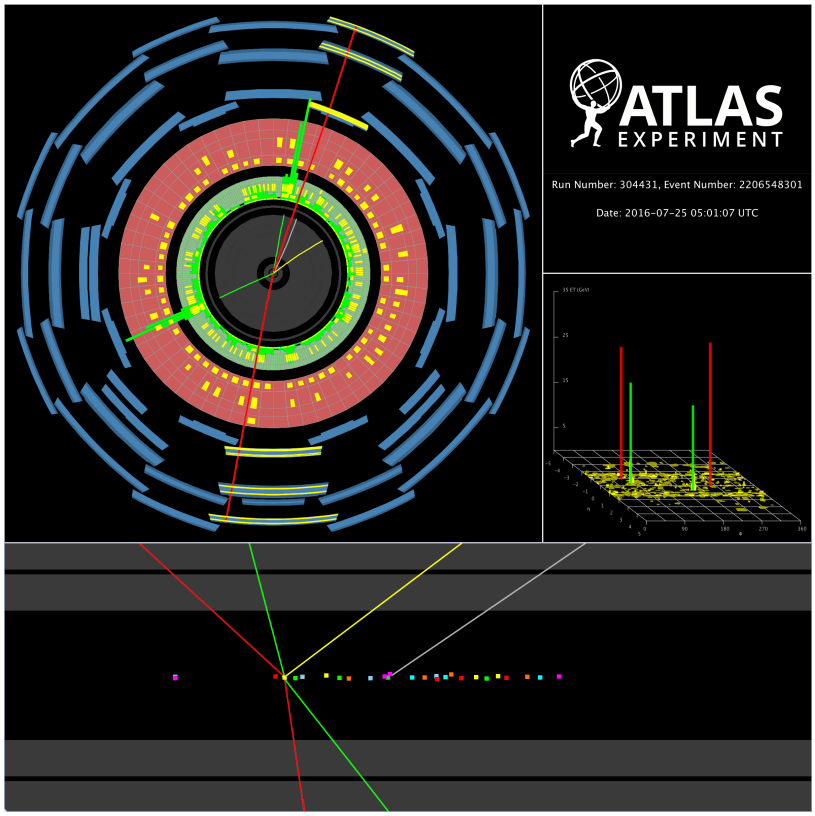

Figure 5.7: Display of a candidate Higgs boson event in the $2\mu 2e$ final state with the event number 2206548301 and run number 304431 in pp collisions recorded by ATLAS at a center-of-mass energy of 13 TeV. The candidate event is reconstructed in a beam crossing with 25 additionally reconstructed primary vertices from the minimum bias interactions. All the tracks with p_{T} above 4 GeV are included, in which the red lines show the two muon tracks including the hits in the MS, the green lines show two electrons tracks with the energy deposit in the electromagnetic calorimeter.

CHAPTER VI

Statistical Method

Statistical method is the bridge connecting the data selected in a certain physics analysis and the physics quantity that we aim to probe or measure. The probability of an event to happen is determined by the underlying physics laws. Thus, the experimental data are random by nature. Furthermore, fluctuations in the detector response such as scale, resolution and efficiency and etc., also introduce uncertainties in the data. In this chapter, we will discuss the statistical method used in this dissertation in the statistical modeling and the procedure to estimate from the data the central value or upper limit and the associated uncertainties of the physics quantities under study.

6.1 Statistical Modeling

6.1.1 Parameterization

Parameters (α) in physics analyses in this dissertation can be separated into two groups, the parameter of interest denoted as μ and nuisance parameters denoted as θ hereafter, thus $\alpha = (\mu, \theta)$.

The parameter of interest μ, stands for the quantity the analysis is aiming to measure. In the Higgs boson coupling measurements under the κ-framework which will be discussed in Chapter VIII, the parameters of interest are the couplings modifiers κ_F and κ_V.

Nuisance parameters θ represent certain aspects of the analysis, such as physics object construction and identification efficiencies, energy scale and resolution, luminosity measurement uncertainty, and the theoretical uncertainties for signal and background modeling and estimation, some of which are estimated from dedicated auxiliary measurements, such as control regions, sidebands, data-driven background estimates and

calibration measurements. The auxiliary measurement $f_{aux}(D_{aux} \mid \alpha_p, \alpha_{other})$ provides a maximum likelihood estimate for α_p, a_p, and a standard error σ_p. Thus, the probability model for an auxiliary measurement $f_p(a_p \mid \alpha_p, \sigma_p)$, referred to as constraint terms hereafter, can be approximately modelled using a Gaussian function:

$$f(a_p \mid \alpha_p, \sigma_p) = Gauss(a_p \mid \alpha_p, \sigma_p). \tag{6.1}$$

In case of an intrinsically non-negative parameter where the Gaussian function does not apply, such as event yields and energy scale uncertainties, or in case of a parameter which is not associated with an auxiliary measurement, such as theoretical uncertainties from the choice of renormalization and factorization scales and missing higher-order corrections in a theoretical calculation, the constraint term can take the form of the log-normal distribution, which is given by:

$$f(a_p \mid \alpha_p, \kappa) = \frac{1}{\sqrt{2\pi} a_p \ln \kappa} e^{-\frac{(\ln(a_p/\alpha_p))^2}{2(\ln \kappa)^2}} \tag{6.2}$$

where $\kappa = 1 + \sigma_p/a_p$.

6.1.2 Likelihood Construction

In experimental high energy physics, Poisson distribution

$$Pois(n_c \mid \nu_c(\alpha)) = \frac{e^{-\nu_c(\alpha)} \nu_c(\alpha)^{n_c}}{n_c!} \tag{6.3}$$

is often used to model the possibility of the number of events observed in data (n_c) when the expected average number of events is $\nu(\alpha)$ in an analysis channel or category c [1], which is defined by certain event selection criteria.

In addition to a counting experiment based on the number of selected events, discriminating variables are often used to distinguish between different processes. As an instance, in the search for new resonances in the four-lepton final state which will be discussed in Chapter IX, the invariant mass of the four-lepton system ($m_{4\ell}$) is used to separate the signal from background processes. Denoting the discriminating variable as x, the probability density function (pdf) can be written as $f(x|\alpha)$.

For a channel with n_c events observed in the dataset, the data are represented by a set of values of the discriminating variables for each event $D_c = \{x_{1,c}, x_{2,c}, ..., x_{n_c,c}\}$. The probability model for this type of data is referred to as an unbinned extended

[1] A channel or category is referred to as a channel in this chapter

likelihood or marked Poisson model [2]. The likelihood model L_c for channel c, can be expressed in Equation 6.4:

$$F_c(D \mid \alpha) = Pois(n_c \mid \nu_c(\alpha)) \prod_{e=1}^{n_c} f(x_{e,c} \mid \alpha) \tag{6.4}$$

where the event rate and pdf could have contributions from several individual processes, such as different Higgs boson production processes and background processes in the Higgs boson couplings measurement as described in Chapter VIII. The total rate is the sum of the rates from individual processes

$$\nu_c(\alpha) = \sum_{k \in processes} \nu_{c,k}(\alpha) \tag{6.5}$$

and the total pdf is the weighted sum of the individual pdfs

$$f_c(x \mid \alpha) = \frac{1}{\nu_c(\alpha)} \sum_{k \in processes} \nu_{c,k}(\alpha) f_{c,k}(x \mid \alpha) \tag{6.6}$$

An analysis may include several channels, for instance, the mine categories used in the Higgs boson couplings measurement described in Chapter 8.1.3. The channels are combined by multiplying the likelihood of each channel, and the combined model can be written as

$$L_{comb}(D_{comb} \mid \alpha) = \prod_{c=1}^{N} [Pois(n_c \mid \nu_c(\alpha)) \prod_{e=1}^{n_c} f(x_{e,c} \mid \alpha)] \tag{6.7}$$

where e and c is the event index and channel index, respectively. n_c is the number of events observed in channel c, and N is the total number of channels in included in the analysis. $x_{e,c}$ denotes the value of the discriminating variable of the e^{th} event in the c^{th} channel. The combined data are a set of data from individual channels: $D_{comb} = \{D_1, D_2, ..., D_N\}$.

As the last step in constructing the full likelihood, the constraint terms for the nuisance parameters are multiplied to Equation 6.7, thus the full model can be written as

$$L_{com}(D_{com}, G \mid \alpha) = \prod_{c=1}^{c_{max}} [Pois(n_c \mid \nu_c(\alpha)) \prod_{e=1}^{n_c} f(x_e^c \mid \alpha)] \cdot \prod_{p \in S} f(a_p \mid \alpha_p, \sigma_p). \tag{6.8}$$

[2] If the pdfs use the distribution of binned histogram, the unbinned extended likelihood is equivalent to binned extended likelihood.

where the set of nuisance parameters constrained by auxiliary measurements is denoted as S and a set of estimates of those parameters, also referred to as global observables, is denoted $G = a_p$ with $p \in S$.

6.2 Statistical Approach

A test statistic is used in statistical hypothesis testing as a gauge to distinguish the null from the alternative hypothesis. Two kinds of test statistics are used in the analyses in this dissertation. The profile likelihood ratio test statistic [73] is used to derive confidence intervals or an upper limit on a measured quantity, and to obtain levels of compatibility between the two hypothesis. The Higgs boson production and rate measurement in Chapter VIII and the search for new resonances in the four-lepton final state in Chapter IX, both use the profile likelihood ratio test statistic. The other test statistic is ratio of likelihoods, which is used in the spin and parity study of the Higgs boson discussed in Chapter VII.

The test statistic is defined such that larger values imply increasing level of disagreement, which can be quantified in terms of p-value

$$p(\mu) = \int_{t_{\mu,obs}}^{\infty} f(t_\mu \mid \mu) dt_\mu \tag{6.9}$$

which is calculated by integrating the corresponding distribution of the test statistic $f(t_\mu \mid \mu)$ above the observed value of the test statistic in data $t_{\mu,obs}$.

The distribution of the test statistic, $f(t_\mu \mid \mu)$, can be obtained by the ensemble from Monte Carlo pseudo-experiments. This approach is used in the spin and parity study of the Higgs boson. In case of the profile likelihood ratio test statistic and the statistics in data is sizable, $f(t_\mu \mid \mu)$ can be well approximated by explicit formulae [73], which will be discussed in more detail later in this Chapter. This approximation method is used in the Higgs boson production and rate measurements in Chapter VIII and the search for new resonances in the four-lepton final state in Chapter IX.

In particle physics, the p-value can be converted into an equivalent significance Z, defined as

$$Z = \Phi^{-1}(1 - p) \tag{6.10}$$

where Φ^{-1} is the quantile of the standard Gaussian function. In search for new physics, to constitute a discovery in particle physics, a significance of at least $Z = 5\sigma$

is needed to reject the background hypothesis. This corresponds to a p-value of 2.87×10^7. $Z = 3\sigma$ indicates evidence for new physics. In case no evidence of new physics is observed in data, an upper limit μ_{up} for the new physics process is often set at 95% modified confidence level CL_s [74], where μ_{up} satisfies $CL_s(\mu_{up}) = 95\%$ and CL_s is defined as:

$$CL_s(\mu) = \frac{p_\mu}{1 - p_b} \tag{6.11}$$

where p_μ is the p-value for the signal with size μ plus background hypothesis and p_b for the background-only hypothesis. The CL_s procedure is formulated to ensure that a signal hypothesis would not be excluded when the sensitivity of the experiment is little.

For a measurement, the confidence level (CL) intervals or contours of the measured quantity are defined such that the boundaries of $100(1 - \beta)\%$ CL intervals $[\mu_1, \mu_2]$, satisfy $P(\mu_1) = P(\mu_2) = \beta$.

6.2.1 Profile Likelihood Ratio

For a given dataset D_{com}, the likelihood function 6.8 is referred to $L(\mu, \theta)$ for short, hereafter. The likelihood ratio is constructed to be,

$$\Lambda(\mu) = \frac{L(\mu, \hat{\hat{\theta}}(\mu))}{L(\hat{\mu}, \hat{\theta})} \tag{6.12}$$

where $\hat{\mu}$ and $\hat{\theta}$ are the maximum likelihood estimates (MLEs) for parameters of interest and nuisance parameters respectively, which are the values of the parameters that maximize the likelihood function $L(\mu, \theta)$. $\hat{\hat{\theta}}$ is the conditional maximum likelihood estimate of θ which maximizes the likelihood function with parameters of interest fixed to a certain value. It can be seen that by definition, $0 \leq \lambda \leq 1$, and λ value near 1 indicating good agreement between the data and the hypothesized value of μ, and smaller values indicating increasing level of disagreement between the two.

In case the parameter of interest is physically non-negative, $\mu > 0$, an alternative likelihood ratio is defined as:

$$\tilde{\Lambda}(\mu) = \begin{cases} \frac{L(\mu, \hat{\hat{\theta}}(\mu))}{L(\hat{\mu}, \hat{\theta})}, & \hat{\mu} \geq 0 \\ \frac{L(\mu, \hat{\hat{\theta}}(\mu))}{L(0, \hat{\hat{\theta}}(0))}, & \hat{\mu} < 0 \end{cases} \tag{6.13}$$

6.2.1.1 Test Statistic t_μ

The profile likelihood test statistic is defined as

$$t_\mu = -2 \ln \Lambda(\mu) \tag{6.14}$$

to measure the level of disagreement between the data and the hypothesized value of μ. The sampling distribution of t_μ can be well approximated by a chi-square distribution with n degree of freedom $\chi^2_n(t_\mu)$ [73]:

$$f(t_\mu \mid \mu) \approx \chi^2_n(t_\mu) \tag{6.15}$$

where n is the number of parameters of interest. The value of t_μ close to 0 means agreement between the data and the hypothesized value of μ, while larger values imply increasing level of disagreement, which can be quantified in terms of the p-value defined in Equation 6.9:

$$p(\mu) = \int_{t_{\mu,obs}}^{\infty} \chi^2_n(t_\mu) dt_{t_\mu}, \tag{6.16}$$

which can convert to the corresponding Gaussian significance using Equation 6.10. For one degree of freedom $n = 1$, 68.3% ($Z = 1\sigma$), 95.4% ($Z = 2\sigma$), and 99.7% ($Z = 3\sigma$) CL intervals are given by the values of μ which satisfy $t_\mu = 1.0$, 4.0 and 9.0, respectively. In this dissertation, the values of μ are obtained by a numerical method. As an example, Figure 6.1 shows, in the measurement of the combined ggF and bbH production in the $H \to ZZ^* \to 4\ell$ channel (parameter of interest $\mu = (\sigma \cdot B)^{\rm ZZ}_{\rm ggF}$) which will be discussed in Section 8.1, the test statistic t_μ (or $-2 \ln \Lambda$ displayed in Figure 6.1) versus $(\sigma \cdot B)^{\rm ZZ}_{\rm ggF}$ distribution obtained by using Spline to interpolate individual ($(\sigma \cdot B)^{\rm ZZ}_{\rm ggF}$, t_μ) points. The expected experimental sensitivity and observed results in data are obtained by fitting the likelihood to the Asimov data [73] and to the data, respectively. The μ values where the Spline and lines $t_\mu = 1, 4, 9$ cross give the 68.3%, 95.4% and 99.7% CL intervals. This kind of plot is referred to as NLL scan hereafter.

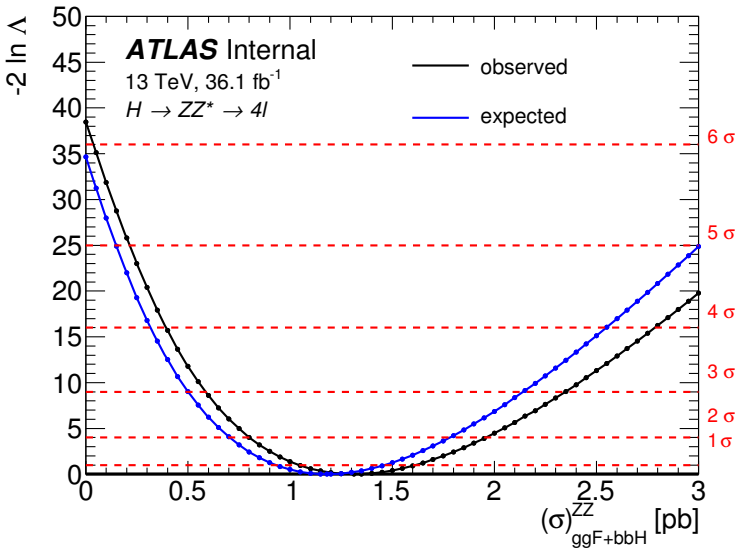

Figure 6.1: NLL scan to measure $(\sigma \cdot B)^{ZZ}_{ggF+bbH}$, the combined ggF and bbH production in the $H \to ZZ^* \to 4\ell$ channel. The blue and black lines show the NLL scans for the expected experimental sensitivity and observed results in data, respectively.

6.2.1.2 Test Statistic q_0 for Discovery of a Positive Signal Process

The statistic for the discovery of a positive signal is defined as:

$$q_0 = \begin{cases} -2\ln\Lambda(0), & \hat{\mu} \geq 0 \\ 0, & \hat{\mu} < 0. \end{cases} \tag{6.17}$$

The sampling distribution of q_0 can be well approximated by:

$$f(q_0 \mid 0) \approx \frac{1}{2}\delta(q_0) + \frac{1}{2\sqrt{2\pi q_0}} e^{-q_0/2}. \tag{6.18}$$

Therefore, the p-value to quantify the compatibility with background-only hypothesis are calculated using the equation:

$$p(\mu) = 1 - \Phi(\sqrt{q_0}) \tag{6.19}$$

where Φ represents the cumulative distribution function of the standard Gaussian distribution. The corresponding signal significance can be calculated by:

$$Z(\mu) = \sqrt{q_0}. \tag{6.20}$$

As an example shown in Figure 6.1, the expected and observed ggF significance in data are found to be $\sqrt{-2\ln\Lambda(0)} = 5.8\sigma$ and 6.2σ, respectively.

6.2.1.3 Test Statistic $\tilde{q}$ for Upper Limits

An upper limit is often set in a search when no significant excess over background is observed in data. The test statistic for upper limit of a signal process is defined as

$$\tilde{q}_\mu = \begin{cases} -2\ln\tilde{\Lambda}(\mu), & \hat{\mu} \geq \mu \\ 0, & \hat{\mu} < \mu. \end{cases} \tag{6.21}$$

The presentation of upper limits in this dissertation are set at 95% CL_s including the observed limit in data, the expected limit which is the median upper limit under the background-only hypothesis, a $\pm 1\sigma$ and a $\pm 2\sigma$ expected limit band, as shown in Figure 9.2 for instance. The method to calculate the upper limit is described in detail in Ref. [75, 76].

6.2.2 Ratio of Profiled Likelihoods

The ratio of profiled likelihoods test statistic applicable in a hypothesis test. Denoting the null and alternative hypothesis as H_0 and H_1, the ratio of profiled likelihoods is defined as

$$\tilde{q} = \ln \frac{\mathcal{L}(H_1, \hat{\hat{\theta}}_{H_1})}{\mathcal{L}(H_0, \hat{\hat{\theta}}_{H_0})}, \tag{6.22}$$

where $\hat{\hat{\theta}}_{H_0}$ and $\hat{\hat{\theta}}_{H_1}$ are the conditional maximum likelihood of the nuisance parateters which maximizes the likelihood function for the null and alternative hypothesis, respectively. This test statistic is used in the Higgs boson spin and parity study the and the method is described in detail in Section 7.1.3.

The implementation of the statistical modeling and procedures is based on the RooFit [77], RooStats [78], and HistFactory [79] packages.

CHAPTER VII

Studies of Higgs Boson Spin and Parity

In the Standard Model (SM), the Higgs boson is a spin-0 particle with even parity. Studying the spin and parity of the newly discovered boson is hence crucial in confirming whether it is the Higgs boson SM predicted. The $H \to ZZ^* \to 4\ell$ channel plays a pivotal role in this study due to the fully reconstructed final state and the rich angular information in the final state. A two-dimensional analysis method based on Boosted-Decision-Tree (BDT) is used to separate the SM hypothesis from non-SM spin and parity hypotheses and to improve background rejection. This method achieves similar sensitivity and serves as an independent study, to cross-check the baseline method based matrix-element discriminant in the Run 1 ATLAS Higgs Spin/CP legacy paper [80]. To maximize the experimental sensitivity regarding the Higgs boson spin and parity, the studies in the diboson decay channels ($\gamma\gamma$, ZZ^*, WW^*) are combined.

7.1 Signal and Background Simulation

7.1.1 Signal Simulation

The SM Higgs boson ggF production is modelled using the Powheg-Box [81] generator at NLO, interfaced to Pythia 8 for parton showering and hadronization. To improve the modeling of the SM Higgs boson $p_{\mathrm{T,H}}$, each MC event is reweighted so that $p_{\mathrm{T,H}}$ matches the prediction of the NNLO and next-to-next-to-leading-logarithms (NNLL) dynamic-scale calculation given by the HRes2.1 [82, 83] program.

For the non-SM signals, the spin-2 samples are generated at LO using the MadGraph5_aMC [84] generator. The spin-0 samples are generated using Powheg-Box generator for the signal production process and using JHU [85, 86] generator at LO for the decay process.

7.1.2 Background Simulation

The ZZ^* continuum background is modelled using Powheg-Box [81] for quark-antiquark annihilation and gg2ZZ [87] for gluon-initiated process. The PDF+α_s and QCD scale uncertainties are parametrized as functions of $m_{4\ell}$ following the recommendation in [88]. For the ZZ^* background in the Higgs signal region of $115 < m_{4\ell} < 130$ GeV, the quark and gluon-initiated processes have a QCD scale uncertainty of $\pm 5\%$ and $\pm 25\%$, and PDF+α_s uncertainty of $\pm 4\%$ and $\pm 8\%$, respectively. Sherpa [89] generator is used for the simulation of WZ production.

7.1.3 Statistical Modeling

A likelihood function, $\mathcal{L}(\text{data} \mid J^P, \mu, \theta)$, that depends on the spin-parity assumption of the signal is constructed as a product of conditional probabilities over binned distributions of the discriminant observables in each channel:

$$\mathcal{L}(\text{data} \mid J^P, \mu, \theta) = \prod_{c}^{N_{\text{chann.}}} \prod_{i}^{N_{\text{bins}}} Pois\big(n_{i,c} \mid \mu_c \cdot S_{i,c}^{(J^P)}(\theta) \; + B_{i,c}(\theta)\big) \cdot f_c(\theta) \; , \qquad (7.1)$$

where the inclusive signal strength parameter introduced in Section 2.2.4.4, μ_c, represents the measured signal production cross section divided by the SM Higgs boson prediction in the Higgs decay channel c and under a certain spin-parity assumption of the signal. The likelihood function is a product of Poisson distributions $Pois$ corresponding to the observation of $n_{i,c}$ events channel c and in bin i of the discriminant observables, given the expectations for the signal, $S_{i,c}^{(J^P)}(\theta)$, and for the background, $B_{i,c}(\theta)$. The symbol θ represents nuisance parameters, and the corresponding constraint terms are represented by the functions $f_c(\theta)$.

While the couplings are predicted for the SM Higgs boson, they are not known *a priori* for the BSM hypotheses introduced in Section 2.2.4.3. In order to be insensitive to assumptions on the couplings of the BSM resonance to SM particles, the numbers of signal events in each Higgs decay channel, for each different LHC centre-of-mass energy and for each tested hypothesis, are free parameters in the model. This is included in the likelihood by having independent parameters μ_c parameter for each decay channel in the likelihood.

The test statistic $\tilde{q}$ used to distinguish between the two tested spin-parity hy-

potheses is a ratio of profiled likelihoods [90, 91]:

$$\tilde{q} = \ln \frac{\mathcal{L}(J^P_{SM}, \hat{\hat{\mu}}_{J^P_{SM}}, \hat{\hat{\theta}}_{J^P_{SM}})}{\mathcal{L}(J^P_{BSM}, \hat{\hat{\mu}}_{J^P_{BSM}}, \hat{\hat{\theta}}_{J^P_{BSM}})} \tag{7.2}$$

where $\mathcal{L}(J^P, \hat{\hat{\mu}}_{J^P}, \hat{\hat{\theta}}_{J^P})$ is the conditional maximum likelihood value evaluated under either the SM $J^P_{SM} = 0^+$ or the BSM J^P_{BSM} spin-parity hypothesis. The parameters $\hat{\hat{\mu}}_{J^P}$ and $\hat{\hat{\theta}}_{J^P}$ represent the values of the signal strength and nuisance parameters fitted to the data under each spin and parity hypothesis.

The distributions of the test statistic for both the J^P_{SM} and the J^P_{BSM} hypotheses are obtained using ensemble of all possible outcome from MC pseudo-experiments. For each hypothesis test, about 100 000 such pseudo-experiments were generated. The generation of the pseudo-experiments uses the numbers of signal and background events in each channel obtained from the conditional maximum likelihood fits to data under either the SM $J^P_{SM} = 0^+$ or the BSM J^P_{BSM} spin-parity hypothesis. In the fits of each pseudo-experiment to get the corresponding $\tilde{q}$ value, parameters are profiled, i.e. fitted to the value that maximizes the likelihood for each value of the parameter of interest.

The distributions of $\tilde{q}$ are used to determine the corresponding p-values $p(J^P_{SM}) = p^{\mathrm{SM}}$ and $p(J^P_{BSM}) = p^{\mathrm{BSM}}$. For a tested hypothesis J^P_{BSM}, the observed (expected) p-values are obtained by integrating the corresponding distributions of the test statistic above the observed value of $\tilde{q}$ (above the median of the J^P_{SM} $\tilde{q}$ distribution). Very small values of the integral of the distribution of the test statistic for the J^P_{BSM} hypothesis, corresponding to large values of $\tilde{q}$, are interpreted as the data being in disagreement with the tested hypothesis in favor of the SM hypothesis. The exclusion of the alternative J^P_{alt} hypothesis in favor of the SM J^P_{SM} hypothesis is evaluated in terms of the modified confidence level $CL_s(J^P_{BSM})$, defined as [74]:

$$CL_s(J^P_{BSM}) = \frac{p(J^P_{BSM})}{1 - p(J^P_{SM})} \tag{7.3}$$

7.2 Studies of Spin and Parity in the Four-lepton Decay Channel

Events with an invariant mass of the four-lepton system between 115 and 130 GeV are used in the analysis. The selected events are then classified into four categories depending on the flavor of the leptons: $4\mu, 4e, 2e2\mu, 2\mu2e$, which improves the sen-

sitivity of the spin and parity study comparing to one inclusive category due to the categories with higher sigal-over-background ratio will have a bigger weight in the combined results including all categories. Each category uses the BDT output score of the spin and parity sensitive BDT to separate the two tested signal hypothesis and the background rejecting BDT_{ZZ} discriminants to build the two-dimentional model. This section will discuss the spin and parity sensitive observables, the BDT dicriminants, systematic uncertainties and the results for the study of spin and parity in the $H \to ZZ^* \to 4\ell$ channel using the BDT approach.

7.2.1 Spin and Parity Sensitive Observables

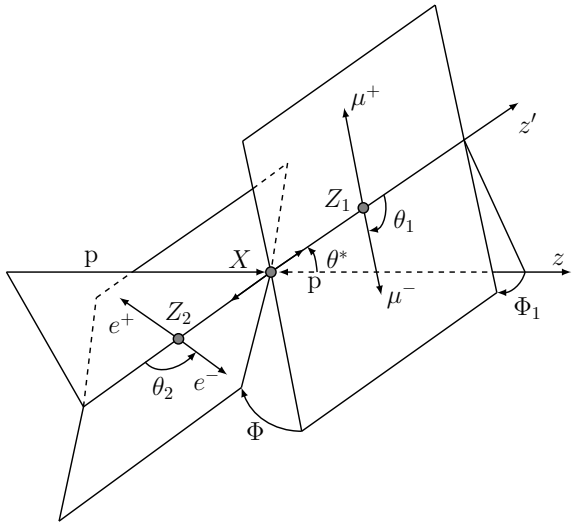

Figure 7.1: Definitions of the angular observables sensitive to the spin and parity of the resonance in the $X \to ZZ^* \to 4\ell$ decay.

The final-state observables sensitive to the spin and parity of a boson decaying to $ZZ^* \to 4\ell$ are two production angles θ^* and Φ_1, three decay angles Φ, θ_1 and θ_2, and two masses m_{12} and m_{34} which are the invariant masses of the leading and subleading lepton pair. The angles are defined in the four-lepton rest frame in the following way and are illustrated in Figure 7.1:

- θ_1 and θ_2 are the angles between the negative-charged leptons in the final state and the direction of flight of their associated Z bosons;
- Φ is the angle between the two decay planes formed by the two lepton pairs from Z boson decays;

- Φ_1 is the angle between the decay plane of the leading lepton pair and a plane defined by the momentum of the Z boson associated with the leading lepton pair (Z_1) in the positive z direction;

- θ^* is the production angle of the Z_1 formed by the direction of Z_1 momentum and the positive z direction.

In the case of a spin-0 boson, the production variables $\cos(\theta^*)$ and Φ_1 are not sensitive, since the resonance has no spin axis with which one can define these angles. Representative distributions of the final-state observables sensitive to the spin and parity of the decaying resonance are presented in Figure 7.2, where the events observed in data are superimposed with the distributions for the SM $J^P = 0^+$ and non-SM $J^P = 0^-$ simulated events, as well as for ZZ^* production and reducible backgrounds in the signal region of 115 GeV $< m_{4\ell} <$ 130 GeV.

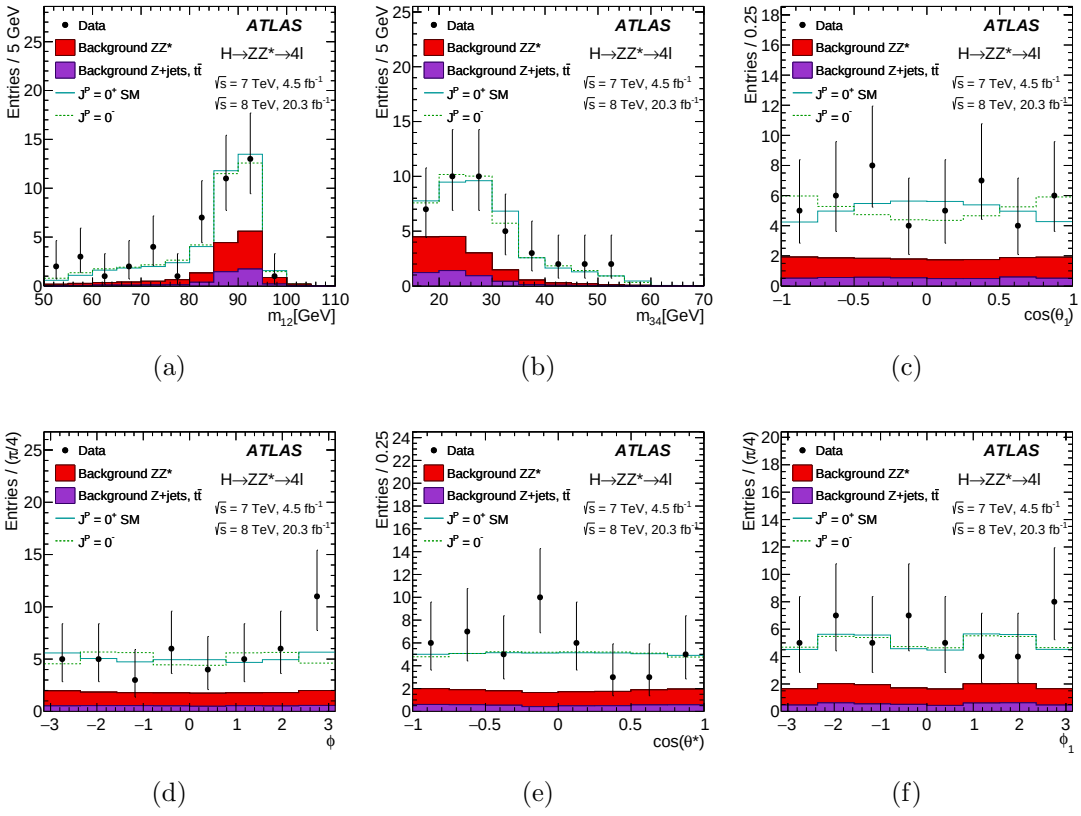

Figure 7.2: Distributions of representative final-state observables sensitive to the spin and parity of the resonance in the signal region 115 GeV $< m_{4\ell} <$ 130 GeV with data (points with errors), backgrounds (filled histograms) and two signal hypotheses SM 0^+ in solid green line and non-SM $J^P = 0^-$ in dashed green line.

7.2.2 BDT Discriminants

As seen in Figure 7.2, it is hard to distinguish 0^+ and 0^- hypothesis, therefore a multivariate analysis BDT approach is used to improve the sensitivity. The spin and parity hypothesis test is based on two kinds of BDT discriminant. One kind to distinguish between different spin and parity hypotheses (BDT discriminant), and the other kind to separate background processes from the signal (BDT_{ZZ} discriminant). The two-dimensional BDT output score is used as discriminant in the likelihood. The BDT discriminants are trained on the following variables based on MC simulations:

- $J^P = 0^+$ vs. 0^- and 0^+ vs. 0_h^+: m_{12}, m_{34}, $\cos(\theta_1)$, $\cos(\theta_2)$, ϕ
- $J^P = 0^+$ vs. 2^+ including universal and non-universal couplings: m_{12}, m_{34}, $\cos(\theta_1)$, $\cos(\theta_2)$, ϕ, $\cos(\theta^*)$, ϕ_1
- SM Higgs vs. continuum ZZ^*: $m_{4\ell}$, $p_{\mathrm{T},4\ell}$, $\eta_{4\ell}$, D_{ZZ^*}

where $m_{4\ell}$, $p_{\mathrm{T},4\ell}$, and $\eta_{4\ell}$ are the invariant mass, transverse momentum, and pseudo-rapidity of the four-lepton system, respectively. The Kinematic Discriminant (D_{ZZ^*}) is defined based on two matrix-elements:

$$D_{ZZ^*} = \ln(\frac{M_{sig}^2}{M_{ZZ}^2}) \tag{7.4}$$

where M_{sig} corresponds to the matrix element for the signal process, assuming the SM Higgs boson spin and parity quantum number 0^+ and the mass of signal to be $m_{4\ell}$. M_{ZZ} is the matrix element for the ZZ^* background process. Both matrix elements are computed at LO using MadGraph5 [67].

The BDT training was performed using the TMVA toolkit [92] using gradient boosting and bagging resampling method. The parameters of the BDT training setup includes shrinkage for the learning rate for the GradBoost algrithm (Shrink.), node purity limit (MNP), signal over background ratio (S/B), bagged sample fraction (BSF), number of grid points in variable range used to find the optimal cut in node splitting (N_{Cuts}), and the max depth of the decision tree allowed (MaxDepth). The values found to provide the largest separation power without the BDTs being overtrained and hence adopted in the analysis are summarized in Table 7.1.

The spin and parity BDT training is performed with the four different final states included, while the BDT_{ZZ} is trained for each four-lepton final state separately which is found to improve the discriminating power. The BDT training for the 7 and 8 TeV analysis is performed using MC samples produced at $\sqrt{s}$ =7, 8 TeV, respectively.

Separated Hypotheses	N_{Trees}	Shrink.	MNP	S/B	BSF	N_{Cuts}	MaxDepth
$J^p = 0^+,\ 0^-$	200	0.10	0.5	1	0.6	20	3
$J^p = 0^+,\ 0^+_h$	800	0.03	0.6	1	0.8	20	3
$J^p = 0^+,\ 2^+$	200	0.10	0.5	1	0.6	20	3
SM Higgs, $ZZ^* \to 4e$	300	0.03	0.6	1.5	0.6	20	3
SM Higgs, $ZZ^* \to 4\mu$	900	0.05	0.6	1.5	0.6	20	5
SM Higgs, $ZZ^* \to 2e2\mu$	300	0.03	0.6	1.5	0.6	20	3
SM Higgs, $ZZ^* \to 2\mu 2e$	300	0.02	0.6	1.5	0.6	20	3

Table 7.1: Parameters used in the BDT training.

Each MC samples are separated at random into two subset of MC samples, one of them is used to train the BDT while the other subset to check if the BDT training process has picked up features caused by statistical fluctuations in MC instead of real physical features, which is referred to as overtraining hereafter. The BDT distributions obtained from the training and testing processes for the 8 TeV analysis are shown in Figure 7.3 for the spin and parity BDT and in Figure 7.4 for the BDT_{ZZ}. The integral of the receiver operating characteristic curve is computed for the distributions in training and testing to study the degree of overtraining. Differences of 1% or smaller in the integral are observed for all the BDTs, which indicate they are not overtrained. The BDTs for the 7 and 8 TeV analyses are found to be very similar indicating tiny dependence on the center-of-mass energy, hence, the BDTs for the 8 TeV analysis are used in the 13 TeV analysis where MC signal samples are not available.

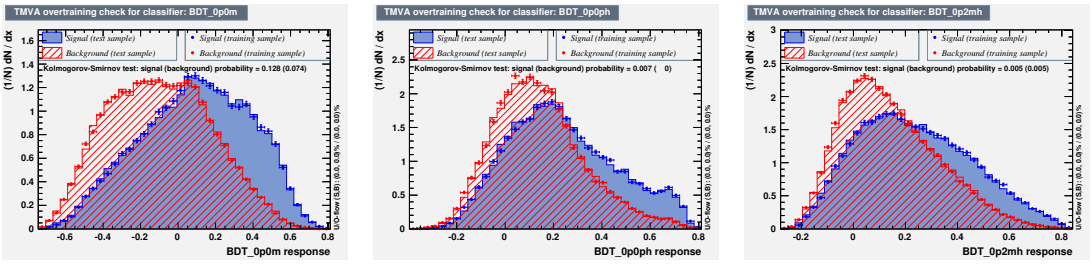

(a) (b) (c)

Figure 7.3: BDT discriminant distributions of MC samples for training and testing for the 8 TeV analysis for $J^p = 0^+$ vs. $J^p = 0^-$ (7.3a), $J^p = 0^+$ vs. $J^p = 0^+_h$ (7.3b), $J^p = 0^+$ vs. $J^p = 2^+$ with universal couplings separation (7.3c). The SM Higgs 0^+ hypothesis is labeled as signal while the BSM signal hypothesis is labeled as background process.

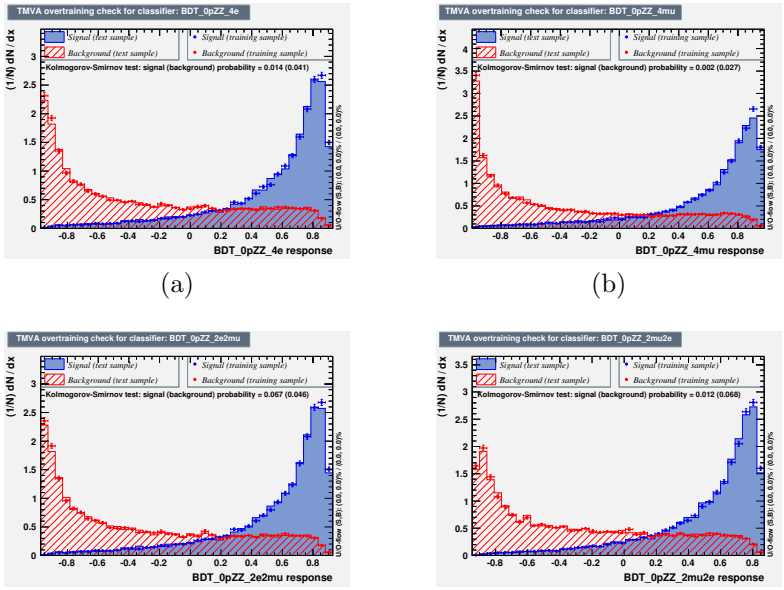

Figure 7.4: BDT discriminant distributions of MC samples for training and testing for the 8 TeV analysis for the $J^p = 0^+$ (labeled as signal) versus ZZ^*-continuum (labeled as background) separation in final state 4e (7.4a), 4μ (7.4b), 2e2μ (7.4c) and 2μ2e (7.4d).

7.2.3 Systematic Uncertainties

Source of the systematic uncertainty	Relative impact
Higgs boson mass experimental uncertainty	$\pm 2.8\%$
Muon momentum resolution	$\pm 0.8\%$
$Z + jets, t\bar{t}$ bkg contribution in $\ell\ell\mu\mu$ final state	$\pm 0.7\%$
e/γ resolution model (constant term)	$\pm 0.7\%$
ZZ^* pdf	$\pm 0.6\%$
$Z + jets, t\bar{t}$ bkg contribution in $\ell\ell ee$ final state	$\pm 0.6\%$
ZZ^* scale	$\pm 0.5\%$
e/γ resolution model (sampling term)	$\pm 0.5\%$
Luminosity	$\pm 0.5\%$

Table 7.2: Relative impact of the leading systematic uncertainties on the expected separation expressed in terms of numbers of standard deviations, between the SM $J^P = 0^+$ and the BSM $J^P = 0^-$ hypotheses.

Two general types of systematic effects impact the spin and parity study: uncertainties on discriminant shapes due to experimental effects, and uncertainties on background normalizations from theory uncertainties and data-driven background estimates. All sources of systematic uncertainty are first included in the analysis, the relative impact from each of the sources on the final separation significance is then evaluated, and finally sources affecting the final separation significance by less than $\pm 0.5\%$ are neglected. The sources of systematic uncertainty with no negligible impact on the separation between the SM $J^P = 0^+$ and $J^P = 0^-$ hypotheses are shown in Table 7.2, including experimental uncertainty on the measured Higgs boson mass of 500 MeV, the modeling of the irreducible ZZ^* background, the uncertainty on the integrated luminosity and the uncertainties on the electron and muon reconstruction. The Higgs boson mass uncertainty has the largest impact of about 2% due to the use of m_{4l} as an input variable to the BDT_{ZZ} discriminant. The total relative impact of all systematic uncertainties on the separation significance between the hypotheses is estimated to be about $\pm 5\%$.

7.2.4 Results in the Four-Lepton Channel

The observed and expected distributions of the BDT output score which are sensitive to separate SM Higgs from the tested BSM hypothesis, are shown in Figure 7.5. The data is found to be more compatible with the distribution of the BDT predicted by the SM Higgs boson than the BSM signal hypothesis in all cases. To illustrate the two-dimentional approach, the BDT_{ZZ} versus the spin and parity sensitive BDT discriminant plot for the $J^P = 0^+$ versus $J^P = 0^-$ hypothesis test are shown in Figure 7.6, including the data, SM $J^P = 0^+$ signal and the background process. The events populated towards the bottom region of the plot have a higher probability to be originated from background processes, while events populated in the top region of the plots are more signal-like.

The exclusion limit given by the observed value of the test statistic in the data and the sampling distribution from ensemble of MC pseudo experiments as shown in Figure 7.7 and 7.8. The quoted p-values is calculated as the integral the right tail of the test statistic distribution of the BSM hypothesis from the value of the test statistic in data. Table 7.3 summarizes the separation significance and p-values of the hypothesis test results based on the full Run 1 dataset collected in 2011 and 2012, Run 2 dataset collected in 2015 and 2016 corresponding to 36.1 fb^{-1} at 13 TeV, and their combination. In the combined result, all tested BSM hypotheses are rejected by about 4σ or more in favor of the SM Higgs hypothesis. For the SM Higgs boson

$J^P = 0^+$ versus the spin-2 with universal couplings hypothesis test, given the spin-2 hypothesis has been excluded by 3.2σ and 4.1σ based on the Run 1 and Run 2 data, respectively, it is expected that the exclusion significance combining Run 1 and Run 2 data should exceed 5σ. An exclusion significance of $> 4.3\sigma$ is quoted in Table 7.3 because the large number (about 10^7) of MC pseudo-experiments required and only a number of 2.4×10^5 MC pseudo-experiments have been generated due to the time limitation in generating the pseudo-experiments.

$\sqrt{s} = 7 + 8$ TeV

Tested Hypotheses	$p^{\text{BSM}}_{\text{exp},\mu=1}$	$p^{\text{BSM}}_{\text{obs}}$	$p^{\text{SM}}_{\text{obs}}$	$\sigma^{\text{BSM}}_{\text{exp},\mu=1}$	$\sigma^{\text{BSM}}_{\text{obs}}$
$0^+,\ 0^-$	0.001	0.012	0.78	3.10σ	2.26σ
$0^+,\ 0^+_h$	0.016	0.037	0.63	2.14σ	1.78σ
$0^+,\ 2^+(\ k_q = k_g)$	0.009	0.0007	0.23	2.36σ	3.2σ
$0^+,\ 2^+(\ k_q = 2k_g;\ p_{\text{T,H}} < 125$ GeV)	0.036	0.017	0.38	1.80σ	2.12σ
$0^+, 2^+(\ k_q = 2k_g;\ p_{\text{T,H}} < 300$ GeV)	0.018	0.0023	0.23	2.09σ	2.84σ
$0^+, 2^+(\ k_q = 0;\ p_{\text{T,H}} < 125$ GeV)	0.040	0.037	0.49	1.75σ	1.78σ
$0^+, 2^+(\ k_q = 0;\ p_{\text{T,H}} < 300$ GeV)	0.018	0.030	0.58	2.10σ	1.88σ

$\sqrt{s} = 13$ TeV

Tested Hypotheses	$p^{\text{BSM}}_{\text{obs}}$	$\sigma^{\text{BSM}}_{\text{obs}}$	$p^{\text{SM}}_{\text{obs}}$	$\sigma^{\text{BSM}}_{\text{exp},\mu=\hat{\mu}}$
$0^+,\ 0^-$	$1.8 \cdot 10^{-4}$	3.6σ	0.059	$> 4\sigma$
$0^+,\ 0^+_h$	$5 \cdot 10^{-5}$	3.9σ	0.48	3.9σ
$0^+,\ 2^+(\ k_q = k_g)$	$2 \cdot 10^{-5}$	4.1σ	0.58	4.1σ

$\sqrt{s} = 7 + 8 + 13$ TeV

Tested Hypotheses	$p^{\text{BSM}}_{\text{obs}}$	$\sigma^{\text{BSM}}_{\text{obs}}$	$p^{\text{SM}}_{\text{obs}}$	$\sigma^{\text{BSM}}_{\text{exp},\mu=\hat{\mu}}$
$0^+,\ 0^-$	$2.1 \cdot 10^{-5}$	4.1σ	0.049	$> 4.3\sigma$
$0^+,\ 0^+_h$	$7.1 \cdot 10^{-5}$	3.8σ	0.31	4.3σ
$0^+,\ 2^+(\ k_q = k_g)$	$< 8.3 \cdot 10^{-6}$	$> 4.3\sigma$	0.69	$> 4.3\sigma$

Table 7.3: Expected and observed p-value and the corresponding significance in spin and parity hypotheses tests.

7.3 Combined Studies of Spin and Parity in Diboson Decay Channels

7.3.1 Input Analyses and the Combined Model

To improve experimental sensitivity, analyses in the diboson channels are combined. The analysis in the $H \to \gamma\gamma$ channel is sensitive to the hypothesis test between the spin-2 hypotheses and the SM Higgs boson, while the analyses in the $H \to ZZ^*$ and $H \to WW^*$ channels are sensitive to separate both the spin-2 and the BSM spin-0 hypotheses from the SM Higgs boson. While combining the three analyses, the signal strength parameters for the different decay channels are kept independent in order not to introduce model dependency.

7.3.2 Results in Combining Diboson Channels

As summarized in Table 7.4, data favor the SM Higgs boson hypothesis and all tested BSM hypotheses are rejected at a more than 99.9% modified confidence level (CL_s) in favor of the SM hypothesis. Figure 7.10 includes representative plots showing the test statistic value observed in data and the expected distributions of the test statistics for the SM Higgs boson hypothesis and the BSM signal hypothesis.

Tested Hypothesis	$p^{\text{alt}}_{\text{exp},\mu=\hat{\mu}}$	$p^{\text{SM}}_{\text{obs}}$	$p^{\text{alt}}_{\text{obs}}$	Obs. CL_s (%)
0^+_h	$4.7 \cdot 10^{-3}$	0.85	$7.1 \cdot 10^{-5}$	$4.7 \cdot 10^{-2}$
0^-	$1.3 \cdot 10^{-4}$	0.88	$< 3.1 \cdot 10^{-5}$	$< 2.6 \cdot 10^{-2}$
$2^+(\kappa_q = \kappa_g)$	$2.9 \cdot 10^{-4}$	0.61	$4.3 \cdot 10^{-5}$	$1.1 \cdot 10^{-2}$
$2^+(\kappa_q = 0;\ p_{\text{T}} < 300\text{GeV})$	$< 3.1 \cdot 10^{-5}$	0.52	$< 3.1 \cdot 10^{-5}$	$< 6.5 \cdot 10^{-3}$
$2^+(\kappa_q = 0;\ p_{\text{T}} < 125\text{GeV})$	$3.9 \cdot 10^{-4}$	0.71	$4.3 \cdot 10^{-5}$	$1.5 \cdot 10^{-2}$
$2^+(\kappa_q = 2\kappa_g;\ p_{\text{T}} < 300\text{GeV})$	$< 3.1 \cdot 10^{-5}$	0.28	$< 3.1 \cdot 10^{-5}$	$< 4.3 \cdot 10^{-3}$
$2^+(\kappa_q = 2\kappa_g;\ p_{\text{T}} < 125\text{GeV})$	$1.2 \cdot 10^{-3}$	0.80	$7.3 \cdot 10^{-5}$	$3.7 \cdot 10^{-2}$

Table 7.4: Expected and observed p-values for different spin-parity hypotheses, for the combination of the three channels: $H \to \gamma\gamma$, $H \to ZZ^*$ and $H \to WW^*$. The observed CL_s for the non-SM hypothesis is reported in the last column.

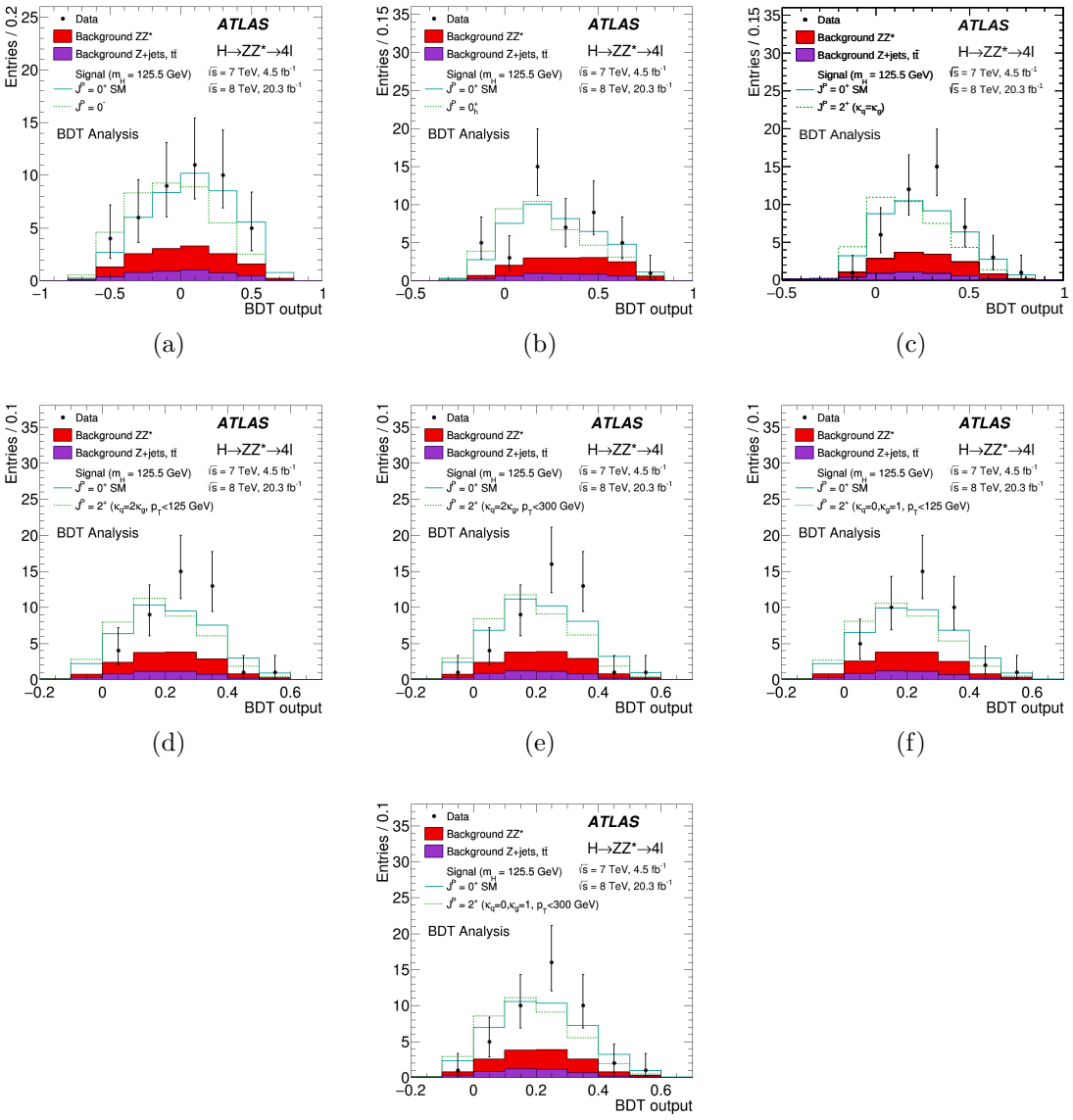

Figure 7.5: Distributions of the BDT discriminants in the signal region with data (points with errors), backgrounds (filled histograms), and for predictions for several spin and parity hypotheses. The Standard Model hypothesis is indicated with the solid line while the BSM hypotheses with dashed lines. The signal distributions are normalized to the signal strength observed in data.

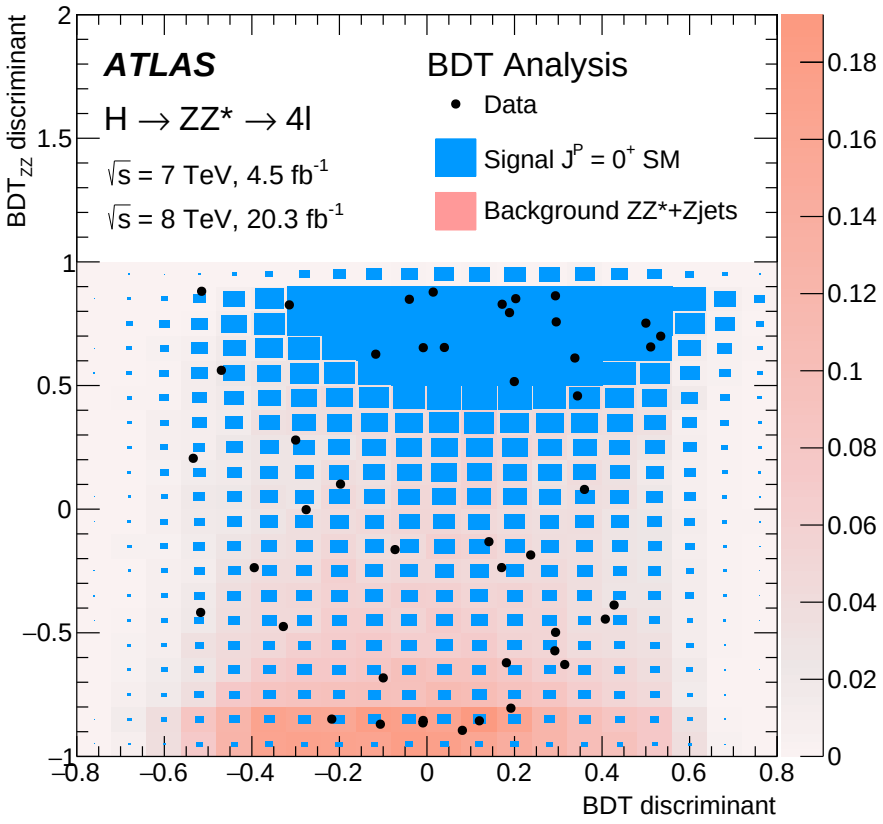

Figure 7.6: The distributions of the discriminant BDT_{ZZ} versus the BDT discriminant for the selected data candidates (points) compared to the SM signal ($J^P = 0^+$) (blue box) and the background proceses (orange box) in the signal region of 115 GeV $< m_{4\ell} <$ 130 GeV corresponding to 4.5 and 20.3 fb^{-1} collected at $\sqrt{s} = 7$ and 8 TeV.

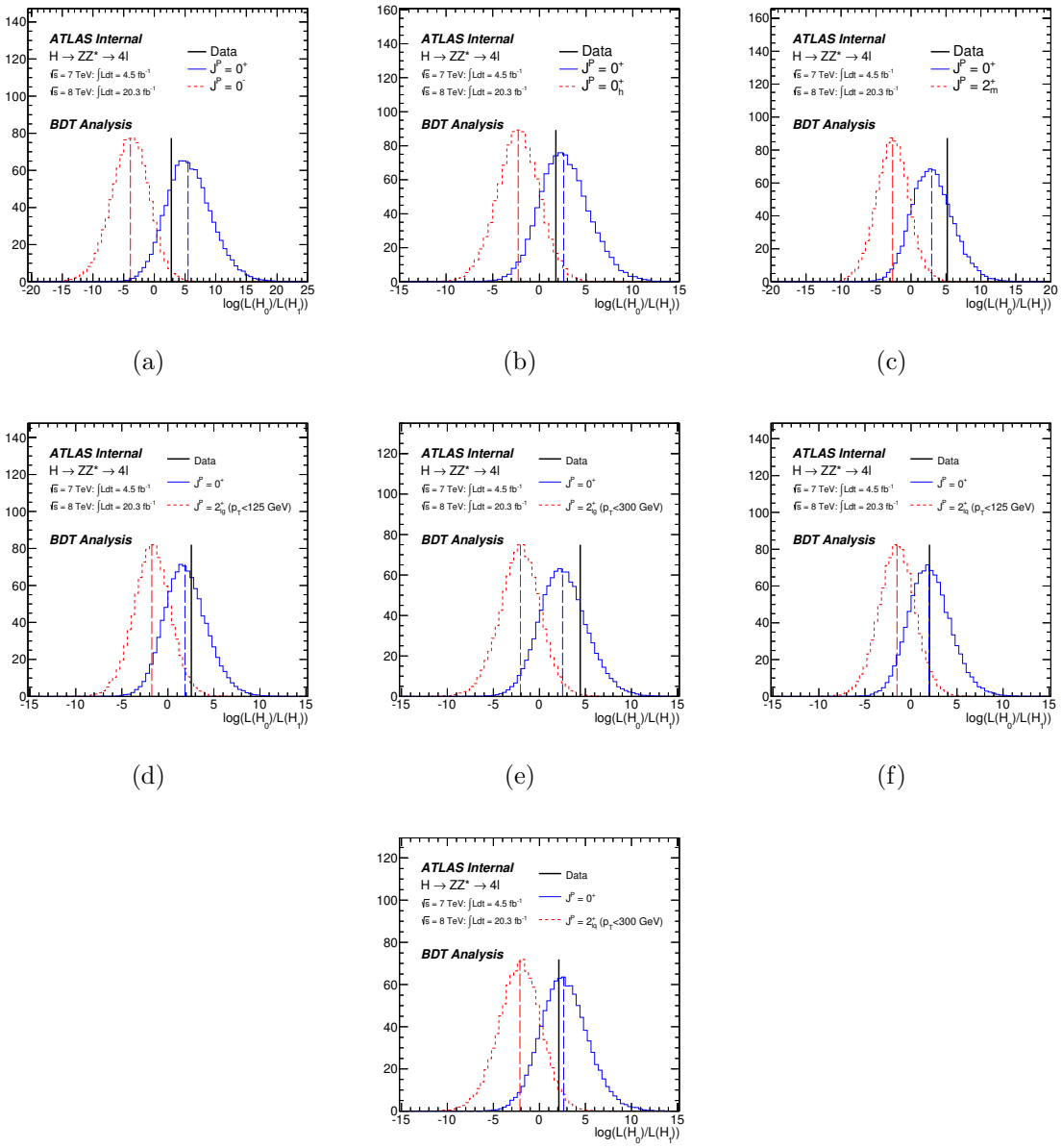

Figure 7.7: Distributions (histogram) of the test statistic given by ensemble of MC pseudo experiments for the two tested hypotheses, and the value (black line) observed in the data collected at $\sqrt{s} = 7$ and 8 TeV, for the hypothesis tests using the BDT output score as discriminant in the likelihood in the four-lepton channel: 0^+ SM versus 0^- (7.7a), 0^+ SM versus 0^+_h (7.7b), 0^+ SM versus 2^+ with universal couplings to fermions and bosons (7.7c), 0^+ SM versus 2^+ with low gluon fraction and $p_{\mathrm{T,H}} <$ 125 GeV (7.7d), 0^+ SM versus 2^+ with low gluon fraction and $p_{\mathrm{T,H}} < 300$ GeV (7.7e), 2^+ with low quark fraction and $p_{\mathrm{T,H}} < 125$ GeV (7.7f), and 0^+ SM versus 2^+ with low quark fraction and $p_{\mathrm{T,H}} < 300$ GeV (7.7g), respectively.

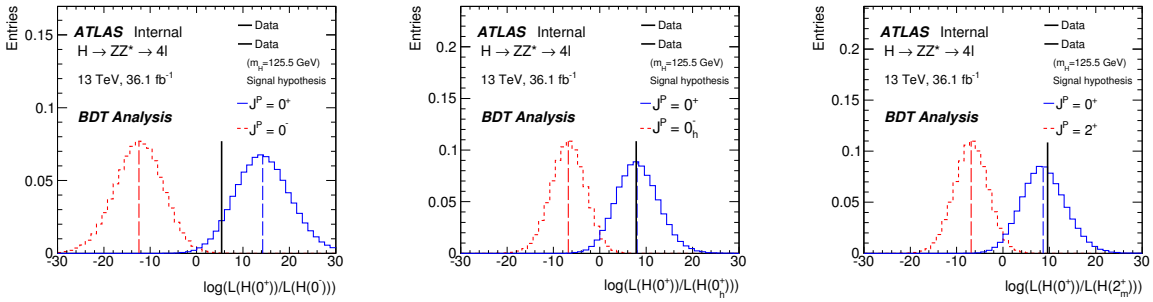

(a) (b) (c)

Figure 7.8: Distributions (histogram) of the test statistic given by ensemble of MC pseudo experiments for the two tested hypotheses, and the value (black line) observed in the data collected at $\sqrt{s} = 13$ TeV, for the hypothesis tests using the BDT output score as discriminant in the likelihood in the four-lepton channel: 0^+ SM versus 0^- (7.8a), 0^+ SM versus 0_h^+ (7.8b) and 0^+ SM versus 2^+ with universal couplings (7.8c).

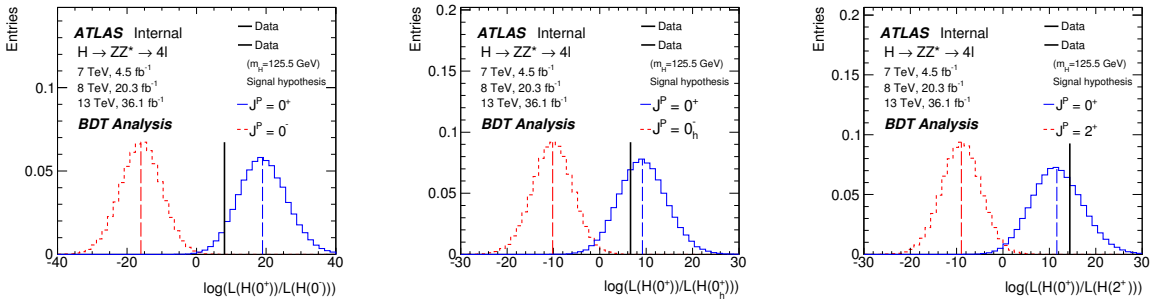

(a) (b) (c)

Figure 7.9: Distributions (histogram) of the test statistic given by ensemble of MC pseudo experiments for the two tested hypotheses, and the value (black line) observed in the data collected at $\sqrt{s} = 7$, 8, 13 TeV, for the hypothesis tests using the BDT output score as discriminant in the likelihood in the four-lepton channel:0^+ SM versus 0^- (7.8a), 0^+ SM versus 0_h^+ (7.8b) and 0^+ SM versus 2^+ with universal couplings (7.8c).

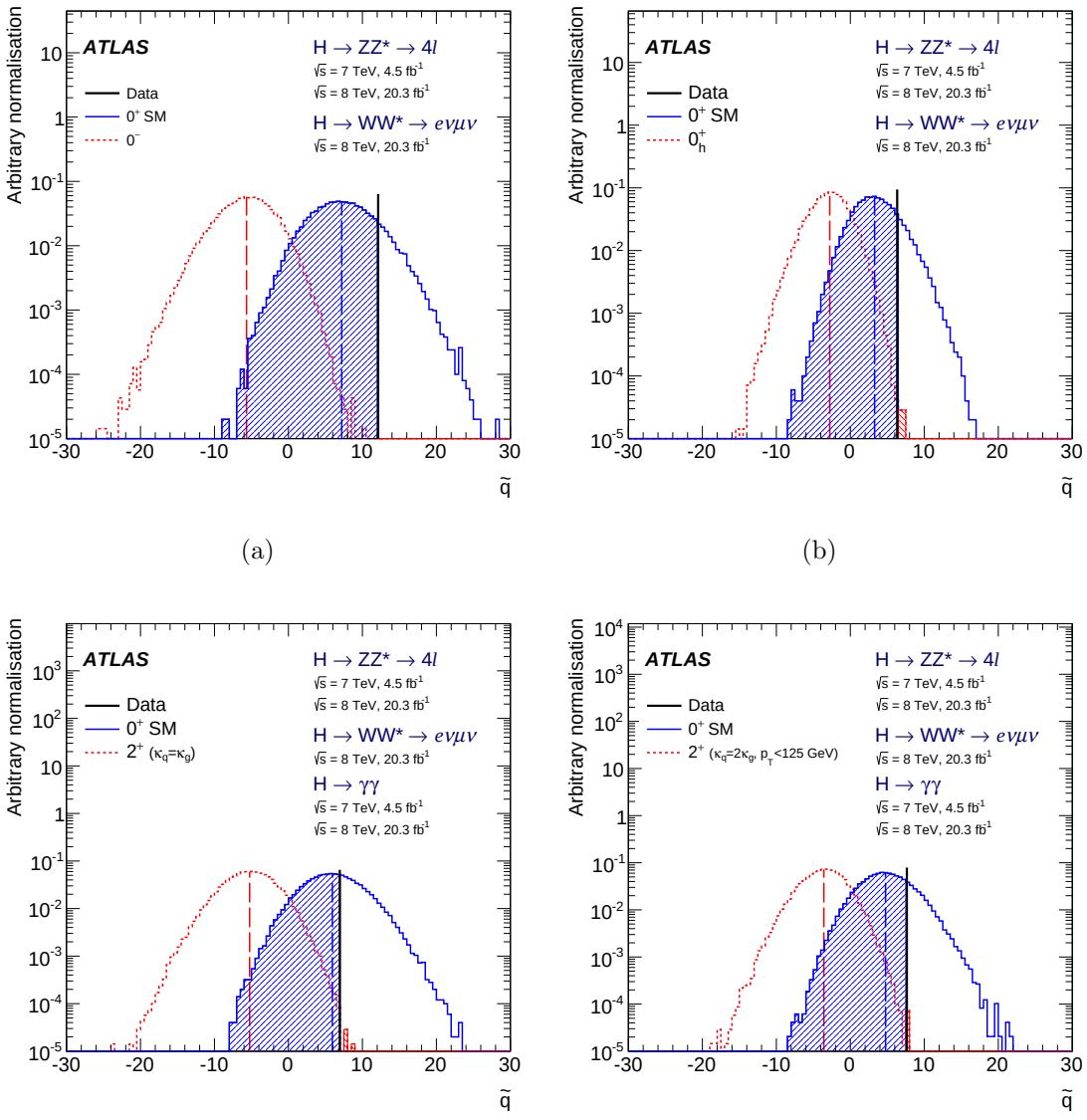

Figure 7.10: Representative distributions of the test statistic $\tilde{q}$ defined in Section 7.1.3, for the combination of the diboson decay channels. The observed values are indicated by the vertical solid line and the expected medians by the dashed lines. The shaded areas correspond to the integrals of the expected distributions used to compute the p-values for the rejection of each hypothesis.

CHAPTER VIII

Higgs Boson Couplings Measurement

In the SM, all coupling strengths of the Higgs boson to the SM vector boson and fermions can be precisely calculated once its mass is known. Thus, measuring the Higgs boson coupling strengths is a powerful approach to look for new physics beyond the SM from possible deviations in the measurement from the SM expectations. The Higgs boson coupling strengths can be probed in the Higgs boson production and decay vertices. Hence, measuring the Higgs boson production and decay rates is crucial for the Higgs boson coupling measurements. In order to be sensitive to different Higgs production mechanisms, several categories are designed. The $H \to ZZ^* \to 4\ell$ channel is the most sensitive Higgs decay channel to measure the Higgs boson coupling to the Z boson. In terms of production mechanisms, this channel is most sensitive to the ggF production mechanism. This chapter will discuss the Higgs boson coupling measurements in the $H \to ZZ^* \to 4\ell$ channel using data corresponding to an integrated luminosity of 36.1 fb^{-1} at $\sqrt{s} = 13$ TeV.

Based on the current statistical power in the LHC data, there is no single Higgs decay channel which is able to measure precisely all Higgs boson couplings, therefore, combining the measurements in multiple Higgs decay channels is crucial in making the best use of the statistical power in data to constrain the Higgs boson couplings. Measurements of the Higgs boson production and decay rates combining $H \to ZZ^* \to 4\ell$ and $H \to \gamma\gamma$ channels using data corresponding to an integrated luminosity of14.8 and 13.3 fb^{-1} at $\sqrt{s} = 13$ TeV is also reported in this chapter.

8.1 Measurement of Higgs Boson Production in Four-Lepton Decay Channel

8.1.1 Introduction

The Higgs boson production cross sections multiplied by the branching ratio to ZZ^* (denoted as $(\sigma \cdot B)_i^{ZZ}$), are measured in the $H \to ZZ^* \to 4\ell$ channel for several Higgs boson production mechanisms (i = ggF, VBF, VH and ttH), in the central region where the absolute value of the rapidity of the Higgs boson ($|y_H|$) is less than 2.5, which is defined in the stage-0 of the simplified template cross sections framework [36]. Adopting the phase space $|y_H| < 2.5$ in the $H \to ZZ^* \to 4\ell$ channel analysis is well-motivated as this analysis is not sensitive to the Higgs boson produced in the forward region. The signal acceptances in $\sigma_i(|y_H| < 2.5)$ phase space calculated using MC samples are shown in Table 8.1. These measurements are then interpreted

Process	$\sigma_i(\|y_H\| < 2.5)/\sigma_i$
ggF	0.912
VBF	0.930
WH	0.880
$q\bar{q} \to ZH$	0.891
ttH	0.983
bbH	0.944

Table 8.1: Ratios between $\sigma_i(|y_H| < 2.5)$ and the total cross section for each production process.

in terms of the signal strength parameters or Higgs boson couplings to other SM particles, taken into account additional relevant theoretical uncertainties associated with the SM predictions.

8.1.2 SM Higgs Boson Signal and Background Simulation

8.1.2.1 Signal Modeling

The SM Higgs boson productions via ggF, VBF and VH production mechanisms are modelled using the POWHEG-BOX v2 MC event generator [93, 94, 95] using the PDF4LHC NLO PDF set [96]. The ggF Higgs boson production process is calculated with the precision of NNLO in QCD, using the POWHEG method to merge the NLO Higgs plus jet cross section with the parton shower, and using the MiNLO

method [97] to reach NLO accuracy for the inclusive Higgs boson production. In addition, a reweighting method using the HNNLO program [98, 99] is used to achieve NNLO accuracy. VBF and VH production mechanisms are modelled at NLO in QCD. The MiNLO method is used to merge VH events plus zero and one jet [100]. The ttH and bbH production mechanisms are calculated with the precision of NLO in QCD using the MadGraph5_aMC@NLO [101] generator using the NNPDF23 and CT10nlo PDF set, respectively. The showering, hadronization and multiple partonic interactions are modelled using PYTHIA 8 [102] generator for the ggF, VBF, VH and bbH production mechanisms and using Herwig++ [103] generator for the ttH production mechanism. The inclusive Higgs boson production cross sections for the production mechanisms and decay branching fractions to the four sub-channels (4μ, $2\mu 2e$, $2e2\mu$ and $4e$) take the theory calculations provided by Ref. [36].

8.1.2.2 Background Modeling

The method to estimate the background follows the description in Section 5.5. This section presents the simulation of the MC samples used to model the ZZ^* background processes.

The ZZ^* continuum background from quark-antiquark annihilation is modelled using Sherpa 2.2 [104, 105, 106] generator using the NNPDF3.0nnlo PDF set, which is calculated at NLO for events with zero or one jet, and at LO for events with two or three jets. The NLO electroweak corrections are applied depending on the invariant mass of the four-lepton system [107, 108].

The electroweak ZZ^* production in association with two jets, vector boson scattering process (VBS), is modelled using Sherpa generator. The SM Higgs boson VBF production process is also included in the sample, which is extracted by a signal (VBF) plus background (VBS) fit to the sample, and then removed.

The gluon-initiated ZZ^* production is modelled by gg2VV [109] generator at LO in QCD. A k-factor of 1.7 with a conservative uncertainty of 60% is applied to account for higher order QCD effects for the $gg \to ZZ^*$ continuum production, which is calculated under the assumption of massless quark loops [110, 111] in the heavy top-quark approximation [112], [113].

8.1.3 Event Categorization

In order to be sensitive to the different Higgs boson production mechanisms, and one step further, to be sensitive to some of the truth bins defined in the stage-1 of the

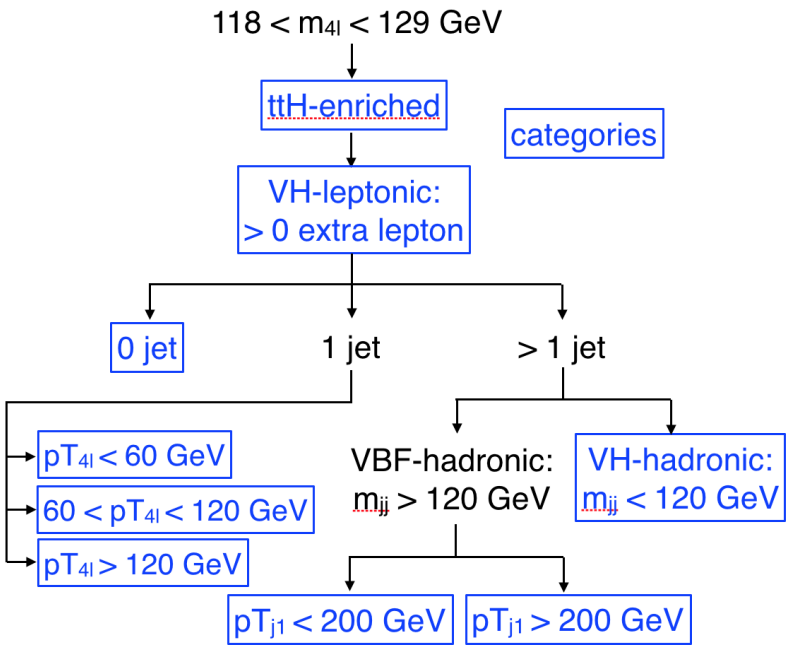

Figure 8.1: A flowchart illustrating the categorization scheme with the final categories shown in blue box.

simplified template cross sections framework [36], each $H \to ZZ^* \to 4\ell$ candidate having an invariant mass of the four-leptons system in the range of 118 GeV $< m_{4l} <$ 129 GeV and satisfying the event selection criteria which are described in 5.3, is classified into one of eight exclusive categories. Some of the categories are expected to be populated with at least a few events, and in such cases, discriminant observables are introduced to further improve the analysis sensitivity to the targeted production mechanism. The discriminant used are the output score of the BDTs trained on simulated samples to distinguish a particular SM Higgs boson production process from other SM Higgs boson production processes, or from the ZZ^* background process.

8.1.3.1 Event Categorization Scheme

The definition of the categories depends on event characteristics including the number of jets, b-tagged jets, and the presence of extra leptons, in addition to the four leptons identified as from the Higgs boson decays. The categories are shown in sequential order in Figure 8.1 and described in detail below.

With the highest priority, the ttH-enriched category requires the presence of at least one b-tagged jet with a b-jet selection efficiency of 70%. In addition, there must

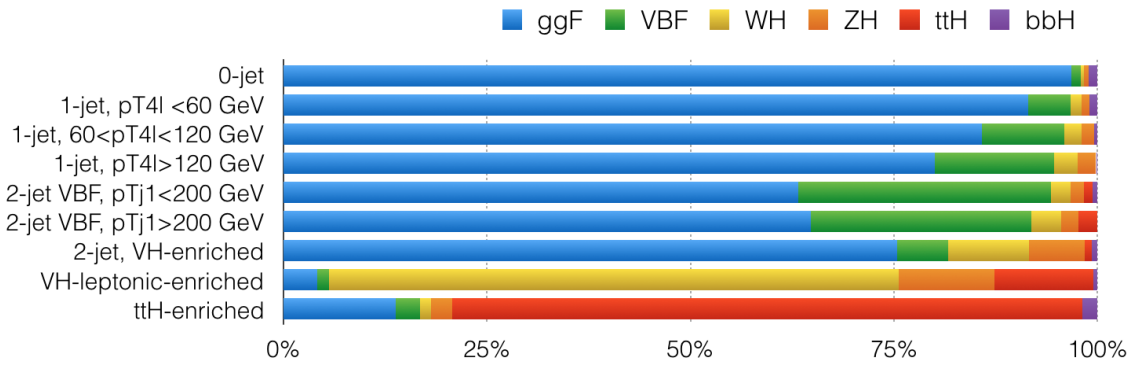

Figure 8.2: Signal composition in categories

be either at least four jets, or one additional lepton (e or μ) with transverse momentum larger than 12 GeV together with at least two jets. The events not satisfying the ttH-enriched category are considered for the VH-leptonic-enriched category, which is defined by the presence of an extra lepton with transverse momentum larger than 12 GeV.

Events that fail the VH-leptonic-enriched category criteria are then classified according to the jet multiplicity. The 0-jet category, expected to contain about 56% of the ggF events, is the most sensitive category in the measurement of the ggF production mechanism.

The 1-jet category is important for both ggF and VBF production mechanism measurements, which is expected to contain about 29% of the ggF events and 34% of the VBF events. Motivated by the stage-1 of the simplified template cross sections framework, the 1-jet category is further divided into three categories with the transverse momentum of the four-lepton system being smaller than 60 GeV, between 60 to 120 GeV and larger than 120 GeV, mirroring the corresponding truth bin definition.

Events with two or more jets are split into two categories depending on the dijet invariant mass. If more than two jets are present in the event, the two jets with higher p_{T} are considered. They are called as the leading and subleading jets. Events with dijet invariant mass in the range of 40 GeV $< m_{\mathrm{jj}} <$ 120 GeV are assigned to the VH-hadronic-enriched category. The rest of the events are further split into two VBF-enriched categories by requiring the leading jet p_{T} to be smaller or larger than 200 GeV, mirroring the corresponding truth bin definition in the stage-1 of the simplified template cross sections framework. Figure 8.2 shows the signal composition expected in the SM in each category.

8.1.3.2 ttH-enriched Category

Studying the ttH production mechanism is essential to directly probe the Yukawa coupling between the Higgs boson and the top quark, the heaviest particle in the SM. Due to its very small cross section, which is about 1% of the SM Higgs boson total production cross section, the ttH production mechanism is difficult to probe. Both ATLAS and CMS experiments have been searching for this production mechanism in several Higgs decay channels [114, 115, 116]. Up to now, the ttH production mechanism has not yet been observed. In spite of the small branching ratio of the $H \to ZZ^* \to 4\ell$ channel, the clean final state and excellent signal-over-background ratio make it very interesting to probe the ttH production mechanism using this Higgs decay channel.

The topology of events produced via the ttH production mechanism is characterized by the presence of b-jets, high jet multiplicity in case of hadronic decay of a W boson coming from the top quark decay and the presence of an additional lepton in case of a W boson decays leptonicly. Since this topology is quite distinct from other production mechanisms probed in this analysis (ggF, VBF, VH), a dedicated category is designed to enrich in ttH events and is given the highest priority in the event categorization scheme.

The strategy of designing the ttH-enriched category is to use simple selection criteria to allow good ttH signal efficiency while suppress backgrounds, given the expected ttH signal is very small: only 0.45 events are expected in the analysis signal region for a dataset corresponding to an integrated luminosity of 36.1 fb^{-1} at $\sqrt{s} = 13$ TeV. Two types of events with the presence of at least one b-tagged jets identified by the 70% b-tagging WP are considered: one associated with an additional lepton (ttH-leptonic) and the other one with high jet multiplicity, number of jets bigger than three $N_{jet} > 3$ (ttH-hadronic). They are merged into one category due to the very limited number of ttH events expected to be observed in data. $N_{jet} > 3$ selection is chosen as study showed that the ttH sensitivity would be less if requiring at least two or at least four jets. The N_{jets} distribution for various processes is illustrated in Figure 8.3 before the b-tagging selection.

The identification of b-jets is crucial in the search for the ttH production mechanism. The number of b-jets (N_{b-jets}) distribution for various processes are presented in Figure 8.4 for the 60%, 70%, 77% and 85% WPs.

Studies have been performed to optimize the ttH category selection. Table 8.2 and 8.3 presented cutflows for several tested selection criteria, and the selection:

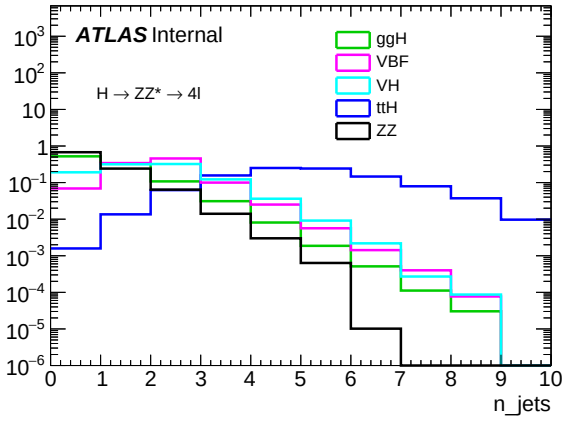

Figure 8.3: The number of jets (N_{jet}) distribution for various processes.

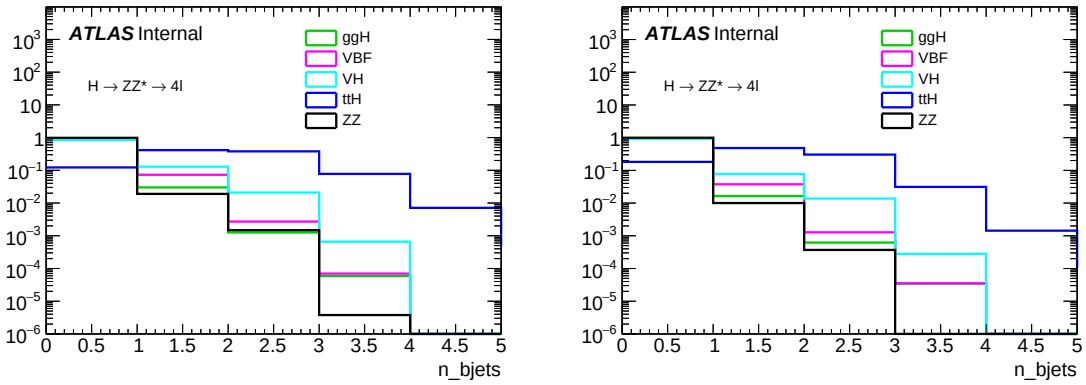

(a)

(b)

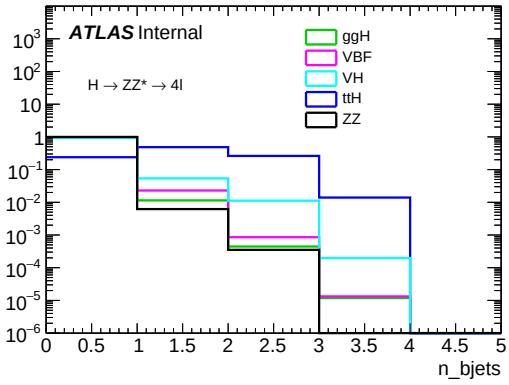

(c)

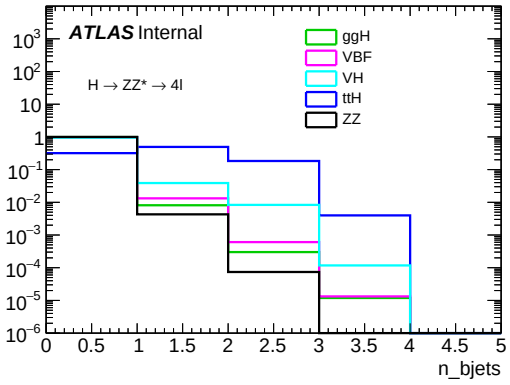

(d)

Figure 8.4: The number of b-jets (N_{b-jet}) distribution for various processes for b-tagging 85% WP (8.4a), 77% WP (8.4b), 70% WP (8.4c), and 60% WP (8.4d).

B-tagging	selection	N_{ttH}	ttH efficiency	Bkg	S/B	ttH significance
85% WP	$N_{b-jet} > 0$	0.40	0.88	2.70	0.15	0.24
	$N_{jet} > 3$	0.32	0.70	0.18	1.79	0.62
	$p_{\mathrm{T(j1)}} > 50$ GeV,	0.32	0.69	0.16	1.96	0.64
	$p_{\mathrm{T(j2)}} > 40$ GeV					
77% WP	$N_{b-jet} > 0$	0.37	0.82	1.47	0.25	0.30
	$N_{jet} > 3$	0.30	0.65	0.11	2.72	0.69
	$p_{\mathrm{T(j1)}} > 50$ GeV,	0.29	0.64	0.10	3.02	0.71
	$p_{\mathrm{T(j2)}} > 40$ GeV					
70% WP	$N_{b-jet} > 0$	0.35	0.76	1.01	0.35	0.33
	$N_{jet} > 3$	0.28	0.61	0.08	3.51	0.72
	$p_{\mathrm{T(j1)}} > 50$ GeV,	0.28	0.60	0.07	3.93	0.74
	$p_{\mathrm{T(j2)}} > 40$ GeV					
60% WP	$N_{b-jet} > 0$	0.31	0.68	0.70	0.45	0.35
	$N_{jet} > 3$	0.25	0.55	0.06	4.16	0.72
	$p_{\mathrm{T(j1)}} > 50$ GeV,	0.25	0.54	0.05	4.69	0.74
	$p_{\mathrm{T(j2)}} > 40$ GeV					

Table 8.2: ttH-hadronic enriched category selection optimization. The cutflow are presented for the four b-tagging working points. The last step of jet p_{T} requirement is not applied to synchronize with VBF and VH-hadronic categories with negligible lose in the sensitivity.

B-tagging	selection	N_{ttH}	ttH efficiency	Bkg	S/B	ttH significance
85% WP	$N_{b-jet} > 0$	0.40	0.88	2.70	0.15	0.24
	$N_l > 4$	0.11	0.23	0.014	7.4	0.55
	$p_{T,l_1} > 12$ GeV	0.096	0.21	0.009	11	0.58
	$N_{jet} > 1$	0.095	0.21	0.003	39	0.69
	$p_{\mathrm{T(j1)}} > 50$ GeV	0.093	0.20	0.003	32	0.70
77% WP	$N_{b-jet} > 0$	0.37	0.82	1.47	0.25	0.30
	$N_l > 4$	0.10	0.22	0.01	11	0.59
	$p_{T,l_1} > 12$ GeV	0.091	0.20	0.005	20	0.63
	$N_{jet} > 1$	0.089	0.19	0.002	45	0.72
	$p_{\mathrm{T(j1)}} > 50$ GeV	0.087	0.19	0.002	52	0.73

Table 8.3: ttH-leptonic enriched category selection optimization. The cutflow are presented for two b-tagging working points.

- ttH-hadronic: 70% WP, $N_{b-jet} > 0$, $n_{jet} > 3$
- ttH-leptonic: 85% WP, $N_{b-jet} > 0$, $n_{jet} > 1$, presence of an additional lepton.

is found to have the best ttH sensitivity among all the tested scenarios. Furthermore, four selection criteria Selection A-D are tested to finalize which b-tagging WP and what threshold for the p_{T} selection of the additional lepton to use:

Selection A:

- ttH-hadronic: 70% WP, $N_{b-jet} > 0$, $N_{jet} > 3$
- ttH-leptonic: 85% WP, $N_{b-jet} > 0$, $N_{jet} > 1$, presence of an additional lepton with $p_{\mathrm{T}} > 12$ GeV.

Selection B:

- ttH-hadronic: 70% WP, $N_{b-jet} > 0$, $N_{jet} > 3$
- ttH-leptonic: 85% WP, $N_{b-jet} > 0$, $N_{jet} > 1$, presence of an additional lepton with $p_{\mathrm{T}} > 8$ GeV.

Selection C:

- ttH-hadronic: 70% WP, $N_{b-jet} > 0$, $N_{jet} > 4$
- ttH-leptonic: 85% WP, $N_{b-jet} > 0$, $N_{jet} > 1$, presence of an additional lepton with $p_{\mathrm{T}} > 12$ GeV.

Selection D:

- ttH-hadronic: 70% WP, $N_{b-jet} > 0$, $N_{jet} > 3$
- ttH-leptonic: 70% WP, $N_{b-jet} > 0$, $N_{jet} > 1$, presence of an additional lepton $p_{\mathrm{T}} > 12$ GeV.

Selection D in which only 70% WP is used, is chosen as the final selection for the ttH-category, in order to simplify the b-tagging systematic uncertainties, with a tiny lose in the expected ttH (1%) and VH (3%) sensitivity, as shown in Figure 8.5 and Table 8.5.

Selection	μ_{ttH} 95% CL	ttH significance	μ_{VH} 95% CL	VH significance
Selection A	[-1.21,3.26]	0.694σ	[-1.16,2.17]	0.791σ
Selection B	[-1.21,3.25]	0.695σ	[-1.20,2.17]	0.758σ
Selection C	[-1.04,3.52]	0.862σ	[-1.17,2.17]	0.787σ
Selection D	[-1.22,3.34]	0.677σ	[-1.21,2.18]	0.759σ

Table 8.4: Sensitivity for the affected production mechanisms ttH and VH, with four selection criteria for the ttH-enriched category, checking the impact of lepton p_{T} requirements changing from 8 GeV to 12 GeV, b-tagging WP from 85% to 70% efficiency in the ttH-leptonic part of the selection.

Looking forward, more data to come will allow the inclusion of two such categories separately, motivated by the much higher purity of ttH events in the ttH-leptonic than in the ttH-hadronic category. Besides, multivariate technique can potentially improve the sensitivity when there are more data.

8.1.3.3 VH-Leptonic Category

The p_{T} threshold for the additional lepton is raised to 12 GeV from 8 GeV in this analysis from the previous analysis [117], which provides about 4% gain in VH signal significance. Figure 8.6 shows the p_{T} distribution of the additional lepton with p_{T} bigger than 8 GeV.

8.1.3.4 Discriminants in 1-jet Categories

Approximately 34% of VBF events are expected to have only one reconstructed jet, therefore, a discriminant is introduced in this category to separate VBF events

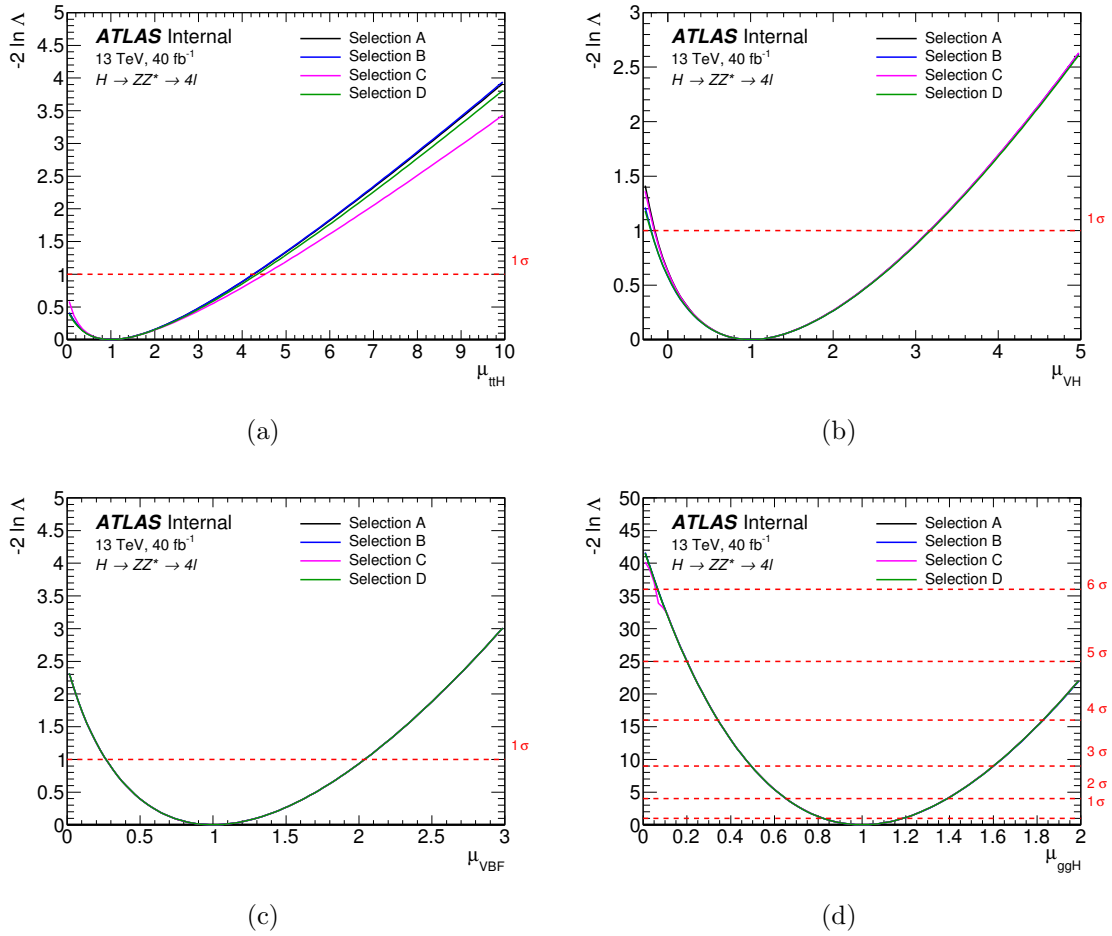

(a) (b)

(c) (d)

Figure 8.5: NLL scans for the expected sensitivity for 36.1 fb^{-1} at 13 TeV for the ttH (8.5a), VH (8.5b), VBF (8.5c) and ggF (8.5d) production mechanisms, under the four selection criteria for the ttH-enriched category, studying the impact of lepton p_{T} requirements changing from 8 GeV (blue line) to 12 GeV (black line) for both VH and VH-leptonic category, b-tagging WP from 85% (black line) to 70% (blue line) efficiency in the ttH-leptonic part of the selection, number of jet selection comparing $n_{jet} > 3$ (black line) and $n_{jet} > 4$ (magenta line).

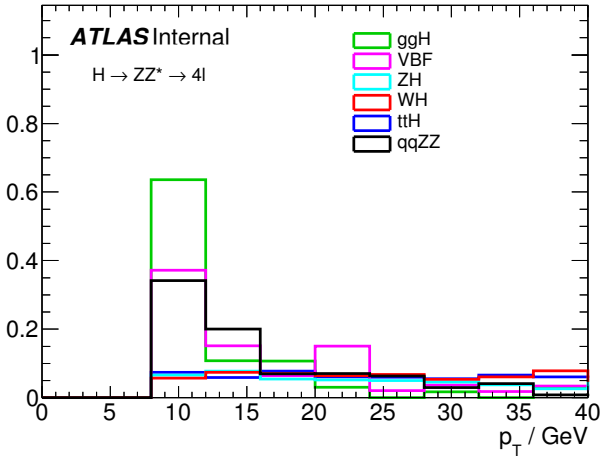

Figure 8.6: p_{T} distribution of the additional lepton starting from 8 GeV

from other processes. For the 1-jet $p_{\mathrm{T,H}} < 60$ GeV and 60 GeV $< p_{\mathrm{T,H}} < 120$ GeV categories, a BDT discriminant is trained on ggF and VBF MC samples, which is found to be sensitive to separate events produced via the VBF process from all other processes. The training is performed using the transverse momentum ($p_{\mathrm{T(j1)}}$) and pseudorapidity ($\eta_{\mathrm{(j1)}}$) of the jet, as well as the $\Delta R(j, 4\ell)$ variable which measures the angular separation between the reconstructed jet and the four-lepton system. The ranking of the variables according to their importance to the BDT discriminant is $\eta_{\mathrm{(j1)}}$, $p_{\mathrm{T(j1)}}$, and $\Delta R(j, 4\ell)$. The distribution of these variables for the VBF and ggF events are shown in Figure 8.7.

Training and testing samples are randomly and evenly drawn from MC events simulated assuming $m_H = 125$ GeV. The gradient boosted decision tree technique is used to perform the training, and the training configurations are listed in Table 8.5. Superimpositions of the BDT response of the training and testing samples for the

Category	$\mathrm{N_{Trees}}$	Shrink.	S/B	BSF	N_{Cuts}	MaxDepth
1-jet, $p_{\mathrm{T,H}} < 60$ GeV	400	0.03	1	0.5	20	3
1-jet, 60 GeV $< p_{\mathrm{T,H}} < 120$ GeV	150	0.06	1	0.5	20	3

Table 8.5: Table of parameters used for the BDT training in the 1-jet categories. The parameters are described in Section 7.2.2.

$p_{\mathrm{T,H}} < 60$ GeV and 60 $<$ GeV$p_{\mathrm{T,H}} < 120$ GeV 1-jet categories, are shown in Figure 8.8, indicating good agreement between the testing and training process and thus the BDTs are not overtrained.

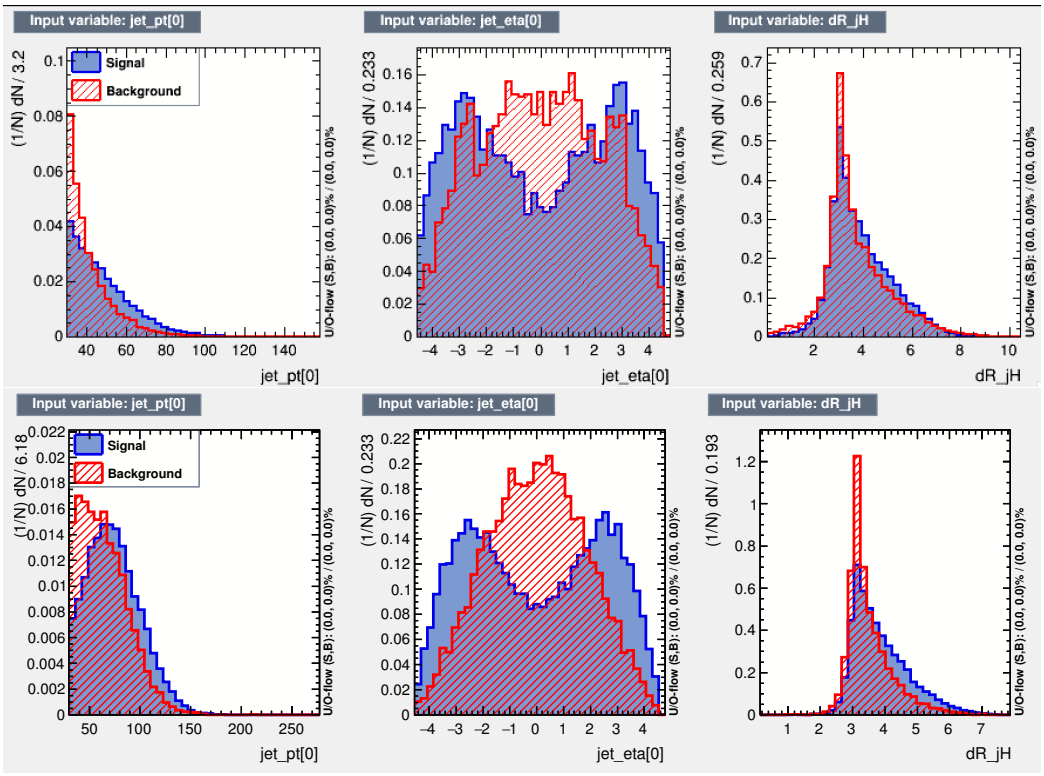

Figure 8.7: Discriminating variables considered for training the BDT for the 1-jet $p_{\mathrm{T,H}} < 60$ GeV (top) and $60 < p_{\mathrm{T,H}} < 120$ GeV (bottom) categories, from left to right, jet p_{T}, jet η, $\Delta R(j, 4\ell)$. The VBF MC events are labeled as signal shown in blue while the ggF MC events are labeled as background in red.

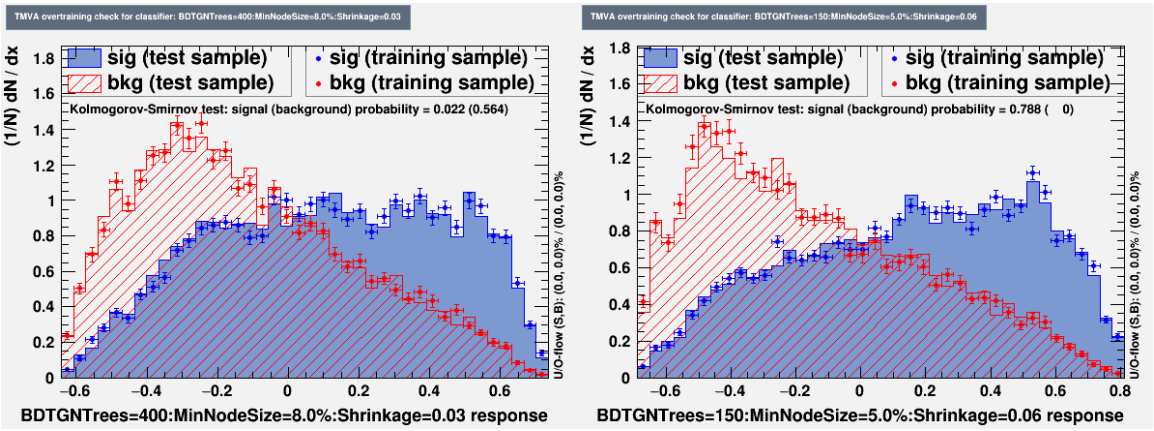

(a) (b)

Figure 8.8: Superimposed training and testing samples for the BDT to separate ggF and VBF events in the 1-jet $p_{\mathrm{T,H}} < 60$ GeV (8.8a) and 60 GeV $< p_{\mathrm{T,H}} < 120$ GeV (8.8b) categories. The VBF MC events are labeled as signal shown in blue while the ggF MC events are labeled as background in red. The distributions shown by points represent training samples, while the distributions shown by filled histograms come from testing samples.

8.1.3.5 Other Discriminants

The BDT discriminant in the 0-jet category (BDT_{ZZ^*}) separates the Higgs boson signal from the ZZ^* background, which is trained on the transverse momentum ($p_T^{4\ell}$) and pseudorapidity ($\eta_{4\ell}$) of the four-lepton system, as well as a matrix-element based kinematic discriminant D_{ZZ^*} as defined in Equation 7.4.

In the 2-jet VBF-enriched category with leading jet p_{T} smaller than 200 GeV, several input variables are used to separate events produced in the VBF and ggH mechanism: the invariant mass (m_{jj}), pseudorapidity separation ($\Delta\eta_{jj}$) and transverse momentum of the leading and subleading jet (p_{T}^{j1}, p_{T}^{j2}), the transverse momentum of the four-lepton plus di-jets system ($p_{\mathrm{T}}^{4\ell jj}$), the difference between the pseudorapidity of the four-lepton system and the average pseudorapidity of the leading and subleading jet (η_{ZZ^*}), as well as the minimum angular separation between the leading dilepton pair and the leading and subleading jets ($\Delta R(j, 4\ell)$).

In the VH-hadronic-enriched category, same input variables as in the 2-jet VBF category is used with the exception of replacing $p_{\mathrm{T}}^{4\ell jj}$ with the pseudorapidity of the leading jet (η_{j1}).

To summarize, all categories and discriminant observables are shown in Table 8.6.

Category	Discriminant	BDT training variables
0-jet	BDT_{ZZ}	$p_T^{4\ell}$, $\eta_{4\ell}$, D_{ZZ^*}
1-jet, $p_{\mathrm{T,H}} < 60$ GeV	BDT_{1jVBF}	p_T^j, η_j, $\Delta R(j, 4\ell)$
1-jet, 60 GeV $< p_{\mathrm{T,H}} < 120$ GeV	BDT_{1jVBF}	p_T^j, η_j, $\Delta R(j, 4\ell)$
1-jet, $p_{\mathrm{T,H}} > 120$ GeV	counting	
2-jet, VBF $p_{\mathrm{T(j1)}} < 200$ GeV	BDT_{2jVBF}	m_{jj}, $\Delta\eta_{jj}$, p_{T}^{j1}, p_{T}^{j2}, $\eta_{4\ell}$ ΔR_{jZ}^{min}, $p_{\mathrm{T}}^{4\ell jj}$
2-jet, VBF $p_{\mathrm{T(j1)}} > 200$ GeV	counting	
2-jet, VH-hadronic-enriched	BDT_{2jVH}	m_{jj}, $\Delta\eta_{jj}$, p_{T}^{j1}, p_{T}^{j2}, $\eta_{4\ell}$ ΔR_{jZ}^{min}, η_{j1}
VH-leptonic-enriched	counting	
ttH-enriched	counting	

Table 8.6: List of categories and BDT discriminants with the variables used in the training.

8.1.4 Systematic Uncertainties

The dominating theory uncertainties includes inclusive cross sections, and the modelling of the event topology, for signal and background processes. The main experimental uncertainties arise from the jet and lepton reconstruction and identification efficiencies and the jet energy scale, uncertainty on the measurement of data integrated luminosity, as well as the uncertainties on the data-driven background estimates.

8.1.4.1 Theoretical uncertainties

The main theoretical uncertainty on the signal for the cross section measurement is the modelling of the ggF signal events in different jet multiplicity bins, and in different $p_{\mathrm{T,H}}$ bins. The size of the migration between jet bins varies from a few percent to 15% level, and correlations of the migrations between categories are taken into account. In addition, the uncertainty from $p_{\mathrm{T,H}}$ or p_T^{j1} splitting in the 1-jet and 2-jet categories affects the signal yields by 20% to 40%. The uncertainty on the shape of BDT discriminants for the ggF process in the 2-jet categories is included as well. Other signal processes have smaller uncertainties from QCD scale variation. For all signal process, the PDF uncertainties on the signal acceptances are also taken into account.

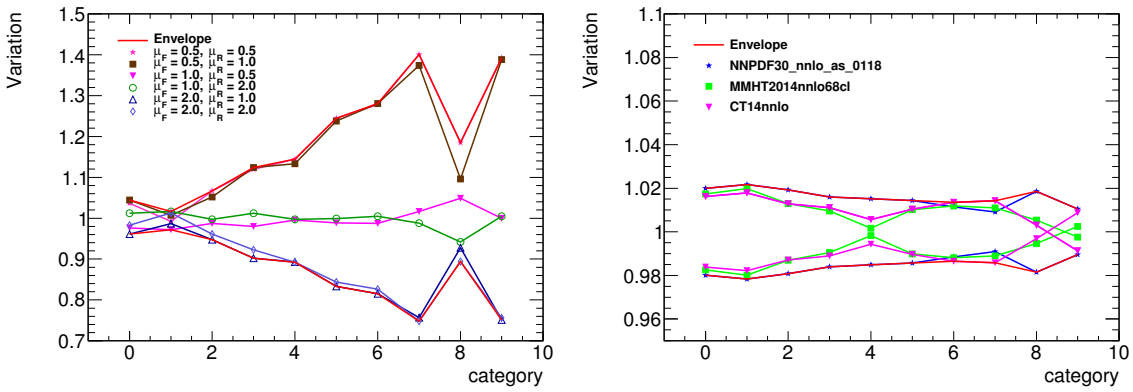

(a) (b)

Figure 8.9: PDF (8.9a) and PDF (8.9b) variations on the $qqZZ$ background process for the expected event yield inclusively shown in index 0, and on the categories shown in index $1-9$ are 0-jet, 1-jet $p_{\mathrm{T,H}} < 60$ GeV, 1-jet 60 GeV $< p_{\mathrm{T,H}} < 120$ GeV, 1-jet $p_{\mathrm{T,H}} > 120$ GeV, 2-jet VH-enriched, 2-jet VBF-enriched $p_{\mathrm{T(j1)}} < 200$ GeV, 2-jet VBF-enriched $p_{\mathrm{T(j1)}} > 200$ GeV, VH-leptonic-enriched, and ttH-enriched categories, respectively.

The theory uncertainties on the inclusive cross sections of the considered production mechanisms affect the signal-strength parameter and coupling measurements, and are thus included in the measurement.

For the ZZ^* background, the uncertainties coming from QCD scale and pdf are evaluated for both their effect on the expected number of events in the categories and on the expected distributions of the BDT discriminants. The QCD scale uncertainties are evaluated by independently varying the factorization and normalization scale by a factor of two and taking the largest variation. The pdf uncertainties are taken to be the maximum variations from the NNPDFnnlo 3.0 uncertainty evaluated using eigenvectors, and the difference comparing to two alternative PDF sets, CT14nnlo and MMHT2014nnlo68cl. These uncertainties on the inclusive event yield and each category are presented in Figure 8.9. The QCD uncertainty is about 3% for the inclusive event yield, and the pdf uncertainty is about 2%. The QCD uncertainty increases with the number of jets in the event. The impacts from QCD scale and pdf uncertainties on the BDT distribution is quite small, only at $1-2\%$ level.

8.1.5 Statistical Modeling

The statistical treatment of the data follows the likelihood method discussed in VI. Confidence intervals are based on the profile likelihood ratio test statistic. Depending on the measurements performed, the set of parameters of interest can be the Higgs boson production cross section in the central region ($\sigma_i(|y_H| < 2.5)$) times the branching ratio to ZZ^* ($(\sigma \cdot B)_i^{ZZ} = \sigma_i(|y_H| < 2.5) \times \mathrm{BR}_{ZZ^*}$), the signal strength parameters, or couplings modifiers.

8.1.6 Results

8.1.6.1 Expected and Observed Events in Categories

The numbers of expected and observed events are shown in Table 8.7 for each of the categories. In the two VBF-enriched categories, the observed number of events is slightly higher than that from SM expectation, leading to the measured $(\sigma \cdot B)_{\mathrm{VBF}}^{ZZ}$ slightly higher than its SM prediction. There are no events observed in the VH-leptonic and ttH-enriched categories, which is consistent with the SM prediction. The expected and observed distributions of BDT discriminants introduced in Section 8.1.3.1 are shown in Figure 8.10.

8.1.6.2 Production Cross Section Multiplied by Branching Ratio

The expected and measured $(\sigma \cdot B)_i^{ZZ}$ for each production processe i is shown in Table 8.8. Since there are no data observed in the ttH-enriched and VH-leptonic-enriched categories, and the three events in the VH-hadronic-enriched categories all have negative VH-sensitive BDT output scores (background- or ggF-like), the current data do not have contraint power for the VH and ttH production mechanisms yet. Therefore, $(\sigma \cdot B)_{\mathrm{VH}}^{ZZ}$ and $(\sigma \cdot B)_{ttH}^{ZZ}$ are free parameters but contrained to be positive when performing the measurements. The ggF and bbH processes are combined in the measurement ($(\sigma \cdot B)_{\mathrm{ggF+bbH}}^{\mathrm{ZZ}}$) because the analysis is not expected to be sensitive to the bbH production mechanism. The confidence intervals quoted are at 86.3% level, which are given by the two $(\sigma \cdot B)_i^{ZZ}$ values where the NLL scan curve and the line $-2\ln\Lambda = 1$ cross as shown in Figure 8.11.

All measured results are in very good agreement with the SM prediction, except that a tension of 2.1σ is observed with respect to the SM expectation in terms of the measured VBF production cross section multiplied by Higgs boson branching ratio to a pair of Z bosons ($(\sigma \cdot B)_{\mathrm{VBF}}^{ZZ}$), which is driven by the slightly higher number of events

Analysis	Signal			
category	ggF + bbH	VBF	VH	ttH
0-jet	26.2 ± 1.9	0.29 ± 0.08	0.25 ± 0.02	$(2.5 \pm 1.6) \cdot 10^{-4}$
1-jet $p_{\mathrm{T,H}}$ <60 GeV	8.1 ± 0.9	0.51 ± 0.03	0.23 ± 0.02	$(6.8 \pm 3.0) \cdot 10^{-4}$
1-jet 60 GeV< $p_{\mathrm{T,H}}$ < 120 GeV	4.5 ± 0.7	0.64 ± 0.08	0.23 ± 0.02	$(1.0 \pm 0.4) \cdot 10^{-3}$
1-jet $p_{\mathrm{T,H}} > 120$ GeV	1.11 ± 0.22	0.27 ± 0.04	0.095 ± 0.004	$(0.8 \pm 0.1) \cdot 10^{-3}$
2-jet VH-enriched	2.8 ± 0.5	0.21 ± 0.03	0.580 ± 0.031	0.031 ± 0.004
2-jet VBF-enriched $p_{\mathrm{T(j1)}} < 200$ GeV	3.9 ± 0.7	2.00 ± 0.15	0.285 ± 0.018	0.065 ± 0.007
2-jet VBF-enriched $p_{\mathrm{T(j1)}} > 200$ GeV	0.33 ± 0.09	0.18 ± 0.02	0.050 ± 0.003	0.016 ± 0.002
VH-leptonic-enriched	0.014 ± 0.002	0.003 ± 0.001	0.263 ± 0.016	0.038 ± 0.004
ttH-enriched	0.056 ± 0.013	0.009 ± 0.005	0.020 ± 0.002	0.301 ± 0.029
Total	47.0 ± 3.3	4.11 ± 0.18	2.00 ± 0.11	0.45 ± 0.04
Analysis	Background		Total	
category	ZZ^*	Z + jets, $t\bar{t}$	expected	Observed
0-jet	13.7 ± 0.7	2.23 ± 0.31	42.7 ± 2.1	49
1-jet $p_{\mathrm{T,H}}$ <60 GeV	3.09 ± 0.29	0.53 ± 0.07	12.5 ± 0.9	12
1-jet 60 GeV< $p_{\mathrm{T,H}}$ < 120 GeV	0.88 ± 0.11	0.38 ± 0.05	6.7 ± 0.7	9
1-jet $p_{\mathrm{T,H}} > 120$ GeV	0.14 ± 0.02	0.045 ± 0.007	1.65 ± 0.22	3
2-jet VH-enriched	0.65 ± 0.13	0.187 ± 0.021	4.4 ± 0.5	3
2-jet VBF-enriched $p_{\mathrm{T(j1)}} < 200$ GeV	1.1 ± 0.3	0.40 ± 0.04	7.7 ± 0.7	16
2-jet VBF-enriched $p_{\mathrm{T(j1)}} > 200$ GeV	0.09 ± 0.03	0.054 ± 0.005	0.72 ± 0.10	3
VH-leptonic-enriched	0.05 ± 0.01	0.014 ± 0.001	0.38 ± 0.02	0
ttH-enriched	0.01 ± 0.01	0.07 ± 0.04	0.47 ± 0.05	0
Total	19.7 ± 1.3	3.9 ± 0.5	77 ± 4	95

Table 8.7: The expected and observed number of events in the mass range of 118 GeV $< m_{4\ell} <$ 129 GeV for an integrated luminosity of 36.1 fb^{-1} in each category. The signal process is assuming the SM Higgs boson with a mass of 125 GeV.

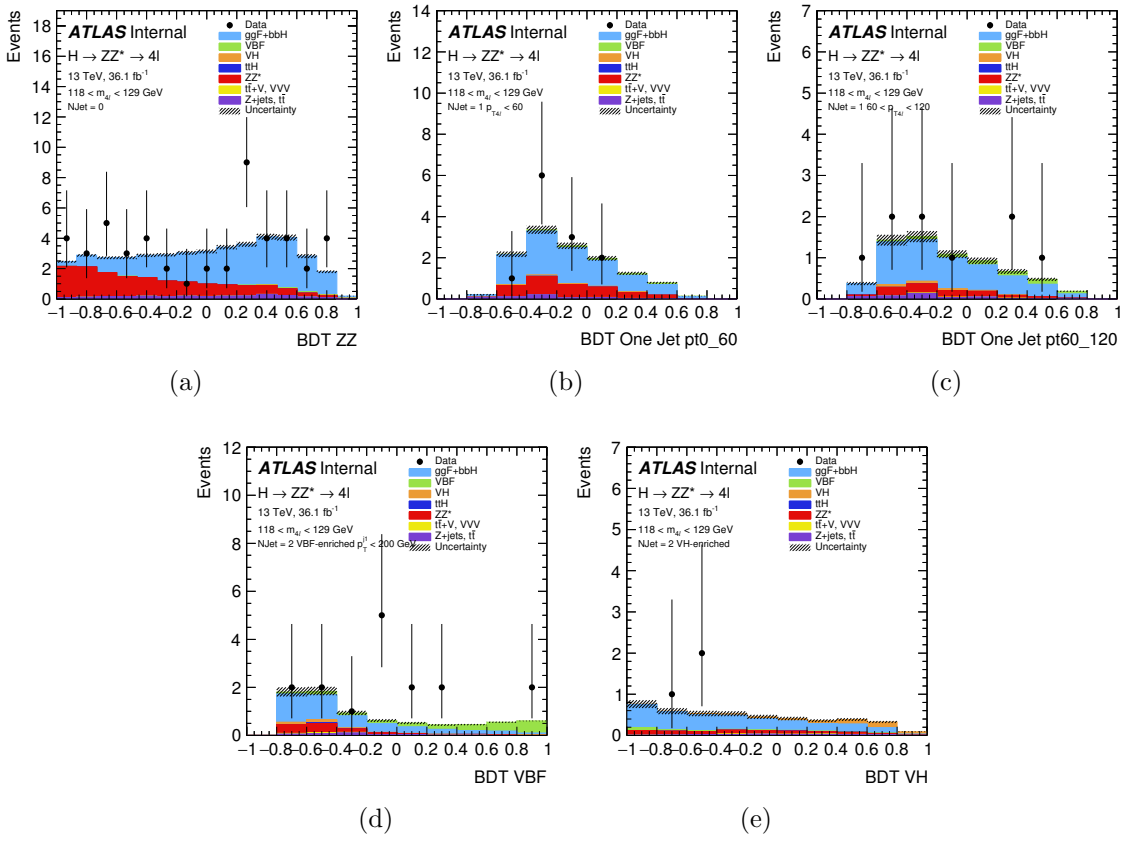

Figure 8.10: Expected and observed distributions of the BDT output score in the 0-jet (8.10a), 1-jet with $p_{\mathrm{T,H}} < 60$ GeV (8.10b), 1-jet with 60 GeV $< p_{\mathrm{T,H}} < 120$ GeV (8.10c), 2-jet VBF-enriched with $p_{\mathrm{T(j1)}} > 200$ GeV (8.10d) and 2-jet VH-hadronic-enriched (8.10e) categories with an integrated luminosity of 36.1 fb^{-1} collected at $\sqrt{s} = 13$ TeV.

observed in the 2-jet VBF-enriched categories. The VBF production is observed with an evidence of 3.4σ with respect to an expected significance of 1.4σ.

Measured quantity	Expected cross section (pb)	Observed cross section (pb)
$(\sigma \cdot B)^{ZZ}_{\text{ggF+bbH}}$	$1.18^{+0.28}_{-0.25}$	$1.31^{+0.30}_{-0.27}$
$(\sigma \cdot B)^{ZZ}_{\text{VBF}}$	$0.093^{+0.106}_{-0.073}$	$0.37^{+0.17}_{-0.14}$
$(\sigma \cdot B)^{ZZ}_{\text{VH}}$	$0.050^{+0.122}$	$0.000^{+0.041}$
$(\sigma \cdot B)^{ZZ}_{ttH}$	$0.013^{+0.048}$	$0.000^{+0.019}$

Table 8.8: The expected and measured results at 68.3 % CL for the stage-0 production bins using 36.1 fb^{-1}of data collected at $\sqrt{s} = 13$ TeV.

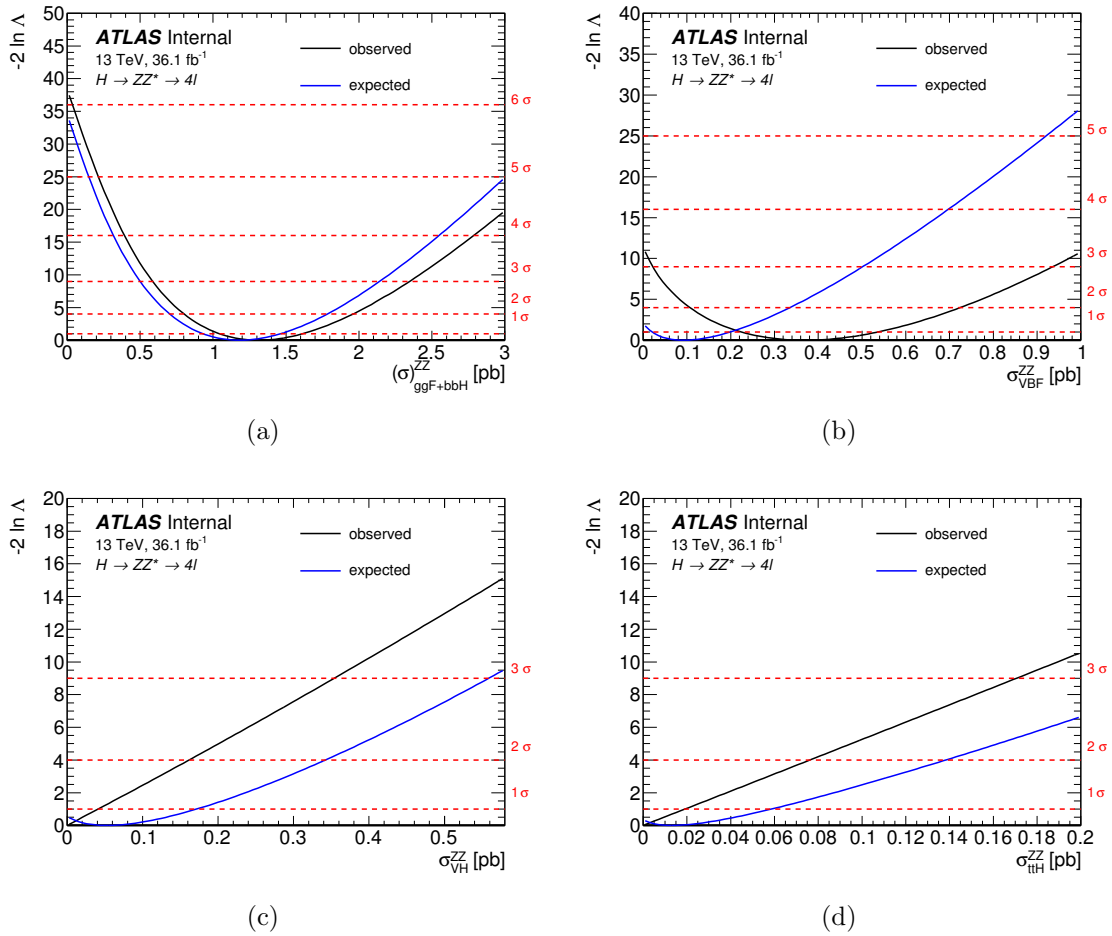

(a) (b)

(c) (d)

Figure 8.11: NLL scans to probe the ggF and bbH combined (8.11a), VBF (8.11b), VH (8.11c) and ttH (8.11d) production mechanisms in the $H \to ZZ^* \to 4\ell$ channel.

8.1.6.3 Signal Strengths Fits

The cross section measurements shown in Section 8.1.6.2 are interpreted into signal strength parameters including theory uncertainties on the SM prediction of the Higgs boson production and decay branching ratio. To probe possible deviations from the SM predictions of the Higgs boson couplings to SM bosons and fermions, two signal strengths parameters $\mu_{\text{ggF+bbH+ttH}}$ and $\mu_{\text{VBF+VH}}$ are introduced, assuming same signal strengths for fermion-mediated processes ggF, bbH and ttH production mechanisms, and same signal strengths for vector boson-mediated processes VBF and VH. The contours at 68% and 95% CL in the $\mu_{\text{ggF+bbH+ttH}} - \mu_{\text{VBF+VH}}$ plane are shown in Figure 8.12, reflecting the observed result is compatible with the SM prediction well within 2σ level.

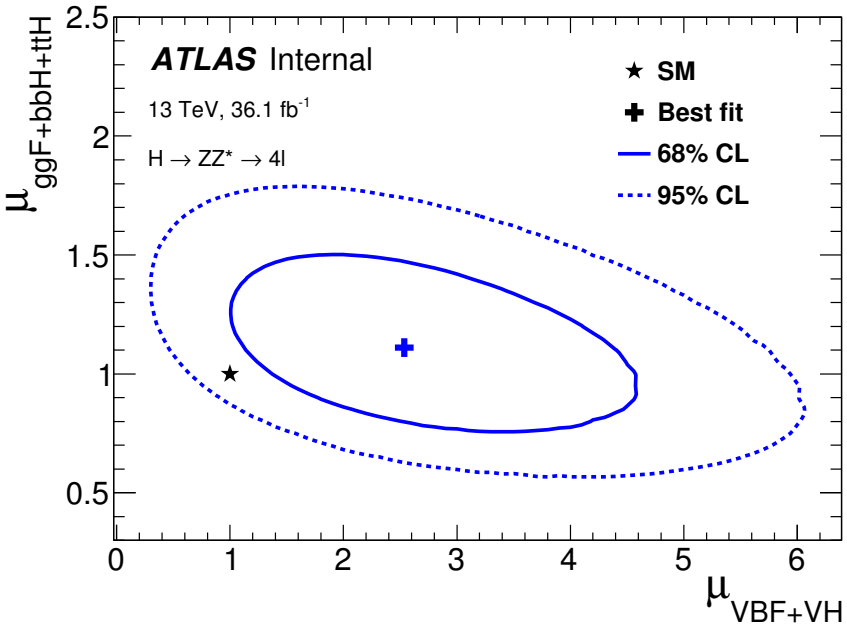

Figure 8.12: The best-fit value (cross) and contours at 68% (solid line) and 95% (dashed line) CL in the $\mu_{\text{ggF+bbH+ttH}}$ - $\mu_{\text{VBF+VH}}$ plane based on 36.1 fb^{-1} of data at 13 TeV, together with the SM prediction (star).

8.1.6.4 Coupling Fits

The cross section measurements shown in Section 8.1.6.2 can also be interpreted in the κ framework, which is described in Section 2.2.4.4. To probe possible deviations from the SM predictions of the Higgs boson couplings to SM bosons and fermions, two Higgs boson coupling strength modifiers are introduced κ_F and κ_V, assuming that

all the coupling strengths of Higgs boson to fermions are the same, and all coupling strengths to bosons are the same, and that there are no undetected or invisible Higgs boson decays, and no new physics contribution to the loop process. The contours at 68% and 95% CL in the $\kappa_V - \kappa_F$ plane are shown in Figure 8.13, where the $\kappa_F > 0$ and $\kappa_V > 0$ plane is shown because the $H \to ZZ^* \to 4\ell$ channel is sensitive to the magnitude of the two coupling strength modifiers. The compatibility between the observed result and the SM prediction is 1.3σ which corresponds to a p-value of 18%.

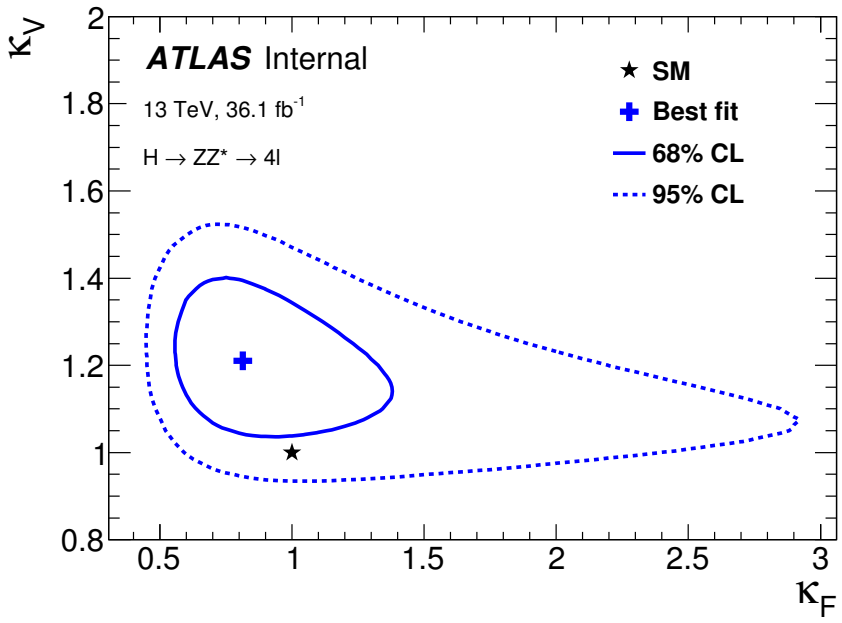

Figure 8.13: The best-fit value (cross) and contours at 68% (solid line) and 95% (dashed line) CL in the κ_F - κ_V plane based on 36.1 fb^{-1} of data at 13 TeV, together with the SM prediction (star).

8.2 Combined Measurement of Higgs Boson Production and Decay in Four-Lepton and Diphoton Decay Channels

8.2.1 Introduction

This combined measurements on the Higgs boson production cross sections and branching ratios are based on the measurements performed in the $H \to \gamma\gamma$ [118] and $H \to ZZ^* \to 4\ell$ decay channels [117]. The dateset used correspond to an integrated luminosity of 13.3 fb^{-1}and 14.8 fb^{-1}at centre-of-mass energy of $\sqrt{s} = 13$ TeV, for the $H \to \gamma\gamma$ and $H \to ZZ^* \to 4\ell$ channels, respectively.

Higgs boson production cross section of production mechanism i ($\sigma_{\mathtt{i}}$) multiplied by its branching ratios to the final state f (B^f) is denoted as $(\sigma \cdot \mathrm{B})^f_{\mathtt{i}}$. $(\sigma \cdot \mathrm{B})^f_{\mathtt{i}}$ is measured in the phase space $|y_H| < 2.5$, where y_H is the Higgs boson rapidity. This phase space is chosen considering the $H \to \gamma\gamma$ and $H \to ZZ^* \to 4\ell$ analyses have a negligible acceptance in the forward region $|y_H| > 2.5$. Therefore the cross sections measured have reduced theoretical uncertainties comparing to those if measured in the full phase space.

This combined analysis is sensitive to five production processes (ggF, VBF, VH-had, VHlep and top), which are explained more below:

- ggF includes $gg \to H$ and $b\bar{b}H$ processes, assuming SM predictions for the ratio of the cross section of the two processes.
- top includes $t\bar{t}H$ and tH processes, assuming SM predictions for the ratio of the cross sections of the two processes in the $H \to \gamma\gamma$ channel analysis. tH is not included in the $H \to ZZ^* \to 4\ell$ channel analysis due to negligible event yield.
- WH and ZH processes are grouped together separately for hadronic (VHhad) and leptonic (VHlep) decays of the vector boson.

The ratios of the Higgs boson production cross section in the phase space $\sigma_i(|y_H| < 2.5)$ and the full phase space shown in Table 8.9 are estimated using MC simulations. Together with the theoretical calculations summarized Ref. [36] for the cross sections in the full phase space, they are used to calculate the SM prediction for the measured cross sections shown in Section 8.2.3.

The measurements performed including $(\sigma \cdot \mathrm{B})^f_{\mathtt{i}}$ for the five production processes introduced above in the two Higgs decay channels, and the production cross-sections $\sigma_{\mathtt{i}}$ for the five production processes by assuming SM Higgs decay branching ratio. Finaly, the global signal strength μ which are introduced in Section 2.2.4.4, is also reported.

8.2.2 Input Analyses and the Combined Model

The mass spectrum passing the inclusive event selection in the $H \to \gamma\gamma$ and $H \to ZZ^* \to 4\ell$ channels are presented in Figure 8.14 [118] and 8.15 [117]. In order to probe different Higgs production mechanisms, events are categorized based on the topologies and kinematics of the physics objects in the final state.

The combined model is built by incorporating all categories into one likelihood model and using the same parameters to incorporate the parameters of interest and

Process	$\sigma_i(\lvert y_H\rvert < 2.5)/\sigma_i$
$gg \to H$	0.907
$qq' \to qq'H$	0.932
$q\bar{q}' \to WH(W \to \text{had.})$	0.870
$q\bar{q}/gg \to ZH(Z \to \text{had.})$	0.900
$q\bar{q}' \to WH(W \to \text{lep.})$	0.869
$q\bar{q} \to ZH(Z \to \text{lep.})$	0.900
$gg \to ZH(Z \to \text{lep.})$	0.965
$q\bar{q}/gg \to t\bar{t}H$	0.985

Table 8.9: Ratios between $\sigma_i(|y_H| < 2.5)$ and the total cross section for each production process. The ratios for $b\bar{b}H$ and tH processes are set to one for simplicity without affecting the accuracy of the results.

common systematic uncertainties in the two individual analyses. The main experimental uncertainties include uncertainties on the electromagnetic energy resolution and the photon identification efficiency. The dominating theoretical uncertainties are the ones on the acceptance of gluon fusion production in the categories with requirement on the number of jets in the event.

8.2.3 Results

8.2.3.1 Production Cross Section Multiplied by Branching Ratios

Measurements of the $(\sigma \cdot \mathrm{B})^f_{\mathtt{i}}$ are carried out, including ggF, VBF, VHlep, VHhad and top production processes measured in the $H \to \gamma\gamma$ channel, ggF and VBF production processes measured in the $H \to ZZ^* \to 4\ell$ channel. The VHlep, VHhad, and top processes are not constrained well by data in the $H \to ZZ^* \to 4\ell$ decay channel, thus they are fixed to the SM prediction with theoretical uncertainties included when performing all the measurements. The measured results of $(\sigma \cdot \mathrm{B})^f_{\mathtt{i}}$ are summarized in Table 8.10, together with SM predictions for comparison. The measured results are found to be in good agreement with the SM predictions, and the compatibility with SM predictions corresponds to a p-value of 11%. The measured cross sections divided by the SM predictions are summarized in Figure 8.16.

The ggF and VBF cross sections are measured with the highest precision among all the production processes. There is sizable correlation between the two measurements due to the contamination of events produced via the ggF mechanism in the VBF-

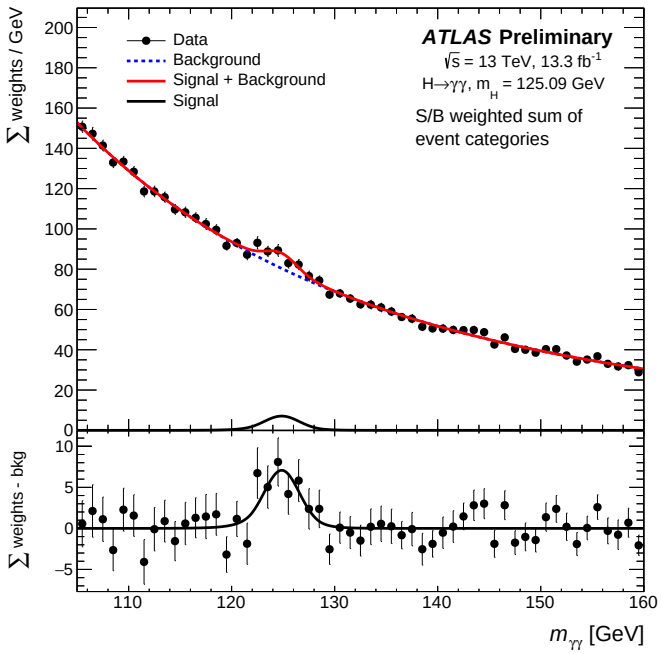

Figure 8.14: The mass spectrum for the $H \to \gamma\gamma$ channel. The black data points show the measured distribution, where each event is weighted by the signal-to-background ratio of the event category it belongs to. The blue dashed curve shows the result of a background-only fit to the data, the red curve shows the summed signal and background distribution based on the fitted signal yields, and the black curve shows the signal component. The bottom inset displays the residuals of the data with respect to the fitted background component.

		$H \to ZZ^*$	$H \to \gamma\gamma$
ggF	Observed (pb)	$1.58\,^{+0.46}_{-0.39}$	$0.063\,^{+0.030}_{-0.029}$
	SM prediction (pb)	1.18 ± 0.07	0.101 ± 0.006
VBF	Observed (fb)	350^{+260}_{-200}	$18\,^{+6}_{-6}$
	SM prediction (fb)	93.0 ± 2.8	8.00 ± 0.29
VHhad	Observed (fb)	fixed to SM	$-2.5\,^{+6.8}_{-5.8}$
	SM prediction (fb)	36.0 ± 1.2	3.09 ± 0.12
VHlep	Observed (fb)	fixed to SM	$1.0^{+2.5}_{-1.9}$
	SM prediction (fb)	17.0 ± 0.5	1.46 ± 0.05
top	Observed (fb)	fixed to SM	$-0.3^{+1.6}_{-1.2}$
	SM prediction (fb)	15.9 ± 1.5	1.36 ± 0.13

Table 8.10: The observed value in data of $(\sigma \cdot \mathrm{B})^f_{\mathtt{i}}$ for channel $\mathtt{i} \to H \to f$, and the SM predictions.

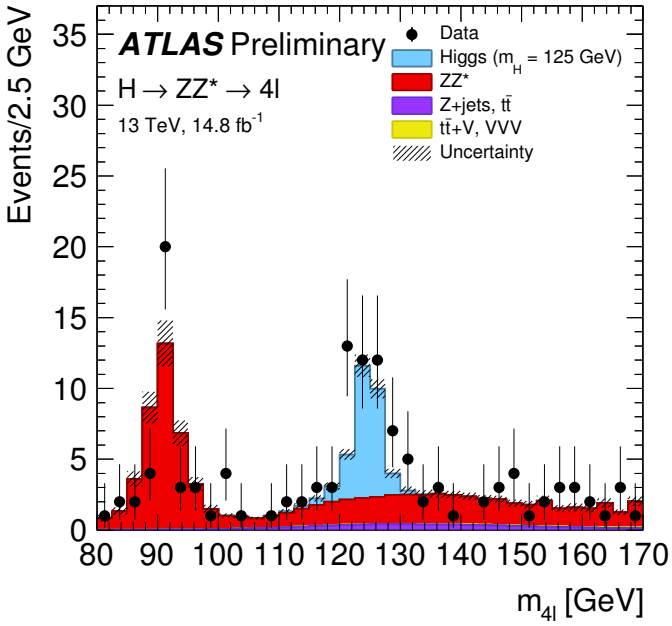

Figure 8.15: The mass spectrum for the $H \to ZZ^* \to 4\ell$ channel. The black data points show the measured distribution, compared to the background expectation.

enriched categories. Hence, 68% and 95% CL contours in the $(\sigma \cdot \mathrm{B})^f_{\mathrm{ggF}}$ versus $(\sigma \cdot \mathrm{B})^f_{\mathrm{VBF}}$ plane are measured in the $H \to \gamma\gamma$ and $H \to ZZ^*$ channels, which are shown in Figure 8.17 in terms of the measured values of $(\sigma \cdot \mathrm{B})^f_{\mathrm{i}}$ divided by the SM prediction.

8.2.3.2 Production Cross Sections Assuming SM Branching Ratios

The measurements of the production cross sections σ_i by assuming SM Higgs decay branching ratios and taking into account the associated theoretical uncertainties are summarized in Table 8.11 and Figure 8.18. The compatibility between the measurements and the SM prediction corresponds to a p-value of 21%, indicating good agreement between the measurement and the SM prediction.

8.2.3.3 Signal Strength

The global signal strength μ is measured to be $\mu = 1.13^{+0.18}_{-0.17}$ using the NLL scan shown in Figure 8.19. This measurement is in good agreement with the SM prediction, with the compatibility corresponding to a p-value of 43%.

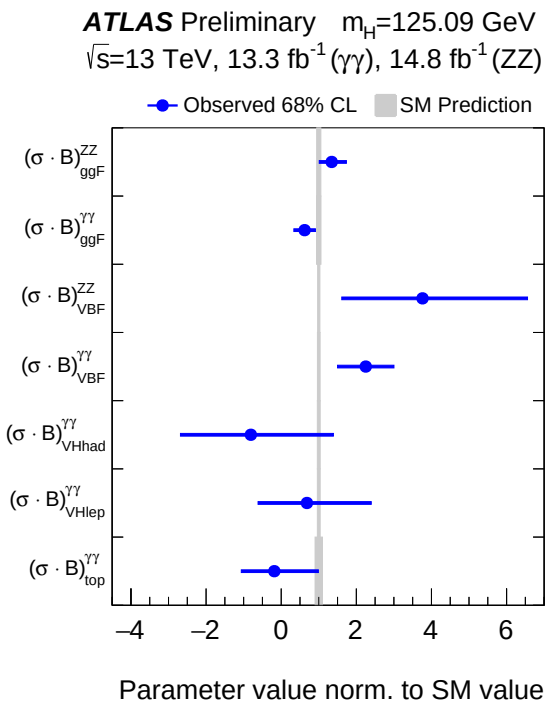

Figure 8.16: The measured cross sections $(\sigma \cdot \mathrm{B})^f_{\mathtt{i}}$ for channel $\mathtt{i} \to H \to f$ divided by the SM predictions shown by the blue dots and error bars, and the grey bands indicating the theoretical uncertainties in the SM predictions.

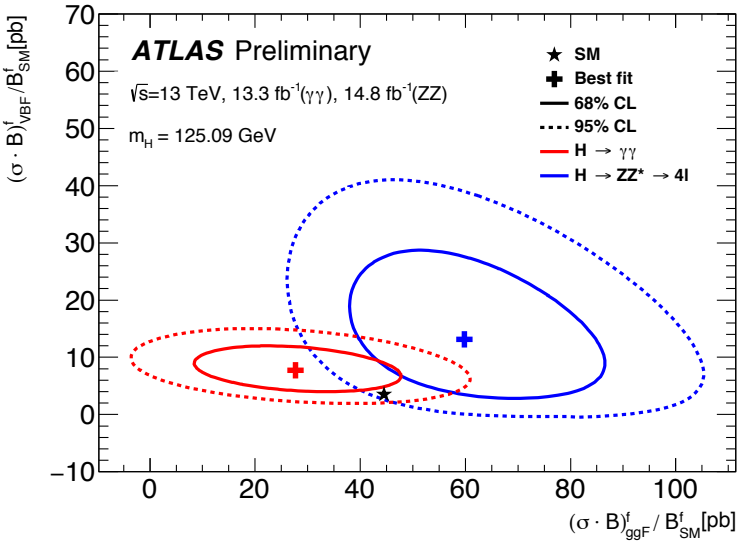

Figure 8.17: Contours in the $(\sigma \cdot \mathrm{B})^f_{\mathrm{ggF}}/\mathrm{B}^f_{\mathrm{SM}} - (\sigma \cdot \mathrm{B})^f_{\mathrm{VBF}}/\mathrm{B}^f_{\mathrm{SM}}$ plane as measured in the $H \to \gamma\gamma$ and $H \to ZZ^*$ decays, together with the SM prediction.

Process	Observed (pb)	SM prediction (pb)
σ_{ggF}	$47.8\,^{+9.8}_{-9.4}$	44.5 ± 2.3
σ_{VBF}	$7.9\,^{+2.8}_{-2.4}$	3.52 ± 0.07
σ_{VHhad}	$-2.5\,^{+2.9}_{-2.6}$	1.36 ± 0.03
σ_{VHlep}	$0.32\,^{+1.07}_{-0.79}$	0.64 ± 0.02
σ_{top}	$-0.11\,^{+0.67}_{-0.54}$	0.60 ± 0.06

Table 8.11: Measured production cross sections assuming SM Higgs decay branching fractions, with the SM predictions for comparison.

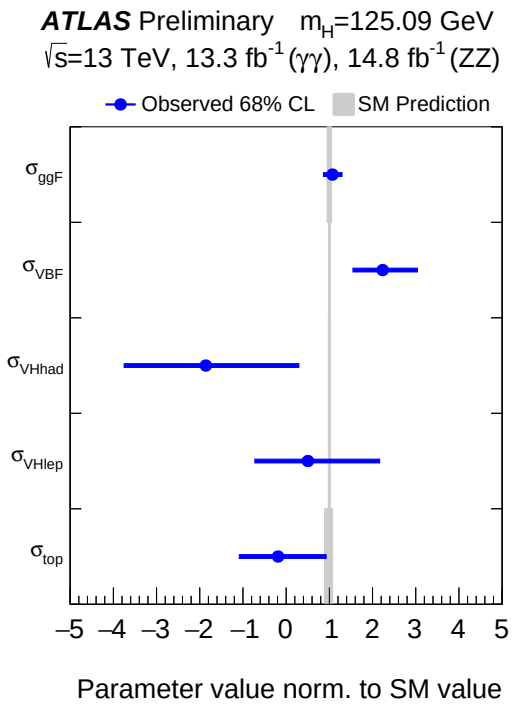

Figure 8.18: The measured production cross sections assuming SM Higgs decay branching fractions, normalized to the SM predictions shown in the blue dots with error bars, compared with the SM predictions in the grey bands.

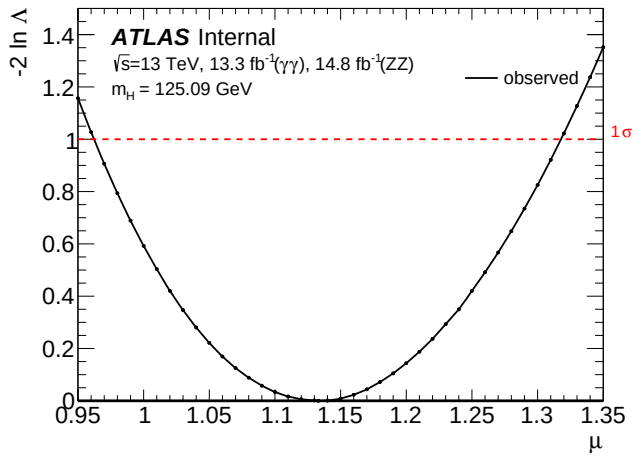

Figure 8.19: The NLL scan of the global signal strength μ shows the μ is measured to be $\mu = 1.13\,^{+0.18}_{-0.17}$ at 68.3% CL (1σ).

CHAPTER IX

Search for New Resonances in ZZ Final State

Searching for new physics beyond the SM is an important goal of the LHC physics program. The LHC is offering unprecedented opportunities to search for new physics phenomena. There are many possible extensions to the SM Higgs sector such as the 2HDM and the EWS models, which predicted the existence of additional Higgs bosons. This chapter discusses the search for new resonances (denoted by S) decaying to a pair of Z bosons in the four-lepton final state ($ZZ \to 4\ell$, $\ell = e$ or μ) in a mass range between 200 GeV and 1 TeV, with early 13 TeV data corresponding to an integrated luminosity of 3.2 fb^{-1} collected by the ATLAS detector [72]. The $ZZ \to 4\ell$ channel has very good mass resolution while relatively small ZZ decay branching fraction of 0.45% compared to $ZZ \to 2\ell 2q$ (4.70%) and $ZZ \to 2\ell 2\nu$ (1.35%), making it the most sensitive channel for searches for new resonances with masses below about 400 GeV in all ZZ decay channels. At a higher mass scale, the $ZZ \to 4\ell$ channel helps improve the sensitivity by combining the result with other ZZ decay channels. The limits combining ZZ decay channels (4ℓ, $2\ell 2\nu$ [120], $2\ell 2q$ [121] and $2\nu 2q$ [122]) and probing a mass range of 200 GeV to 3 TeV based on the same dataset will also be presented in this chapter.

The strategy of the search is to simultaneously look for narrow resonance peaks over smooth background in three sub-channels classified by the flavor of the final state leptons: $ZZ \to 4\mu$, $ZZ \to 2e2\mu$ and $ZZ \to 4e$. No significant excess over background prediction in data is observed and 95% CL_s upper limits are set on the production cross section multiplied by the branching fraction of a scalar particle decaying to four leptons ($\sigma \times BR(S \to ZZ \to 4\ell)$), with a mass ($m_S$) from 200 GeV to 1 TeV. The width of the scalar particle is assumed to be much smaller than the detector mass resolution, and Narrow Width Approximation (NWA) is used. Under the NWA assumption, the interference effect between the resonance and ZZ

continuum is negligible. The lepton and event selection, and background estimation methods follow the strategy presented in Chapter V.

9.1 Signal and Background Modeling

9.1.1 Signal

The resonance is simulated using the Powheg-BOX v2 generator [123, 94], which calculates separately the gluon fusion and vector-boson fusion production mechanisms with matrix elements up to NLO . SM Higgs boson couplings structure is assumed. The lineshape of the new resonance for all masses is modelled with a Breit-Wigner with a fixed width of 4.07 MeV, which is the value of the natural width predicted for the SM Higgs boson with a mass of 125 GeV. The choice of a fixed width of 4.07 MeV is arbitrary, since the precise value is not importance as long as it is significantly smaller than the detector mass resolution. Powheg-BOX is interfaced to Pythia8 [124] for decaying the resonance into the $ZZ \to 4\ell$ final state, and later for the showering and hadronization. Photos++ [125] is used to model QED emissions from electroweak vertices and charged leptons. MC simulation samples are generated for ggF and VBF production mechanisms, for 200 GeV $< m_S <$ 1000 GeV in steps of 10 GeV.

Based on these MC simulations, analytical models consisting of a linear combination of a Crystal Ball and a Gaussian function are determined to model the invariant mass distribution of the four-lepton system for the signal processes produced via the ggF and VBF mechanisms for each of the mass point where MC simulation samples are available. It is found that the analytical models determined from these two processes are very similar, thus for simplicity, the analytical models determined by the ggF production mechanism is used. Next, each parameter of the analytical models for different mass points is fitted to a first or second order polynomial to provide continuous description of the invariant mass distribution as a function of m_S over the full search range of 200 GeV $< m_S <$ 1000 GeV. The signal efficiency is modelled in a similar way by determine the value for each mass point from MC simulation sample and then using these values to determine first or second order polynomials to obtain continuous description over the full mass range.

9.1.2 Background

The SM ZZ continuum production is the dominate background for this search. The ZZ background from quark-antiquark annihilation is modelled using POWHEG-

BOX v2 generator using CT10 PDF set in the hard-scattering process while the CTEQL1 PDF set is used for the parton shower. The nonperturbative effects are modelled using the AZNLO [126] tune. NNLO QCD and NLO EW corrections for this process are included as a function of the invariant mass of the four-lepton system [127]. The gluon-initiated ZZ production, includnig the ZZ continuum, the Higgs boson produced off-shell via the gluon fusion mechanism and their interference, is modelled using Sherpa 2.1.1 [104]. A k-factor of 1.7 is applied to account for corrections from higher-order calculations.

Other background contributions including the $Z + jets$ and $t\bar{t}$, WZ, ttV, triboson productions are minor. $Z + jets$ and $t\bar{t}$, WZ background contributions are estimated with data. The triboson backgrounds ZZZ, WZZ, and WWZ with four or more leptons are modelled using Sherpa 2.1.1. For the all-leptonic $t\bar{t} + Z$ background MadGraph+PYTHIA 8 is used.

9.2 Systematic Uncertainties

The systematic uncertainties for this search includes theoretical ones affecting the expected numbers of background events, the invariant mass distribution of the four-lepton system for the background processes, as well as the signal acceptances. The experimental uncertainties impact the expected numbers of background events, signal acceptances, and the invariant mass distribution of the four-lepton system for both signal and background processes.

9.2.1 Theory

The QCD scale and PDF theoretical uncertainties on the estimation of quark-initiated ZZ^* process include influences on the overall expected number in the signal region which are estimated to be 4% and 5%, respectively, as well as on the $m_{4\ell}$ distribution. The higher order QCD corrections for the expected number of events from the gluon-initiated ZZ^* background process is applied as a k-factor of 1.7 with an uncertainty of 30%, as well as 8% included to account for the PDF uncertainty. The theoretical uncertainties on the signal acceptance include contributions from QCD scales, PDF and showering, and they are studied to be well below 1%.

9.2.2 Experiment

The dominating experimental uncertainties include the uncertainty on the data luminosity measurement, the lepton identification and reconstruction efficiencies. Re-

garding the expected number of events from both the background and the signal processes, effect from the muon identification and reconstruction systematic uncertainties is below 2% while from the electron identification and reconstruction systematic uncertainties is up to 3%. In addition, regarding the impact on the invariant mass distribution of the four-lepton system, sources from the lepton identification and reconstruction have a tiny affect of about 1%, while the lepton momentum (or energy) scale and resolution have a larger effect of about 4%. The impact of the experimental uncertainties on the analytical signal parametrization has also been studied. The effect from the lepton resolution uncertainties on the width of the Gaussian and Crystal Ball function is estimated to be $10-20\%$ while impact from the other lepton systematic uncertainties are found to be negligible and thus are not included for the simplification of the signal parametrization.

9.3 Statistical Modeling

The unbinned likelihood construction and statistical procedure for the upper limit setting follow the method described in Chapter VI. The signal pdf construction is described in section 9.1 while the pdf of the main background process the ZZ continuum production uses a distribution based on the MC sample while smoothed by a kernel density estimation method [128] to reduce the statistical fluctuations in the MC sample. The parameter of interest of this search is the cross section times branching ratio to four leptons for a new scalar particle $\sigma \times BR(S \to ZZ \to 4\ell)$.

9.4 Results

9.4.1 Limit in the Four-Lepton Channel

The number of observed candidate events and the background expectations in the three decay channels in $m_{4\ell}$ mass region above 200 GeV are presented in Table 9.1. The mass spectrum with data and background prediction overlaid is shown in Figure 9.1. No significant excess is observed in data with respect to the background prediction.

The upper limits at 95% CL_s on $\sigma \times BR(S \to ZZ \to 4\ell)$, which is the cross section times branching ratio to four leptons for a scalar particle, observed in data and expected from the background-only hypothesis as shown in Figure 9.2, are computed as a function of m_S by performing an unbinned likelihood fit to the data and Asimov dataset [90], respectively, and following the CL_s procedure described in section 6.2.

Channel	ZZ^*	$Z+\text{jets}$, $t\bar{t}$, WZ	$t\bar{t}V$,VVV	Expected	Observed
4μ	22.1 ± 2.2	0.05 ± 0.02	0.23 ± 0.01	22.4 ± 2.2	20
$2\mu 2e$	35.0 ± 3.1	0.11 ± 0.03	0.40 ± 0.01	35.5 ± 3.1	30
$4e$	13.9 ± 2.1	0.06 ± 0.02	0.18 ± 0.01	14.1 ± 2.1	12
Total	71 ± 8	0.23 ± 0.04	0.81 ± 0.04	72 ± 8	62

Table 9.1: The number of expected and observed events for the four-lepton final states in a range of $m_{4\ell} > 200$ GeV, for an integrated luminosity of 3.2 fb^{-1}at $\sqrt{s} = 13$ TeV.

The observed limits agree with the SM prediction within the uncertainties. Since the signal model is a scalar particle with a narrow width significantly smaller than the detector resolution, the results are found to be valid for models in which the width of the scalar particle is less than 0.5% of its mass ($\Gamma_S < 0.005 \times m_S$).

The limits are cross-checked with those obtained by using a different approach for the signal modelling, where the distribution is provided by the MC simulation after being smoothed out MC statistical fluctuations using kernel density estimation method [128]. The agreement is found to be within 5%.

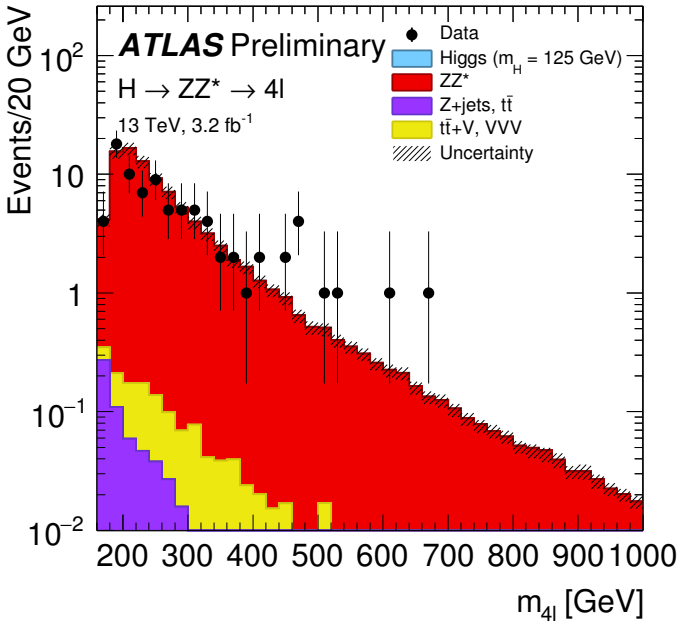

Figure 9.1: The invariant mass distribution of the four-lepton system in the range of $160-1000$ GeV with data shown by points and the SM prediction for the background processes shown by filled histograms.

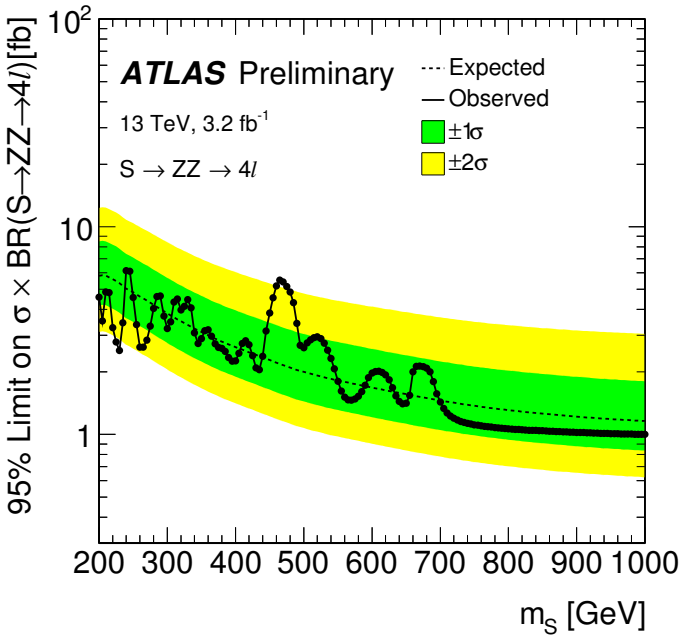

Figure 9.2: The upper limits at 95% CL_s on $\sigma \times BR(S \to ZZ \to 4\ell)$ in the NWA approximation.

9.4.2 Limit in Combining ZZ Decay Channels

Combining the searches in different ZZ decay channels is important to the search for heavy scalars due to that there is no single ZZ decay channel dominating the sensitivity over the full searched mass range. The 4ℓ channel is most sensitive when the mass of the scalar is below 400 GeV. At higher mass range, the $2\ell 2\nu$, $2\ell 2q$ and $2\nu 2q$ channels dominate the sensitivity. Based on the 2015 data collected at 13 TeV corresponding to an integrated luminosity of 3.2 fb^{-1}, the searches in the ZZ decay channels are combined. The limits for the mass range of 200 GeV $< m_S <$ 1000 GeV combing 4ℓ, $2\ell 2\nu$ and $2\ell 2q$ final states and the limits for the mass range of 1000 GeV $< m_S <$ 3000 GeV combing $2\ell 2q$ and $2\nu 2q$ final states are shown in Figure 9.3. No significant excess in data is observed. The data excess around 470 GeV has a local significance of about 3σ with respect to the background-only hypothesis, and it is reflected in the upper limit plot 9.2 that the data is close to the expected 2 sigma error band. This is interpretated as data fluctuation.

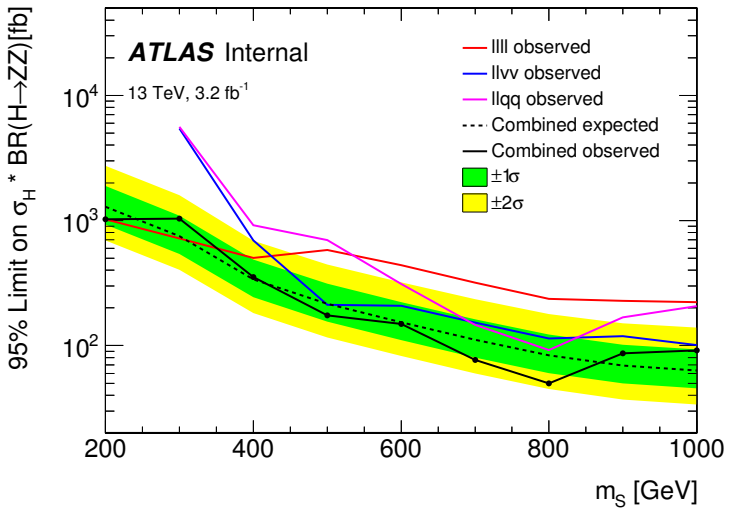

(a)

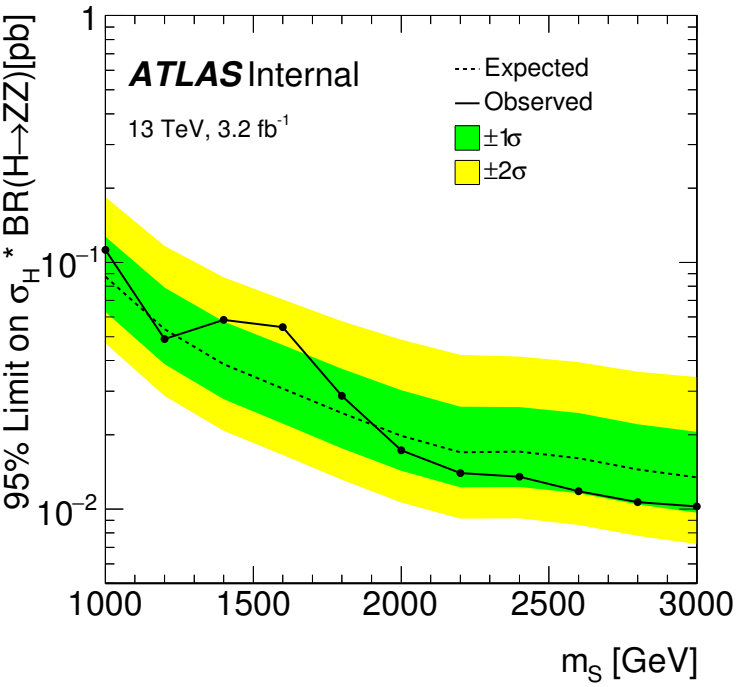

(b)

Figure 9.3: The limits at 95% CL_s on $\sigma \times BR(S \to ZZ)$ are set assuming a scalar particle signal in the NWA approximation combing ZZ decay channels. In the mass range of $200-1000$ GeV (9.3a) 4ℓ, $2\ell 2\nu$ and $2\ell 2q$ channels are combined. In the mass range of $1000-3000$ GeV (9.3b) $2\ell 2q$ and $2\nu 2q$ channels are combined.

CHAPTER X

Summary and Outlook

The thesis presented the studies on the Higgs boson properties including its spin and parity quantum numbers J^P, and the Higgs boson couplings to other particles with the four-lepton final state and combining with other Higgs boson decay channels. All the results are found to be consistent with a SM Higgs boson within the measurement uncertainties.

The exclusion of the tested BSM J^P models at more than 99.9% CL from combining the diboson decay channels based on the full LHC Run 1 dataset of 25 fb^{-1}of pp collision data at $\sqrt{s} = 7$ and $\sqrt{s} = 8$ TeV collected in 2011 and 2012 by the ATLAS experiment, helps to shift the experimental focus to probing the possibility of CP-mixing in the Higgs sector.

With 36.1 fb^{-1} of pp collision data at $\sqrt{s} = 13$ TeV collected in 2015 and 2016 by the ATLAS detector and using the four-lepton channel, the production cross section of the gluon fusion production mechanism multiplied by Higgs decay branching ratio to ZZ^* final state is measured with a precision of 21% (22% expected). A upper fluctuation in data in the VBF categories gives rise to an observed VBF signal significance of about 3.6σ (1.5σ expected) with respect to the hypothesis of none VBF production. VH and ttH targeted categories are included in the analysis, however, more data is needed to observe and measure them in the four-lepton channel. The precision of 15% for the coupling modifier κ_V and 40% for κ_F has been reached. The precision of these measurements are largely limited by the statistical uncertainty in data. The full LHC Run 2 data and beyond will be crucial for Higgs boson property measurements. The expected experimental precision and signal significance for the ggF, VBF, VH, and ttH Higgs boson production mechanisms in the four-lepton channel at the LHC are summarized in Table 10.1, based on the inputs, analysis methods and systematic uncertainties described in Section VIII.

Production Mechanism	$\int L = 100$ fb^{-1}	$\int L = 300$ fb^{-1}	$\int L = 3000$ fb^{-1}
$(\sigma \cdot B)^{\mathrm{ZZ}}_{\mathrm{ggF}}$ (pb)	$1.17^{+0.18}_{-0.17}$	$1.17^{+0.13}_{-0.12}$	$1.17^{+0.08}_{-0.07}$
$(\sigma \cdot B)^{ZZ}_{\mathrm{VBF}}$ (pb)	$0.093^{+0.060}_{-0.048}$	$0.093^{+0.035}_{-0.030}$	$0.093^{+0.012}_{-0.011}$
	2.4σ	3.9σ	
$(\sigma \cdot B)^{ZZ}_{\mathrm{VH}}$ (pb)	$0.050^{+0.059}$	$0.050^{+0.033}$	$0.050^{+0.010}$
	1.3σ	2.2σ	6.5σ
$(\sigma \cdot B)^{ZZ}_{t\bar{t}H}$ (pb)	$0.013^{+0.023}$	$0.013^{+0.012}$	$0.013^{+0.004}$
	1.0σ	1.7σ	5σ

Table 10.1: The expected sensitivity for the SM Higgs boson production mechanisms ggF, VBF, VH and ttH in the $H \to ZZ^* \to 4\ell$ channel, including the expected measured results of production cross section multiplied by branching ratio σ_i^f at 95% CL and the signal significance, for integrated luminosities of 100, 300, and 3000 fb^{-1} at $\sqrt{s} = 13$ TeV.

The LHC presents unpresented opportunities to search for new physics at a higher mass scale. A search for new resonances with the four-lepton final state based on 2015 data at 13 TeV is also presented in this dissertation. No significant excess with respect to the SM prediction is observed.

Precision Higgs coupling measurements and searching for new particles in multi-TeV mass region are important physics topics as the LHC continues upgrading its luminosity and energy in the coming years. The data analysis methods developed in this dissertation are applicable in ATLAS experiment to study the properties of the Higgs boson in more depth and to advance our understanding of particle physics by using the Higgs boson as a tool to further explore new physics.

APPENDIX

APPENDIX A

Study of MDT 12.5 ns TDC Time Jump on Front-end Electronics

During the LHC Run 1, the MDT operation has been plagued by rare 12.5 ns T_0 time shifts in chambers. T_0 is a parameter in the muon calibrations which measures the timing offset for the particle drift time in the MDT due to trigger and cable delays. Figure A.1 illustrates the cross-section of the MDT tube with ionization clusters distributed allow a muon track. T_0 corresponds to the drift time when a muon track passes the center of the tube. In the digital system, the digitization is based on the 40 MHz LHC clock. Each chamber exhibits a single T_0 value in any given run. In Run 1, A 12.5 ns time shift in the T_0 values for all mezzanine cards on a single CSM for the whole chamber is observed after initialization in one run out of a few thousand, as shown in Figure A.2 for Chamber BOL2C01 in 2012 daily calibrations.

The T_0 shift of 12.5 ns in Run 1 caused a decrease in the muon momentum resolution. Solving this issue will have a positive impact on the physics analysis involved with muons, such as the Higgs boson coupling measurements in the $H \rightarrow ZZ^* \rightarrow 4\ell$ channel through the improved the mass resolution of the Higgs boson allowing more events to fall into the analysis signal region and hence improving the signal-over-background ratio. Therefore, it is important to identify the source of the T_0 time shift and solve it for the Run 2 operations.

The MDT readout electronics are shown in Figure A.3. There are three possible sources causing the T_0 shifts: trigger receiver chip (TTCrx) on the chamber service module (CSM), the field-programmable gate array (FPGA) on CSM, and the ATLAS Muon TDC (AMT) chip on the mezzanine card. Photos of the CSM and mezzanine

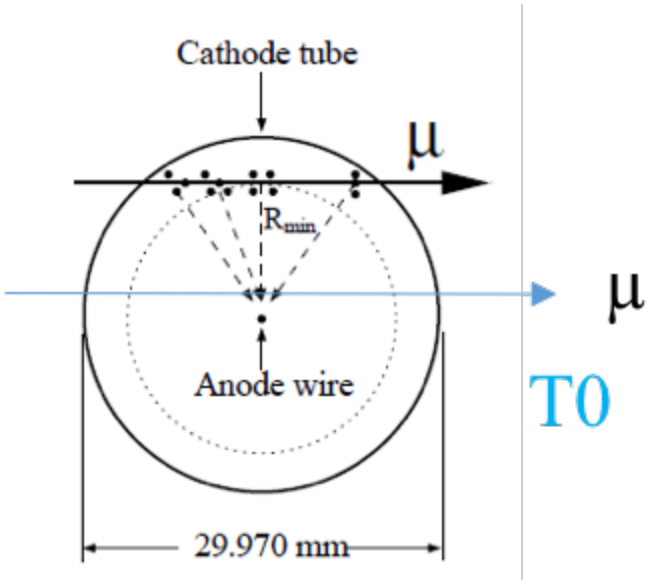

Figure A.1: The cross-section of the MDT tube with ionization clusters distributed allow a muon track

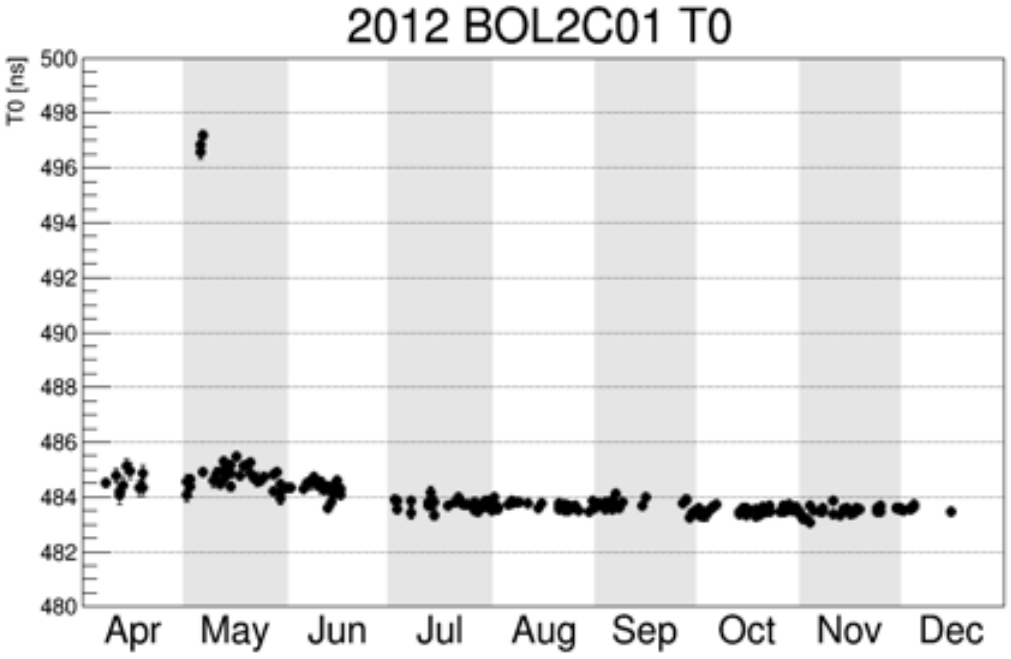

Figure A.2: T_0 values for chamber BOL2C01 from daily calibrations.

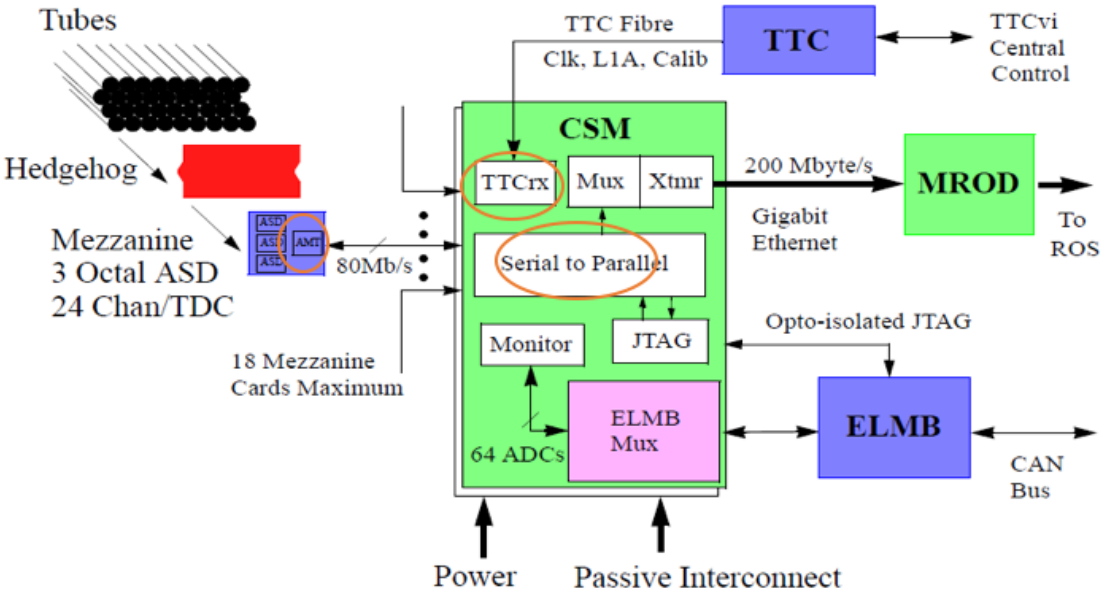

Figure A.3: The MDT readout electronics.

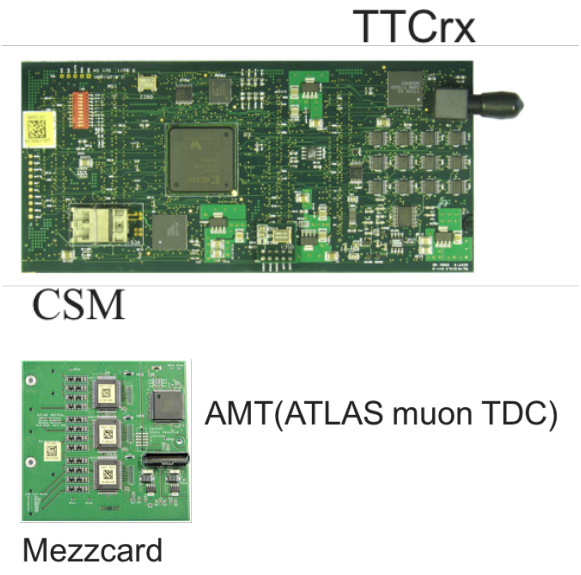

Figure A.4: The CSM and mezzanine card card.

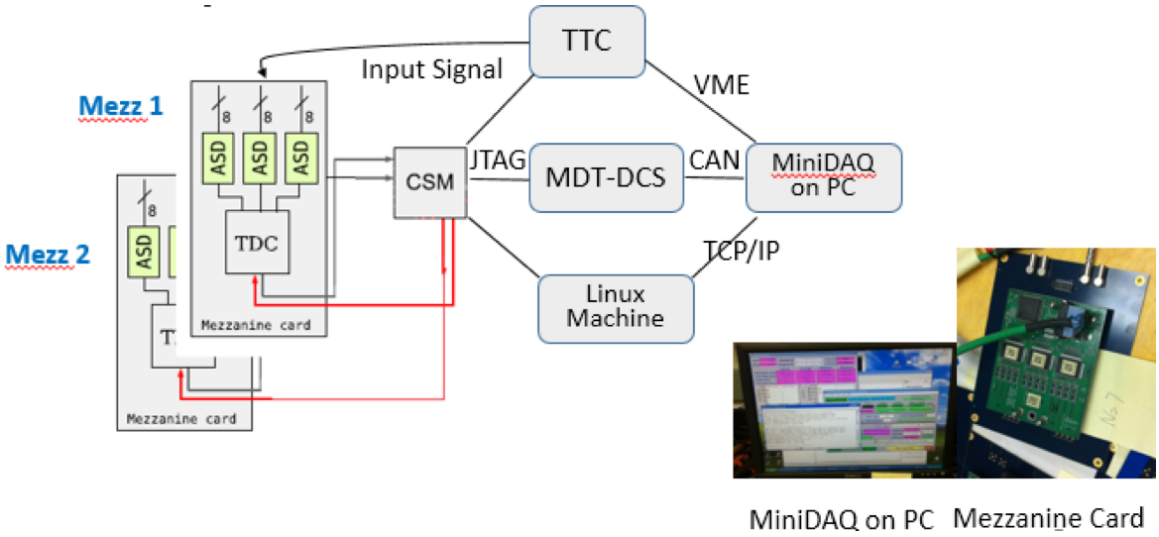

Figure A.5: Test stand at Michigan to debug the 12.5 ns TDC time shift.

card are included in Figure A.4. The Michigan ATLAS group have made huge efforts to look for the T_0 jump sources, however, such phenomena could not be repeated in our lab. To continue the effort to find the timing shift source, a dedicated test station in our lab is reset up as illustrated in Figure A.5. The key point in the setup is that two identical input signals are sent to two mezzanine cards which are synchronized with the TTC 40 MHz clock and the L1 trigger. The two input signals come from two identical outputs produced by same signal injected into NIM discriminator. Two mezzanine cards are included in the test so that we can require a coincidence of TDC time jump in the two cards to make sure the AMT is not responsible for the jump.

After many tests and trials, the 12.5 ns time jump finally is successfully reproduced in our lab for the first time, as we observe events with 12.5 ns time shift in the TDC spectrum from offline analysis of the data produced in the test stand in our lab, as shown in Figure A.6.

After observing the time shift offline, the next goal is to catch it online and identify the responsible source. Thus, the test program is modified so that when a time shift of 12.5 ns happens, the test program is able to pause the run to enable us to check the phase relationships of the three clocks associated with the three possible sources using oscilloscope. The three clocks are connected to the channels (CHN) in the oscilloscope:

- CHN 2- TTCvi module 40 MHz clock
- CHN 3- CSM FPGA 40 MHz input clock from TTCrx chip

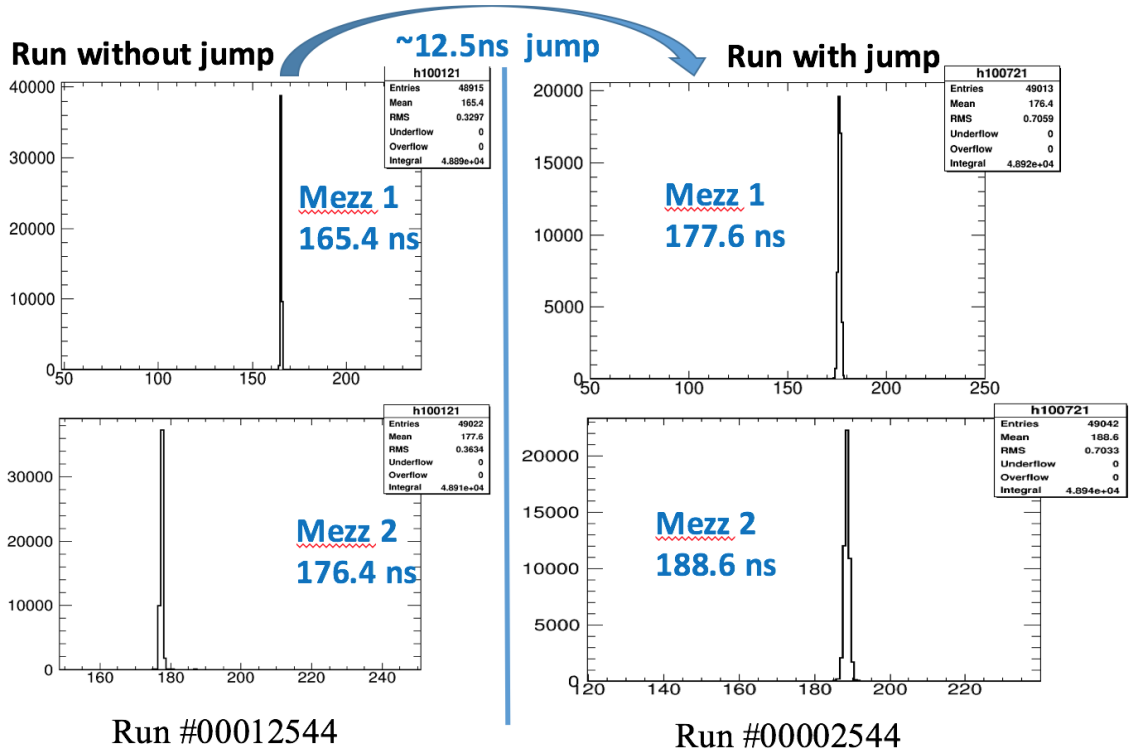

Figure A.6: TDC distribution of the two Mezzanine Card. TDC value is at a fixed point for all runs, making it possible for us to catch and debug 12.5 ns T_0 jump.

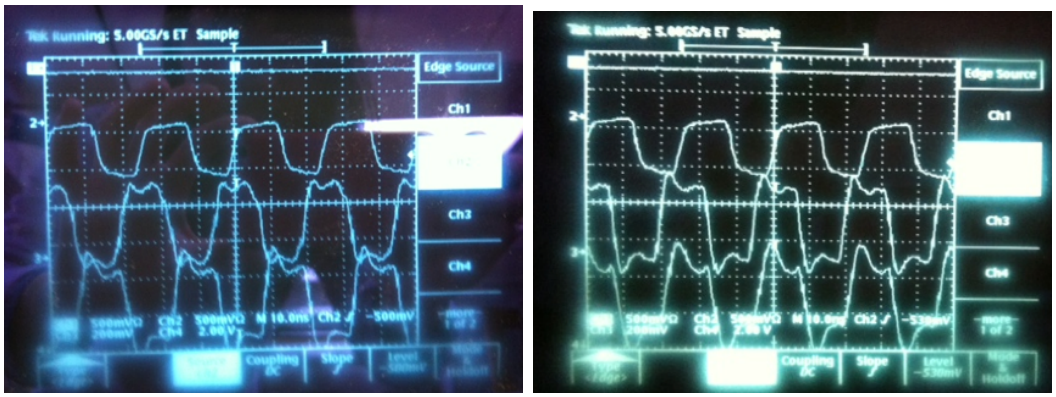

Figure A.7: Phase relationships of three clocks shown by the oscilloscope for the normal case (left) and the case with 12.5 ns TDC time jump (right).

- CHN 4- CSM FPGA 40 MHz clock to AMT chips

The time jump is successfully caught online using the modified program as shown in Figure A.7. The phase relationships of the clocks demonstrate that the culprit is the FPGA digital clock manager (DCM) in the CSM choosing a phase shifted by 180 degree compared to the normal case during the front-end electronics configuration phase.

In the next step, the function to pause a run when a time shift of 12.5 ns happens is disabled in the test program, to allow the test stand to deliver a large amount of data to allow a measurement of the rate of the events with the 12.5 ns time shift. The data are analyzed offline, and 16 runs out of in total 22478 runs are found to have the time shift in both of the two mezzanine cards as plotted in Figure A.8. The rate of the T_0 jump is thus measured to be 0.07%, consistent with the observation in Run 1.

Having known the cause, we carry out intensive tests on new versions of CSM firmware, and after many trials, we come to the following solution which cures the 12.5 ns time shift issue in lab. The method is that during initialization phase, the program will look into the input and out clock of the DCM, and test if the two clocks are in phase. If they are out of phase, an error bits are set, and external control will then have to re-initialize the CSM. The re-initialization can be done up to three times.

This solution is later tested in the ATLAS detector by my colleagues. It worked for most of mezzanines in the ATLAS detector, but few mezzanines in ATLAS always have trouble with wrong data transmission. The reason could be the tolerance on this new firmware is not large enough to deal with many different mezzanine cable

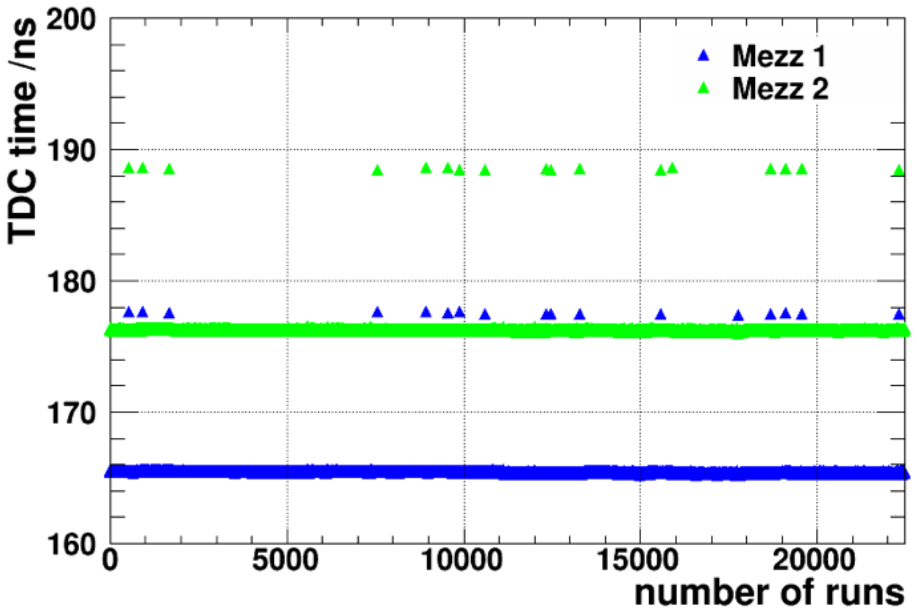

Figure A.8: In the rate measurement, 16 runs out of 22478 runs in total were found to have 12.5 ns T_0 shift in both of the two mezzanine cards.

length due too many clock resource is used by introducing clock monitoring. The final method used in ATLAS is to remove the DCM module by directly distributing the 40MHz clock to all mezzanines from CSM.

This work which has identified the source causing the 12.5 ns T_0 time shift, has laid the foundation for the elimination of the 12.5 ns T_0 jump in Run 2 data taking.

BIBLIOGRAPHY

BIBLIOGRAPHY

[1] S. L. Glashow. Partial symmetries of weak interactions. *Nucl. Phys.*, 22:579, 1961.

[2] Steven Weinberg. A model of leptons. *Phys. Rev. Lett.*, 19:1264, 1967.

[3] A. Salam. *Elementary Particle Theory*. Almqvist and Wiksell, Stockholm, 1968.

[4] F. Englert and R. Brout. Broken symmetry and the mass of gauge vector mesons. *Phys. Rev. Lett.*, 13:321, 1964.

[5] P. W. Higgs. Broken symmetries, massless particles and gauge fields. 12:132, 1964.

[6] P. W. Higgs. Broken symmetries and the masses of gauge bosons. 13:508, 1964.

[7] P. W. Higgs. Spontaneous symmetry breakdown without massless bosons. 145:1156, 1966.

[8] J. M. Cornwall, D. N. Levin, and G. Tiktopoulos. Uniqueness of spontaneously broken gauge theories. *Phys.Rev.Lett.*, page 1268, 1973.

[9] J. M. Cornwall, D. N. Levin, and G. Tiktopoulos. Derivation of Gauge Invariance from High-Energy Unitarity Bounds on the s Matrix. *Phys.Rev.D*, page 1145, 1974.

[10] C. H. Llewellyn Smith. High-Energy Behavior and Gauge Symmetry. *Phys.Lett.B*, page 233, 1973.

[11] B.W. Lee, C. Quigg, and H. B. Thacker. Weak interactions at very high energies: The role of the Higgs-boson mass. *Phys.Rev.D*, page 1519, 1977.

[12] ALEPH, CDF, D0, DELPHI, L3, OPAL, SLD Collaborations, the LEP Electroweak Working Group, the Tevatron ElectroweakWorking Group, and the SLD Electroweak and Heavy Flavour Groups. Precision Electroweak Measurements and Constraints on the Standard Model. *CERN PH-EP-2010-095*, 2010.

[13] ALEPH, DELPHI, L3, OPAL Collaborations, and LEPWorking Group for Higgs Boson Searches. Search for the standard model Higgs boson at LEP. *Phys.Lett. B*, 565, 2003.

[14] CDF and D0 Collaborations. Combination of Tevatron Searches for the Standard Model Higgs Boson in the W^+W^- Decay Mode. *Phys. Rev. Lett.*, page 061802, 2010.

[15] CDF Collaboration. Combined search for the standard model Higgs boson decaying to a $b\bar{b}$ pair using the full CDF data set. *Phys. Rev. Lett.*, page 111802, 2012.

[16] CDF and D0 Collaborations. Evidence for a particle produced in association with weak bosons and decaying to a bottom-antibottom quark pair in Higgs boson search at the Tevatron. *Phys. Rev. Lett.*, page 071804, 2012.

[17] D0 Collaboration. Combined search for the standard model Higgs boson decaying to $b\bar{b}$ using the D0 Run II data set. *Phys. Rev. Lett.*, page 121802, 2012.

[18] Lyndon Evans and Philip Bryant. Lhc machine. *JINST*, 3(08):S08001, 2008.

[19] ATLAS Collaboration. Observation of a new particle in the search for the Standard Model Higgs boson with the ATLAS detector at the LHC. *Phys. Lett. B*, 716:1–29, 2012.

[20] CMS Collaboration. Observation of a new boson at a mass of 125 GeV with the CMS experiment at the LHC. *Phys. Lett. B*, 716:30–61, 2012.

[21] https://wikipedia.org/wiki/Standard_Model.

[22] The ATLAS Collaboration. Observation of a new particle in the search for the Standard Model Higgs boson with the ATLAS detector at the LHC. *Phys. Lett.*, B716:1, 2012.

[23] The CMS Collaboration. Observation of a new boson at a mass of 125 GeV with the CMS experiment at the LHC. *Phys. Lett.*, B716:30, 2012.

[24] ATLAS Higgs Physics Results. Summarised at `https://twiki.cern.ch/twiki/bin/view/AtlasPublic/HiggsPublicResults`.

[25] CMS Higgs Physics Results. Summarised at `https://twiki.cern.ch/twiki/bin/view/CMSPublic/PhysicsResultsHIG`.

[26] Super-Kamiokande Collaboration. Evidence for oscillation of atmospheric neutrinos. *Phys.Rev.Lett.*, 81:1562, 1998.

[27] SNO Collaboration. Direct Evidence for Neutrino Flavor Transformation from Neutral-Current Interactions in the Sudbury Neutrino Observatory. *Phys.Rev.Lett.*, 89:011301, 2002.

[28] Luca Rottoli on behalf of the NNPDF collaboration. NNPDF Status and Future Plans. Link to the Talk at `https://indico.cern.ch/event/381832/contributions/1807340`.

[29] Richard D. Ball et al. Parton distributions for the LHC Run II. *JHEP*, 04:040, 2015.

[30] ATLAS and CMS Collaborations. Combined Measurement of the Higgs Boson Mass in pp Collisions at $\sqrt{s} = 7$ and 8 TeV with the ATLAS and CMS Experiments. *Phys. Rev. Lett.*, 114:191803, 2015.

[31] LHC Higgs Cross Section Working Group. Handbook of LHC Higgs Cross Sections: 3. Higgs Properties. *CERN-2013-004*, 2013.

[32] P. Artoisenet, P. de Aquino, F. Demartin, R. Frederix, S. Frixione, et al. A framework for Higgs characterisation. *JHEP*, 1311:043, 2013.

[33] L. D. Landau. On the angular momentum of a two-photon system. *Dokl. Akad. Nauk Ser. Fiz. SSSR*, 60:207–209, 1948.

[34] Chen Ning Yang. Selection Rules for the Dematerialization of a Particle into Two Photons. *Phys. Rev.*, 77:242, 1950.

[35] ATLAS Collaboration. Evidence for the spin-0 nature of the Higgs boson using ATLAS data. *Phys. Lett. B*, 726:120–144, 2013.

[36] LHC Higgs Cross Section Working Group. Handbook of LHC Higgs Cross Sections: 4. Deciphering the Nature of the Higgs Sector. 2016.

[37] G.C. Branco, P.M. Ferreira, L. Lavoura, M.N. Rebelo, Marc Sher, et al. Theory and phenomenology of two-Higgs-doublet models. *Phys. Rept.*, 516:1–102, 2012.

[38] R. Contino K. Agashe and A. Pomarol. The minimal composite Higgs model. *Nucl. Phys. B*, 719:165, 2005.

[39] M. Redi S. De Curtis and A. Tesi. The 4D Composite Higgs. *JHEP*, 04:042, 2012.

[40] M. Serone D. Marzocca and J. Shu. General Composite Higgs Models. *JHEP*, 1208:013, 2012.

[41] G. Panico and A. Wulzer. The Composite Nambu-Goldstone Higgs.

[42] L. Da Rold R. Contino and A. Pomarol. Light custodians in natural composite Higgs models. *Phys. Rev. D*, 75:055014, 2007.

[43] M. S. Carena et al. Electroweak constraints on warped models with custodial symmetry. *Phys. Rev. D*, 76:035006, 2007.

[44] The ATLAS Collaboration. Constraints on new phenomena via Higgs boson couplings and invisible decays with the ATLAS detector. *JHEP*, 206, 2015.

[45] CERN. The CERN accelerator complex. `http://cds.cern.ch/record/2197559`.

[46] O. S. Bruning (Ed.) et al. LHC design report. Vol. I: The LHC main ring. CERN-2004-003-V-1.

[47] ATLAS Collaboration. Performance of pile-up mitigation techniques for jets in pp collisions at $\sqrt{s}$ = 8 TeV Using the ATLAS Detector. *Eur. Phys. J.*, C 76:581, 2016.

[48] Torbjorn Sjöstrand, Stephen Mrenna, and Peter Z. Skands. A Brief Introduction to PYTHIA 8.1. *Comput. Phys. Commun.*, 178:852–867, 2008.

[49] ATLAS Collaboration. Luminosity Public Results. `https://twiki.cern.ch/twiki/bin/view/AtlasPublic/LuminosityPublicResults#Annual_plots`.

[50] ATLAS Collaboration. Luminosity Public Results Run2. `https://twiki.cern.ch/twiki/bin/view/AtlasPublic/LuminosityPublicResultsRun2`.

[51] ATLAS Collaboration. The ATLAS Experiment at the CERN Large Hadron Collider. *JINST*, 3:S08003, 2008.

[52] ATLAS Collaboration. Track Reconstruction Performance of the ATLAS Inner Detector at $\sqrt{s}$=13 TeV. *ATL-PHYS-PUB-2015-018*, 2015. `https://cds.cern.ch/record/2037683`.

[53] ATLAS Collaboration. ATLAS Insertable B-Layer Technical Design Report. *CCERN-LHCC-2010-013, ATLAS-TDR-19*, 2010.

[54] Ruiz-Martinez on behalf of the ATLAS Collaboration. The Run-2 ATLAS Trigger System. Link to the ATLAS Note at `https://cds.cern.ch/record/2133909`.

[55] ATLAS Collaboration. Trigger Menu in 2016. ATL-DAQ-PUB-2017-001, 2017.

[56] ATLAS Collaboration. Improved luminosity determination in pp collisions at $\sqrt{s}$ = 7 TeV using the ATLAS detector at the LHC. *Eur.Phys.J.*, C 73:2518, 2013.

[57] ATLAS Collaboration. Luminosity determination in pp collisions at $\sqrt{s}$ = 8 TeV using the ATLAS detector at the LHC. *Eur.Phys.J.*, C 76:653, 2016.

[58] T. Cornelissen et al. Concepts, Design and Implementation of the ATLAS New Tracking (NEWT). *ATL-SOFT-PUB-2007-007*, 2007. `https://cds.cern.ch/record/1020106`.

[59] ATLAS Collaboration. Muon reconstruction performance of the ATLAS detector in protonproton collision data at $\sqrt{s}$ =13 TeV. *Eur. Phys. J.*, C76(5):292, 2016.

[60] ATLAS Collaboration. Reconstruction of primary vertices at the ATLAS experiment in Run 1 proton-proton collisions at the LHC. *submitted to EPJC*.

[61] ATLAS Collaboration. Electron identification measurements in ATLAS using $\sqrt{s} = 13$ TeV data with 50 ns bunch spacing. ATL-PHYS-PUB-2015-041, 2015.

[62] ATLAS Collaboration. Electron efficiency measurements with the ATLAS detector using the 2015 LHC proton-proton collision data. ATLAS-CONF-2016-024.

[63] ATLAS Collaboration. Topological cell clustering in the ATLAS calorimeters and its performance in LHC Run 1. *Submitted to EPJC*, 2016.

[64] ATLAS Collaboration. Jet Calibration and Systematic Uncertainties for Jets Reconstructed in the ATLAS Detector at $\sqrt{s} = 13$ TeV. ATL-PHYS-PUB-2015-015.

[65] Nazar Bartosik. `http://bartosik.pp.ua/hep_sketches/btagging`.

[66] ATLAS Collaboration. Optimisation of the ATLAS b-tagging performance for the 2016 LHC Run. ATL-PHYS-PUB-2016-012.

[67] Johan Alwall, Michel Herquet, Fabio Maltoni, Olivier Mattelaer, and Tim Stelzer. MadGraph 5 : Going Beyond. *J. High Energy Phys.*, 06:128, 2011.

[68] ATLAS Collaboration. Measurements of Higgs boson production and couplings in the four-lepton channel in pp collisions at center-of-mass energies of 7 and 8 TeV with the ATLAS detector. *Phys. Rev. D*, 91:012006, 2015.

[69] The ATLAS Collaboration. Study of the Higgs boson properties and search for high-mass scalar resonances in the $H \to ZZ^* \to 4\ell$ decay channel at $\sqrt{s}$=13 TeV with the ATLAS detector. *ATLAS-CONF-2016-079*.

[70] https://twiki.cern.ch/twiki/bin/view/AtlasPublic/EventDisplayPublicResults The ATLAS Collaboration.

[71] The ATLAS Collaboration. Search for the Standard Model Higgs boson in the decay channel $H \to ZZ^* \to 4\ell$ with 4.8 fb^{-1}of pp collisions at $\sqrt{s}$=7 TeV.

[72] The ATLAS Collaboration. Measurements of the Higgs boson production cross section at 7, 8 and 13 TeV centre-of-mass energies and search for new physics at 13 TeV in the $H \to ZZ^* \to l^+l^-l'^+l'^-$ final state with the ATLAS detector. *ATLAS-CONF-2015-059*.

[73] Glen Cowan, Kyle Cranmer, Eilam Gross, and Ofer Vitells. Asymptotic formulae for likelihood-based tests of new physics. *Eur.Phys.J.*, C 71:1554, 2011.

[74] Alexander L. Read. Presentation of search results: The CL$_s$ technique. *J. Phys. G*, 28:2693, 2002.

[75] ATLAS Collaboration. Combined search for the Standard Model Higgs boson in pp collisions at $\sqrt{s}$=7 TeV with the ATLAS detector. *Phys. Rev. D*, 86:032003, 2012.

[76] A. Armbruster and J. Qian (dir.). Discovery of a Higgs Boson with the ATLAS Detector. CERN-THESIS-2013-047, `https://cds.cern.ch/record/1553771/`.

[77] Wouter Verkerke and David P. Kirkby. The RooFit toolkit for data modeling. *eConf*, C 0303241:MOLT007, 2003.

[78] Lorenzo Moneta et al. The RooStats Project. *Proc. Sci.*, ACAT2010:057, 2010.

[79] Kyle Cranmer et al. HistFactory: A tool for creating statistical models for use with RooFit and RooStats. *Report No. CERN-OPEN-2012-016*, Jan 2012.

[80] ATLAS Collaboration. Study of the spin and parity of the Higgs boson in diboson decays with the ATLAS detector. *Eur. Phys. J.*, C75(10):476, 2015.

[81] Simone Alioli, Paolo Nason, Carlo Oleari, and Emanuele Re. NLO Higgs boson production via gluon fusion matched with shower in POWHEG. *JHEP*, 0904:002, 2009.

[82] Giuseppe Bozzi, Stefano Catani, Daniel de Florian, and Massimiliano Grazzini. Transverse-momentum resummation and the spectrum of the Higgs boson at the LHC. *Nucl. Phys.*, B 737:73, 2006.

[83] Massimiliano Grazzini and Hayk Sargsyan. Heavy-quark mass effects in Higgs boson production at the LHC. *JHEP*, 1309:129, 2013.

[84] J. Alwall, R. Frederix, S. Frixione, V. Hirschi, F. Maltoni, et al. The automated computation of tree-level and next-to-leading order differential cross sections, and their matching to parton shower simulations. *JHEP*, 1407:079, 2014.

[85] Y. Gao et al. Spin determination of single-produced resonances at hadron colliders. *Phys. Rev. D*, 81:075022, 2010.

[86] S. Bolognesi et al. On the spin and parity of a single-produced resonance at the LHC. *Phys. Rev. D*, 86:095031, 2012.

[87] T. Binoth, N. Kauer and P. Mertsch. Gluon-induced QCD Corrections to $pp \to ZZ \to \ell\bar{\ell}\ell'\bar{\ell}'$. 2008.

[88] LHC Higgs Cross Section Working Group. Handbook of LHC Higgs Cross Sections: 2. Differential Distributions. *CERN-2012-002*, 2012.

[89] T. Gleisberg et al. Event generation with SHERPA 1.1. *J. High Energy Phys.*, 02:007, 2009.

[90] Glen Cowan, Kyle Cranmer, Eilam Gross, and Ofer Vitells. Asymptotic formulae for likelihood-based tests of new physics. *Eur. Phys. J. C*, 71:1554, 2011.

[91] Glen Cowan, Kyle Cranmer, Eilam Gross, and Ofer Vitells. Erratum to: Asymptotic formulae for likelihood-based tests of new physics. *Eur. Phys. J. C*, 73(7), 2013.

[92] P. Speckmayer, A. Hocker, J. Stelzer, and H. Voss. The toolkit for multivariate data analysis, TMVA 4. *J.Phys.Conf.Ser.*, 219:032057, 2010.

[93] Keith Hamilton, Paolo Nason, Emanuele Re, and Giulia Zanderighi. NNLOPS simulation of Higgs boson production. *JHEP*, 10:222, 2013.

[94] Paolo Nason and Carlo Oleari. NLO Higgs boson production via vector-boson fusion matched with shower in POWHEG. *J. High Energy Phys.*, 02:037, 2010.

[95] Gionata Luisoni, Paolo Nason, Carlo Oleari, and Francesco Tramontano. $HW^{\pm}$/HZ + 0 and 1 jet at NLO with the POWHEG BOX interfaced to GoSam and their merging within MiNLO. *JHEP*, 10:083, 2013.

[96] Jon Butterworth et al. PDF4LHC recommendations for LHC Run II. *J. Phys.*, G43:023001, 2016.

[97] Keith Hamilton, Paolo Nason, and Giulia Zanderighi. MINLO: Multi-Scale Improved NLO. *JHEP*, 10:155, 2012.

[98] Stefano Catani and Massimiliano Grazzini. An NNLO subtraction formalism in hadron collisions and its application to Higgs boson production at the LHC. *Phys. Rev. Lett.*, 98:222002, 2007.

[99] Massimiliano Grazzini. NNLO predictions for the Higgs boson signal in the $H \to WW \to \ell\nu\ell\nu$ and $H \to ZZ \to 4\ell$ decay channels. *JHEP*, 02:043, 2008.

[100] Keith Hamilton, Paolo Nason, Carlo Oleari, and Giulia Zanderighi. Merging H/W/Z + 0 and 1 jet at NLO with no merging scale: a path to parton shower + NNLO matching. *JHEP*, 05:082, 2013.

[101] J. Alwall, R. Frederix, S. Frixione, V. Hirschi, F. Maltoni, et al. The automated computation of tree-level and next-to-leading order differential cross sections, and their matching to parton shower simulations. *J. High Energy Phys.*, 07:079, 2014.

[102] Torbjorn Sjöstrand, Stephen Mrenna, and Peter Z. Skands. A Brief Introduction to PYTHIA 8.1. *Comput. Phys. Commun.*, 178:852, 2008.

[103] M. Bahr et al. Herwig++ Physics and Manual. *Eur. Phys. J.*, C58:639–707, 2008.

[104] T. Gleisberg et al. Event generation with sherpa 1.1. *J. High Energy Phys.*, 0902:007, 2009.

[105] Tanju Gleisberg and Stefan Höche. Comix, a new matrix element generator. *JHEP*, 0812:039, 2008.

[106] Fabio Cascioli, Philipp Maierhofer, and Stefano Pozzorini. Scattering Amplitudes with Open Loops. *Phys. Rev. Lett.*, 108:111601, 2012.

[107] B. Biedermann, A. Denner, S. Dittmaier, L. Hofer, and B. Jger. Electroweak corrections to $pp \to \mu^+\mu^- e^+ e^- + X$ at the LHC: a Higgs background study. *Phys. Rev. Lett.*, 116(16):161803, 2016.

[108] Benedikt Biedermann, Ansgar Denner, Stefan Dittmaier, Lars Hofer, and Barbara Jager. Next-to-leading-order electroweak corrections to the production of four charged leptons at the LHC. *JHEP*, 01:033, 2017.

[109] Nikolas Kauer, Claire OBrien, and Eleni Vryonidou. Interference effects for $H \to W\,W \to \ell\nu q\bar{q}'$ and $H \to ZZ \to \ell\bar{\ell}q\bar{q}$ searches in gluon fusion at the LHC. *JHEP*, 10:074, 2015.

[110] Fabrizio Caola, Kirill Melnikov, Raoul Röntsch, and Lorenzo Tancredi. QCD corrections to ZZ production in gluon fusion at the LHC. *Phys. Rev.*, D92:094028, 2015.

[111] John M. Campbell, R. Keith Ellis, Michal Czakon, and Sebastian Kirchner. Two Loop Correction to Interference in $gg \to ZZ$. 2016.

[112] Kirill Melnikov and Matthew Dowling. Production of two Z-bosons in gluon fusion in the heavy top quark approximation. *Phys. Lett.*, B744:43–47, 2015.

[113] Chong Sheng Li, Hai Tao Li, Ding Yu Shao, and Jian Wang. Soft gluon resummation in the signal-background interference process of gg($\to$ h*)$\to$ ZZ. *JHEP*, 08:065, 2015.

[114] The CMS Collaboration. Search for the associated production of a higgs boson with a top quark pair in final states with a τ lepton at $\sqrt{s}$ 13 tev.

[115] The CMS Collaboration. Search for Higgs boson production in association with top quarks in multilepton final states at $\sqrt{s}$ 13 TeV.

[116] The ATLAS Collaboration. Combination of the searches for higgs boson production in association with top quarks in the $H \to \gamma\gamma$, multilepton, and $b\bar{b}$ decay channels at $\sqrt{s} = 13$ tev with the atlas detector.

[117] The ATLAS Collaboration. Study of the Higgs boson properties and search for high-mass scalar resonances in the $H \to ZZ^* \to 4\ell$ decay channel at $\sqrt{s} =$ 13 TeV with the ATLAS detector. *ATLAS-CONF-2016-079*, 2016.

[118] The ATLAS Collaboration. Measurement of fiducial, differential and production cross sections in the $H \to \gamma\gamma$ decay channel with 9.5 fb^{-1} of 13 TeV proton-proton collision data. *ATLAS-CONF-2016-067*, 2016.

[119] A. Hill and J.J. van der Bij. Strongly interacting singlet-doublet Higgs model. *Phys. Rev.*, D 36:3463–3473, 1987.

[120] The ATLAS Collaboration. Search for high-mass resonances decaying into a Z boson pair in the $\ell\ell\nu\nu$ final state in pp collisions at $\sqrt{s}$=13 TeV with the ATLAS detector. *ATLAS-CONF-2016-012*.

[121] The ATLAS Collaboration. Search for diboson resonances in the $\ell\ell qq$ final state in pp collisions at $\sqrt{s} = 13$ TeV with the ATLAS detector. *ATLAS-CONF-2015-071*.

[122] The ATLAS Collaboration. Search for diboson resonances in the $\nu\nu qq$ final state in pp collisions at $\sqrt{s} = 13$ TeV with the ATLAS detector. *ATLAS-CONF-2015-058*.

[123] Simone Alioli, Paolo Nason, Carlo Oleari, and Emanuele Re. NLO Higgs boson production via gluon fusion matched with shower in POWHEG. *J. High Energy Phys.*, 04:002, 2009.

[124] T. Sjöstrand, S. Mrenna, and P. Z. Skands. PYTHIA 6.4 physics and manual. *JHEP*, 0605:026, 2006.

[125] Piotr Golonka and Zbigniew Was. PHOTOS Monte Carlo: a precision tool for QED corrections in Z and W decays. *Eur. Phys. J.*, C 45:97, 2006.

[126] The ATLAS Collaboration. Measurement of the $Z\gamma^*$ boson transverse momentum distribution in pp collisions at $\sqrt{s} = 7$ TeV with the ATLAS detector. *JHEP*, 145, 2014.

[127] Benedikt Biedermann, Ansgar Denner, Stefan Dittmaier, Lars Hofer, and Barbara Jäger. Next-to-leading-order electroweak corrections to $pp \to \mu^+\mu^- e^+ e^-$ at the LHC. to be submitted.

[128] Kyle S. Cranmer. Kernel estimation in high-energy physics. *Comput. Phys. Commun.*, 136:198–207, 2001.